

## SOUND PROPAGATION IN DUCTS WITH SIDE BRANCHES

by W. K. R. LIPPERT

Division of Building Research, Commonwealth Scientific and Industrial Research Organization,  
Melbourne, Australia

### Summary

The propagation of plane waves in a main conducting duct having a closed side branch is represented by formulae and diagrams with the characteristic reflection and transmission factors. The practical limits of this representation are discussed in measured examples. An effective length of the side branch, which differs from the geometrical length, is derived from the measurements, and its usage is shown to extend the range of validity of the formulae and diagrams.

### Sommaire

On exprime par des formules et des diagrammes, renfermant les coefficients de réflexion et de transmission caractéristiques, la propagation d'ondes planes dans un conduit conducteur principal ayant un embranchement latéral fermé. On examine à partir des résultats de mesure les limites pratiques de validité de ce mode d'expression. On déduit de ces résultats une valeur efficace de la longueur de l'embranchement latéral, valeur qui est différente de la longueur géométrique, et on montre comment on peut l'utiliser pour étendre le domaine de validité des formules et diagrammes.

### Zusammenfassung

Es wird die Ausbreitung ebener Wellen in einem Hauptrohr mit abgeschlossenem Seitenrohr in Formeln und Diagrammen mit Hilfe der charakteristischen Reflexions- und Übertragungsfaktoren dargestellt. Die praktischen Grenzen dieser Darstellung werden an Hand von Meßbeispielen diskutiert. Eine wirksame Länge des Seitenrohres, die sich von der geometrischen Länge unterscheidet, wird von den Meßergebnissen hergeleitet, und es wird gezeigt, daß ihre Anwendung den Gültigkeitsbereich der Formeln und Diagramme erweitert.

### 1. Introduction

The basic idea of producing interference between sound waves propagating in acoustical tubes and of suppressing certain frequencies originated with HERSCHEL in 1833 and was first applied by QUINCKE in 1866. Later, when electrical wave filters were developed, STEWART [1], [2], [3], MASON [4], WAETZMANN and NOETHER [5], LINDSAY [6] and others showed that at low frequencies acoustical filters can be devised in analogy to electrical filters. As a result there has been an improvement in the design of mufflers in automobiles, in air conditioning systems and in other practical applications, and textbooks on the theory and practice of acoustical filters are now available [7].

In recent papers on particular problems of plane wave propagation in ducts [8], [9] the present author found that there are cases where it is preferable to represent the frequency characteristics of acoustical filters with specific parameters called

characteristic reflection and transmission factors. It was shown that these parameters are particularly useful in certain periodic structures. Apart from this the characteristic factors are easily and directly measurable, as has been amply demonstrated [10], [11], [12].

The purpose of this paper is to apply the new method to a fundamental acoustical filter consisting of a main conducting tube and a closed side branch. The long-wavelength approximation represented by the characteristic factors yields clear and informative diagrams whose usefulness is illustrated by measured examples. The theoretical and experimental approach discussed below will help to demonstrate the degree of accuracy that can be achieved with this kind of first order approximation. It will follow from the measurements that the effective length of the side branch has to be used in the formulae instead of the geometrical length, and the method of measuring this effective length will be described in detail.



## 2. The characteristic reflection and transmission factors for plane waves in a duct with a closed side branch

Fig. 1 shows a main duct of rectangular cross section and of unspecified length with height  $a$  and width  $b$ , and a rectangular side branch with the cross sectional dimensions  $d$  (depth in direction of the main duct) and  $e$  (width). The geometrical length  $L$  of the side branch is the distance between the opening plane in the main duct wall and the terminating piston at the end of the side branch. All walls of the main duct and of the side branch are supposed to be hard and rigid.

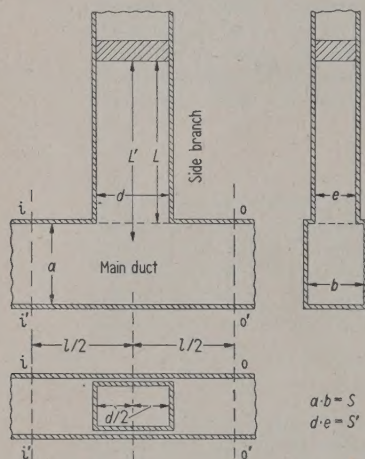


Fig. 1. Main conducting duct with a closed side branch both of rectangular cross-section specifying the various dimensions and the positions of input ( $i, i'$ ) and output ( $o, o'$ ) reference planes.

By restricting the wave propagation to plane waves it is assumed that the wavelength  $\lambda$  is always greater than  $2a$  or  $2b$  or  $2d$  or  $2e$ . The position of the input reference plane in the main conducting duct is specified by  $i, i'$  and that of the output reference plane by  $o, o'$ . Both are perpendicular to the axis of the main duct, at a distance  $l$  from each other and symmetrical with respect to the side branch. The output duct being non-reflecting, plane waves propagating along the main duct result in a standing wave in the input and in a progressive wave in the output.

The symmetrical filter section between the reference planes will be specified by the characteristic factors  $R$  and  $T$  [10]. The characteristic reflection factor  $R = A e^{j\alpha}$  is the complex ratio of the sound pressure of the reflected wave and the incident wave at the input reference plane, and the characteristic transmission factor  $T = B e^{j\beta}$  is the ratio of the sound

pressure of the transmitted wave at the output reference plane and the incident wave at the input plane, if the output duct is non-reflecting.

An easy way of deriving  $R$  and  $T$  is by electrical analogy [13]. Fig. 2a shows an electrical circuit between transmission lines the characteristic impedance of which is  $Z_0$  and the waves propagating along those lines have the wavelength  $\lambda$ . The circuit of Fig. 2a can be made equivalent to the acoustical duct of Fig. 1 if electrical voltages and currents at the various terminals are taken to represent sound pressures and volume velocities (particle velocity  $\times$  area of cross section) at the corresponding reference planes.

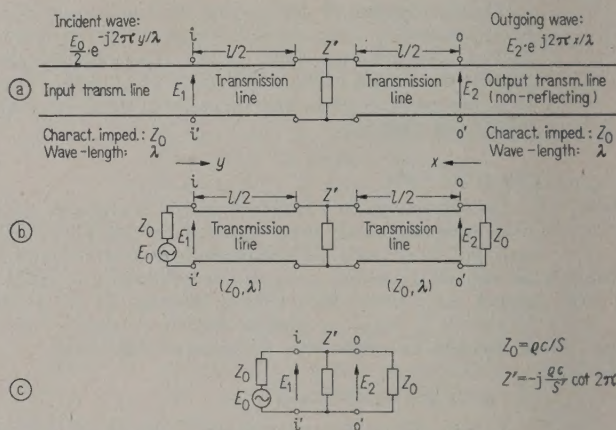


Fig. 2. (a) Electrical analogy to the acoustical duct system of Fig. 1, (b) simplified analogy and (c) the same for the special case  $l=0$ .

The voltages at the input and output terminals are  $E_1$  and  $E_2$  and the incident voltage wave is specified by

$$\frac{E_0}{2} e^{-j2\pi y/\lambda}$$

where  $y$  is the co-ordinate along the input transmission line with  $y=0$  at  $i, i'$ , and the outgoing wave by

$$E_2 e^{j2\pi x/\lambda}$$

where  $x$  is the co-ordinate along the output transmission line with  $x=0$  at  $o, o'$ .

At the input terminal

$$E_1 = \frac{E_0}{2} + E_R$$

where  $E_R$  is the reflected wave. This yields the characteristic factors as specified above

$$R = 2 \frac{E_1}{E_0} - 1, \quad T = 2 \frac{E_2}{E_0}. \quad (1), (2)$$

Applying THEVENIN's theorem to the input transmission line at the terminals  $i, i'$  this line can be re-



presented by a generator with the generator voltage  $E_0$  (voltage at  $i, i'$  if the line is open at the input) and supply resistance  $Z_0$ . The non-reflecting output transmission line is equivalent to a load resistance  $Z_0$  at  $o, o'$ . This representation of the input and output transmission lines by lumped circuit elements in Fig. 2b is convenient for computing  $R$  and  $T$  from eqs. (1) and (2). For actually measuring  $R$  and  $T$ , however, it is suggested that the representation of Fig. 2a and the method described elsewhere [10] be used.

At this stage it is possible to take advantage of a specific feature of the characteristic factors. These factors transform easily for different values of  $l$  or for different positions of the reference planes along the input and output transmission lines, a piece of which ( $l/2$  in length) is circuited in series to the input and output in Fig. 2a and b.

Let the characteristic factors for  $l=0$  be

$$R_0 = A_0 e^{j\alpha_0} \quad \text{and} \quad T_0 = B_0 e^{j\beta_0}$$

then [10]

$$A = A_0, \quad B = B_0 \quad (3)$$

and

$$\alpha = \alpha_0 - 2\pi \frac{l}{\lambda}, \quad \beta = \beta_0 - 2\pi \frac{l}{\lambda}. \quad (4)$$

This means that  $R$  and  $T$  can be easily found from  $R_0$  and  $T_0$  so that it is possible to deal first with the simpler duct system with  $l=0$ , the equivalent circuit of which is given in Fig. 2c. At first sight this may appear to introduce inaccuracies, as when  $l=0$  the wave pattern at the reference planes is greatly disturbed by higher order modes caused by the sudden change in the wall impedance at the side branch. However, in the acoustical case, by definition, the characteristic factors are specified and measured from the standing and progressive waves in the input and output ducts, which are free of disturbances from higher order modes. Therefore, the actual disturbance of the sound field at the reference planes when  $l=0$  is trifling, as long as the position of the reference planes is always transformed (with eqs. (3) and (4)) to parts of the input and output ducts which are free of disturbances, before any connections to other filter systems or sections are considered.

In the electrical circuit of Fig. 2c the impedance  $Z_0$  and the shunt impedance  $Z'$  represent the acoustical characteristic impedance of the main duct and the input impedance of the side-branch duct, which are related:

$$Z_0 = \frac{\rho c}{S} \quad (5)$$

and

$$Z' = -j \frac{\rho c}{S'} \cot 2\pi \frac{L'}{\lambda} \quad (6)$$

where

- $\rho$  density of medium (air),
- $c$  sound velocity,
- $S$  cross section of the main duct,
- $S'$  cross section of the side branch,
- $L'$  effective length of the side branch,
- $\lambda$  wavelength.

In eq. (6) an effective length  $L'$  has been chosen instead of the geometrical length  $L$ . A justification for this and a better specification of  $L'$  will be given in connection with measurements discussed later.

$R_0$  and  $T_0$  can be found from Fig. 2b and with eqs. (1), (2), (5) and (6)

$$R_0 = - \frac{j \frac{1}{2} \frac{S'}{S} \tan 2\pi \frac{L'}{\lambda}}{1 + j \frac{1}{2} \frac{S'}{S} \tan 2\pi \frac{L'}{\lambda}}, \quad (7)$$

$$T_0 = \frac{1}{1 + j \frac{1}{2} \frac{S'}{S} \tan 2\pi \frac{L'}{\lambda}}. \quad (8)$$

Eqs. (7) and (8) are equivalent to

$$A_0 = \frac{\frac{1}{2} \frac{S'}{S} \tan 2\pi \frac{L'}{\lambda}}{\sqrt{1 + \frac{1}{4} \left( \frac{S'}{S} \right)^2 \tan^2 2\pi \frac{L'}{\lambda}}}, \quad (9)$$

$$\alpha_0 = \frac{3}{2} \pi - \arctan \left( \frac{1}{2} \frac{S'}{S} \tan 2\pi \frac{L'}{\lambda} \right) \quad (10)$$

and

$$B_0 = \frac{1}{\sqrt{1 + \frac{1}{4} \left( \frac{S'}{S} \right)^2 \tan^2 2\pi \frac{L'}{\lambda}}}, \quad (11)$$

$$\beta_0 = - \arctan \left( \frac{1}{2} \frac{S'}{S} \tan 2\pi \frac{L'}{\lambda} \right). \quad (12)$$

These formulae have a simple form and are very suitable for experimental checking, as will be shown later.

$R_0$  and  $T_0$  belong to a loss-free filter so that the following conditions are fulfilled [10]

$$A_0^2 + B_0^2 = 1 \quad \text{and} \quad \alpha_0 - \beta_0 = \pm \frac{\pi}{2} \quad (13)$$

which means that eqs. (9), (10) and (11), (12) are interrelated and that it is sufficient to give a diagram for one set of equations only.

In Fig. 3a  $B_0$  and in Fig. 3b  $\beta_0$  has been plotted against  $2L'/\lambda$  for various values of  $S'/S$ . Only one cycle for  $0 \leq 2L'/\lambda \leq 1$  has been drawn as the values of  $B_0$  and of  $\beta_0$  are repeated if  $2L'/\lambda$  is increased by an integer ( $N=0, 1, 2, 3, \dots$ ).

The usefulness of the diagrams of Fig. 3 is best illustrated by examples, and some results of actual measurements are reported below.



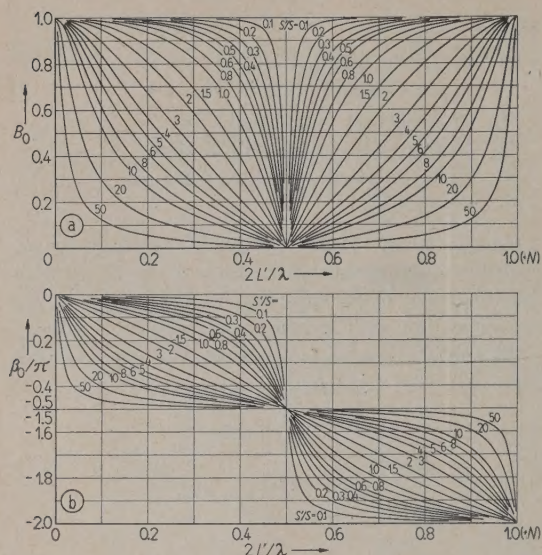


Fig. 3. Magnitudes ( $B_0$ ) and phase values ( $\beta_0$ ) of the characteristic transmission factors of a duct system of Fig. 1 with  $l=0$  plotted against  $2L'/\lambda$  for various ratios  $S'/S$ .

### 3. The measured duct system

The duct system used for the measurements is shown in Fig. 4a. The main conducting duct and the side branch have the same square cross section. From the specification of Fig. 1 this means that  $a=b=d=e$ . Fig. 5 shows a photograph of the duct system.

The main duct is made of brass with a square cross section of 7.6 cm (inside) and wall thickness of 0.95 cm. Other dimensions of the system are shown in Fig. 4. Part of the main duct, 25 cm in length, consists of hardwood having a square opening (7.6 cm  $\times$  7.6 cm) in the top wall.

The side branch is made of brass with the same cross sectional measurements as the main duct and with angle pieces of brass at the ends. The side branch duct is put on top of the main duct so that the square opening and the cross section of the side branch fit accurately. A thin rubber lining (0.02 cm thick) has been applied on the outer top wall of the main duct to ensure a complete seal of the joint with the side branch. Two clamps hold the side branch in position. Within the side branch duct, the walls of which have been carefully machined, a brass piston with a wooden extension can be moved up and down. A good seal was obtained by making the piston sides slightly (0.01 to 0.02 cm) smaller than those of the inner tube walls and by inserting long strips of shim brass of appropriate thickness between the walls and the piston.

The length  $L$  of the side branch can be varied continuously up to  $L=62.7$  cm. (This value of  $L$  is obtained by removing the piston completely and terminating the side branch end with a metal plate.)

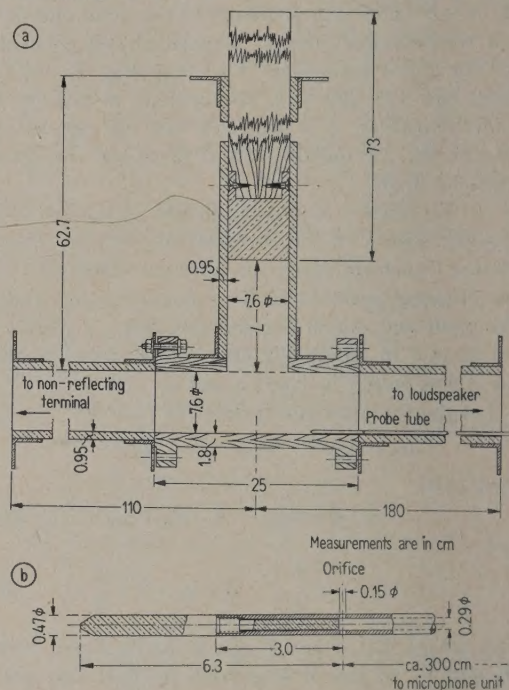


Fig. 4. Diagram showing a cross section (a) of the measured side branch system and (b) of the orifice part of the probe tube.

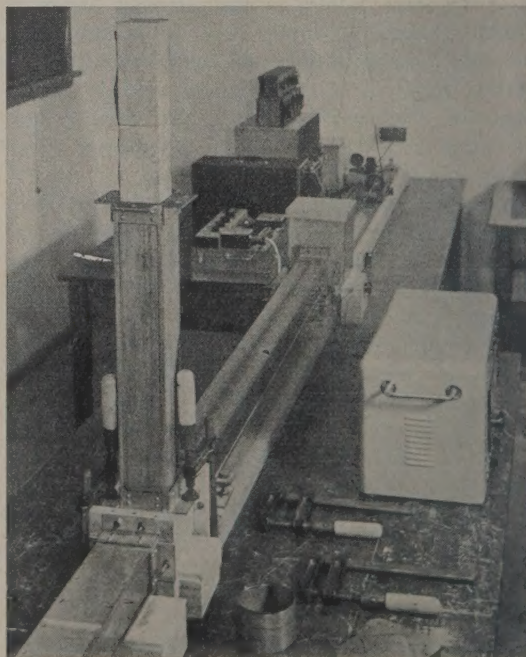


Fig. 5. Photograph of the measured side branch system.



#### 4. Equipment and measuring technique

The equipment for measuring the characteristic factors, including the non-reflecting terminal, microphone unit and other electrical parts, is the same as described in previous papers [8], [12]. By taking advantage of the fact that in the present acoustical filter systems the input and output sound fields can be recorded continuously and in one probing run, the probe tube of the microphone unit has been extended to about 300 cm. The dimensions of the steel probe tube are shown in Fig. 4 b. The microphone unit is mounted on a trolley which can be moved by a motor and pulley system at constant speed along a steel ruler. The probe tube which is attached to the microphone may thus be moved slowly along the bottom of the main duct with the position of the orifice varying continuously between distances of about 70 cm in the output side (negative  $x$  co-ordinates) to about 100 cm in the input side (negative  $y$  co-ordinates). During each run the frequency was kept constant and the sound pressure recorded with a high-speed level recorder. The probing procedure can also be done by hand for accurately measuring the minima positions and the position of equal phase in the standing and progressive waves.

Fig. 6 shows some records at various frequencies with a recording time of about 100 s for each record. In Figs. 6 a to d the length of the side branch is  $L=62.7$  cm and the frequencies are 400, 700, 1200 and 1600 c/s respectively. In Fig. 6 e  $L=17$  cm and the frequency is 2200 c/s. These records were all taken with a 50 dB potentiometer of the level recorder. The position in the main duct is specified by a few distance marks at the top of each record, corresponding to  $x = -50$  cm and  $x = 0$  cm in the output duct and to  $y = 0$  cm,  $y = -50$  cm and  $y = -100$  cm in the input duct. The positions  $x=0$  and  $y=0$  in the output and input reference planes coincide in these cases, as  $l=0$ .

These examples show that, in general, there is a standing wave in the input duct and a progressive wave in the output duct, with a disturbance caused by higher order modes in that part of the main duct where the side duct branches off. This disturbance is restricted, however, to a short distance in the input and output ducts and the characteristic transmission and reflection factors can be easily determined from the undisturbed wave patterns as has been described in earlier papers [8], [10], [11]. The records (c) to (e) of Fig. 6 are typical examples to demonstrate how greatly the wave pattern in the duct systems measured can vary. In record (c) the ratio of minimum to maximum sound pressure in the input ( $P_{\min}/P_{\max}$ ) is about -28 dB or 0.04, and the ratio of transmitted sound pressure in the

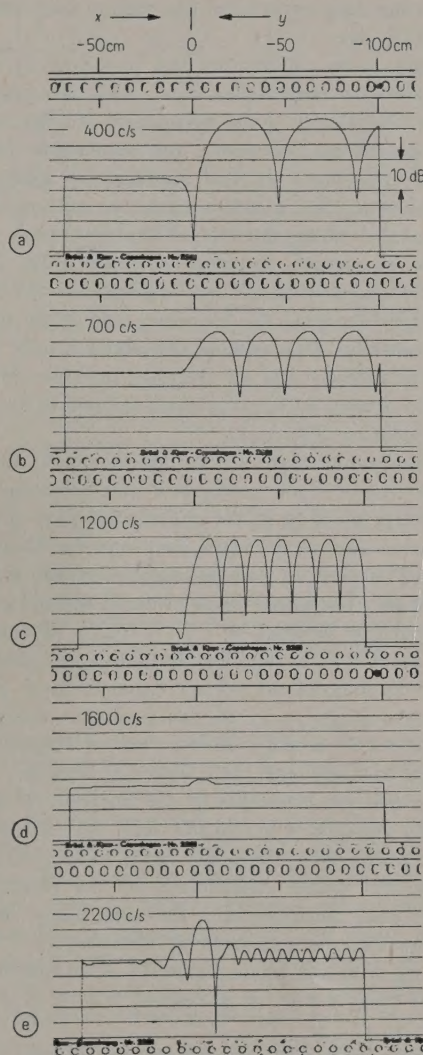


Fig. 6. Examples of records (with a 50 dB potentiometer) showing the sound pressure distribution in the main duct at various frequencies (a) 400, (b) 700, (c) 1200, (d) 1600 and (e) 2200 c/s;  $L=62.7$  cm in (a) to (d) and  $L=17$  cm in (e).

output and maximum sound pressure in the input ( $P_{tr}/P_{\max}$ ) is about -29 dB or 0.035, which yields the values  $B_0=0.07$  and  $A_0=0.92$  [10]. This means that at this particular frequency (1200 c/s) the single side branch has an attenuating effect on the sound propagation comparable with the transmission loss of a light wall.

The opposite can be seen with the record of Fig. 6 d, which was measured at 1600 c/s and where the attenuating effect of the side branch is negligible. In this case the reflection factor  $A_0$  is practically zero which can be seen from the fact



that the standing input wave has degenerated into a progressive one.

In cases with no minima the recording of the sound pressure magnitudes alone does not permit direct measurement of the wavelength. In the technique applied here, however, the wavelength (and not the frequency) is the fundamental quantity which must be determined accurately, and actually in such cases where there is no standing wave not only the wavelength, but also the phase value ( $\beta$ ) of the transmission factor can be measured directly, i. e. without knowing the frequency and phase velocity accurately. This will be explained briefly for symmetrical filters and an arbitrary position of the reference planes, as it is of general interest in acoustical measuring technique.

In cases where there are no minima in the input duct the orifice of the probe tube can be placed at an arbitrary position in the undisturbed part of the progressive wave of the input duct, and the distance between this position and the input reference plane is called  $\Delta z$ . The phase value of the sound pressure at this position denoted by a (+) sign is measured in the usual way by making the phase and magnitude of the microphone voltage equal to those of a reference voltage (e. g. of the oscillator voltage) with the aid of a phase shifter and an attenuator. This can be done with high degree of accuracy by checking that the difference of the microphone and reference voltages is practically zero [8]. By moving the probe tube along the input duct (without changing the phase adjustments of the reference voltage) other positions with the same phase value (+) can then be measured at distances  $\Delta z + N\lambda$  and those with the phase value (-) (which is  $\pi$  different from (+)) at distances  $\Delta z + (N + \frac{1}{2})\lambda$ , with  $N = 0, 1, 2, 3, \dots$

By measuring various distances which belong to different (+) or (-) phase values and numbers  $N$ , the wavelength  $\lambda$  can be computed from the corresponding differences, which are always a multiple of half a wavelength.

The first position in the output duct which has the phase value (-) is then measured in the same way and its distance from the output reference plane is called  $\Delta x$ . By keeping in mind that the distance  $\Delta z$  specified above for  $A = 0$  and the usual distance  $\Delta y$  between the input reference plane and the first pressure minimum of the standing wave in the input duct for  $A \neq 0$  are simply related by

$$\Delta z = \Delta y + \frac{\lambda}{4}; \quad (14)$$

the phase value  $\beta$  of the characteristic transmission factor can then be computed with the earlier formula for general symmetrical filters [10]:

$$\beta = 2\pi \frac{\Delta y + \Delta x}{\lambda} - \frac{\pi}{2}. \quad (15)$$

That this formula is correct in the present case for  $A = 0$  follows from the fact that, although  $\Delta z$  has been chosen arbitrarily in the experimental procedure above, all positions of equal (+) or (-) phase in the progressive input and output waves shift with changing  $\Delta z$  in such a way that the sum  $\Delta y + \Delta x$  does not change. Thus, from eq. (15) the value of  $\beta$  is not changed.

On the other side, the phase value  $\alpha$  of the characteristic reflection factor, which, after [10], depends essentially on  $\Delta y$ , is not measurable in cases where  $A = 0$ ; it is arbitrary because of  $R = Ae^{j\alpha} = 0$ .

As demonstrated above  $\lambda$  and  $\beta$  are still directly and accurately measurable when  $A = 0$ . This rule applies, to some extent to cases where  $A \approx 0$  which in loss-free cases can be very helpful for determining  $\alpha$  by measuring  $\beta$  first and computing  $\alpha$  from the general phase relation for loss-free symmetrical filters (eq. (13)).

Another typical record is shown in Fig. 6 e. It can be seen from this that the disturbance of the wave pattern from higher order modes is greater and extends to longer distances in the input and output parts of the main duct compared with examples at lower frequencies. The frequency in this case was 2200 c/s or the corresponding value of the dimensionless quantity  $\Theta/\pi = 2a/\lambda$  was  $\Theta/\pi = 0.95$  which is rather close to the cut-off frequency (with the value  $\Theta/\pi = 1$ ) below which only plane waves and no higher order modes can be propagated. This indicates that in a frequency range just below the cut-off frequency the simple long-wavelength theory of eqs. (9) to (12) has to be used cautiously and is likely to fail. It is, therefore, of practical importance to determine the limits of applicability of these formulae and of the corresponding diagrams of Fig. 3. This will be done by discussing some measured examples.

## 5. Results of measurements

The characteristic reflection and transmission factors of plane waves travelling along the main duct (illustrated in Fig. 4 a and 5) have been measured at various frequencies and for different lengths  $L$  of the side branch. In these measurements the method of the non-reflecting terminal described above and elsewhere [8], [10] has been applied. In Fig. 7, 8 and 9 the measured values of  $A_0$ ,  $B_0$  and of  $\alpha_0$ ,  $\beta_0$  have been plotted against  $\Theta/\pi$  ( $= 2a/\lambda$ ) for three examples with  $L = 9.4$  cm,  $L = 17$  cm and  $L = 32.2$  cm. (The subscript zero in the measured characteristic factors refers to the position of the reference planes specified by  $l = 0$  as described above.)



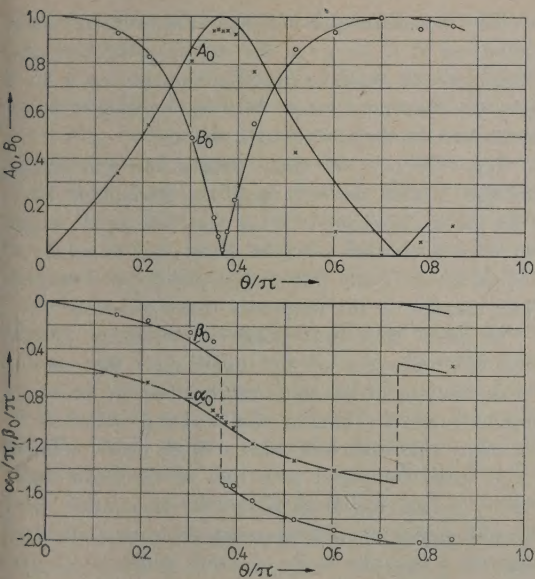


Fig. 7. The measured magnitude ( $A_0$  and  $B_0$ ) and phase values ( $\alpha_0$  and  $\beta_0$ ) of the characteristic reflection and transmission factors plotted against  $\Theta/\pi = 2a/\lambda$  for  $L = 9.4$  cm and the corresponding computed curves for  $L' = 10.37$  cm.

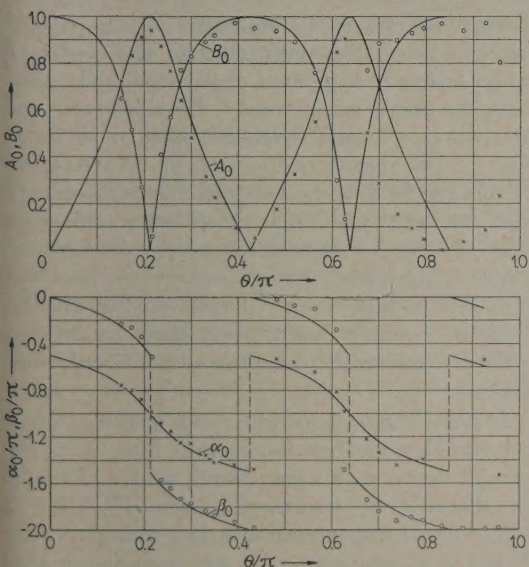


Fig. 8. The measured magnitude ( $A_0$  and  $B_0$ ) and phase values ( $\alpha_0$  and  $\beta_0$ ) of the characteristic reflection and transmission factors plotted against  $\Theta/\pi$  for  $L = 17$  cm, and the corresponding computed curves for  $L' = 17.91$  cm.

The measured quantities can be computed also by using eqs. (9) to (12) or represented by the diagrams of Fig. 3. The parameter is  $S'/S = 1$ . By making  $L' = L$  it was found at first that the com-

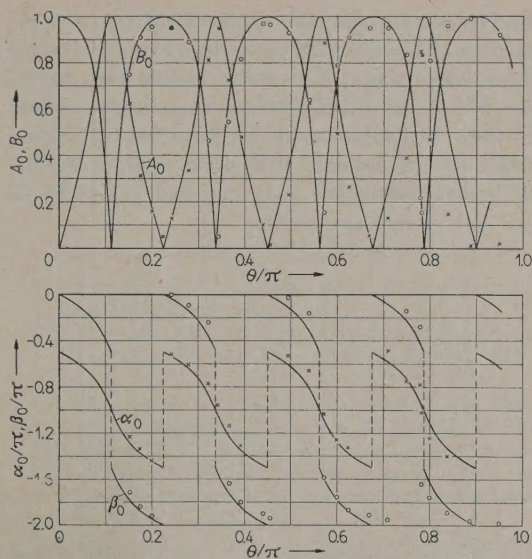


Fig. 9. The measured magnitude ( $A_0$  and  $B_0$ ) and phase values ( $\alpha_0$  and  $\beta_0$ ) of the characteristic reflection and transmission factors plotted against  $\Theta/\pi$  for  $L = 32.2$  cm, and the corresponding computed curves for  $L' = 33.62$  cm.

puted curves did not agree with the measured ones, especially at the minima of  $B_0$  (and  $A_0$ ). Values of  $L'$  were then chosen so that there was good agreement between measured and computed curves at the minima and in the lower and medium frequency range. This could be achieved when  $L'$  was slightly greater than  $L$ . In the examples quoted above the values for  $L'$  providing best agreement between measured and computed curves were: in Fig. 7  $L' = 10.37$  cm, in Fig. 8  $L' = 17.91$  cm and in Fig. 9  $L' = 33.62$  cm. With these values of  $L'$  the theoretical curves of  $B_0$  and  $\beta_0$  have been plotted in Figs. 7 to 9 with the diagrams of Fig. 3 and also those curves of  $A_0$  and  $\alpha_0$  with eq. (13) or eqs. (9) and (10).

There is good agreement between measurements and theory in a wide frequency range between at least  $0 < \Theta/\pi \leq 0.5$ . In Fig. 9 even several cycles (with  $N = 0, 1$  and  $2$  of Fig. 3) of the magnitude and phase curves are repeated very well. In the range where  $0.5 < \Theta/\pi < 1$  the difference between the measured and computed curves becomes greater with increasing frequency, as can be seen from the measured examples, and the approximating eqs. (9) to (12) become less accurate the closer  $\Theta/\pi$  approaches the value unity, which is not surprising (cf. Fig. 6e).

In the frequency range, where the approximating theory is valid, the accuracy of the computed values depends very much on the knowledge of the effec-



tive length  $L'$  especially at the frequencies where minima of  $B_0$  occur. To get a clearer picture of how  $L'$  depends upon  $L$ , more measurements were carried out with different length  $L$  and the effective lengths  $L'$  were determined as above, from the  $\Theta/\pi$  values where the first minima of  $B_0$  occur or from the best fit between measured and computed curves of  $B_0$  (or  $A_0$ ) plotted against  $\Theta/\pi$ .

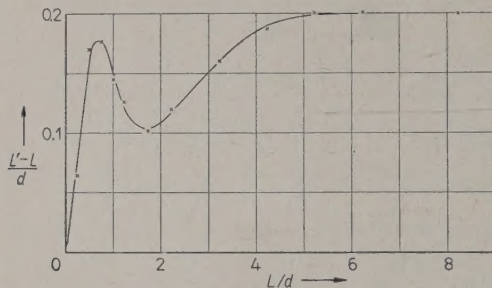


Fig. 10. The measured ratios  $(L' - L)/d$  plotted against  $L/d$  for a side branch system with the same square cross section of both main and side branch duct.

In Fig. 10 the measured ratio  $(L' - L)/d$  has been plotted against the ratio  $L/d$  where  $d = 7.6$  cm (3 in) is the width of the square side branch, which in this particular case is equal to that of the main duct (Fig. 4a). With increasing  $L/d$  the curve of the measured values in Fig. 10 at first shows a maximum and a minimum and finally reaches a constant value of  $(L' - L)/d \approx 0.2$  when  $L/d > 4$ . This curve provides a quick means of finding  $L'$  if  $L$  and  $d$  are given. Fig. 10 refers to the special case where  $d = a$  and  $b = e = a$ . However, similar curves for finding  $L'$  can be measured when  $d \neq a$  and  $b \neq e$  (Fig. 1) or when the cross section of the side branch is other than rectangular, e. g. is circular. This method of determining  $L'$  is obviously superior to the rough guess of the effective length, e. g.  $L' = L + (a/2)$ , which has been recommended [7].

## 6. Discussion

The results of the measurements discussed above constitute an experimental study which demonstrates the validity of the approximating equations (9) to (12) and of the diagrams of Fig. 3. The results obtained will vary with different shapes and dimensions of the cross section of the main duct and of side branches. However, even in cases of varied experimental conditions the particular examples of the present study are informative by showing what sort of agreement can be expected between theory and practice, and the experimental procedure applicable.

The measurements indicate that accurate determination of  $L'$  (e. g. in the experimental way discussed above) leads to closer agreement over a much greater frequency range between experimental results and the long-wavelength theory.

Eqs. (9) to (12) show clearly how the characteristic factors depend upon the parameter  $S'/S$ . The particular shape of  $S'$  or  $S$  as well as the length of the side branch have an effect on the values of  $L' - L$  or of  $L'$  and thus on the positions of minima and maxima in the frequency characteristics.

In cases of several equal side branches around the circumference of the main duct the various cross sections of the side branches have to be added up to form  $S'$ . That a summarizing effect of  $S'$  of many side branches (with a single cross sectional area small compared with that of the main duct) really occurs has been shown by the author in a former paper on measurements of sound attenuation in a duct the walls of which consisted of perforated bricks covered by plywood at the outside [14].

When a side branch system of Fig. 1 is used as an element of an acoustical filter, e. g. by connecting the output to another discontinuity or by repeating the same side branch at equal distances along the main duct, the values of  $A_0$ ,  $B_0$  and  $\alpha_0$ ,  $\beta_0$  have to be transformed to  $A$ ,  $B$  and  $\alpha$ ,  $\beta$  which belong to a position of the input and output reference planes symmetrical to the side branch and at a distance  $l$  apart from each other as shown in Fig. 1. This transformation of the characteristic factors can be done most conveniently with eqs. (3) and (4). The value  $l$  has to be made sufficiently large, so that the sound fields at the input and output reference planes are reasonably free from disturbances of higher order modes (cf. Fig. 6). The value of  $l$  usually has a great effect on the frequency characteristics of multi-sectional acoustical filters.

In cases of  $n$ -sectional filters each section of which consists of a loss-free symmetrical filter as in the present case e. g. of a side branch section of Fig. 1, the characteristic transmission factor  $T_n = B_n e^{j\beta_n}$  can be found with general diagrams from the values  $B$  and  $\beta$  of one section, as has been shown elsewhere [9]. There is a practical advantage in the use of such diagrams. From eqs. (3) and (4) it follows that  $\beta$  alone depends upon  $l$  but  $B$  does not. Thus the effect of the various parameters  $S'/S$ ,  $L'$ ,  $l$  and  $n$  on the form and positions of maxima and minima (or of pass- and stop-bands) of the final frequency characteristics can be separated and considered step by step. The frequency characteristics can be described completely, and specific values of various parameters may be selected to meet practical



design requirements. This is illustrated in the following example.

A practical problem is to design an  $n$ -sectional acoustical side branch filter (with a practically non-reflecting termination of the main duct) so that an attenuation as large as possible is obtained in a frequency range with a given middle frequency  $f_{st} = c/\lambda_{st}$  (where  $\lambda_{st}$  is the wavelength in the duct at  $f_{st}$ ). At first, it is obvious that the number of sections  $n$  and the parameter  $S'/S$  (cf. Fig. 3a) should be chosen as large as practically possible. From the general diagrams of  $n$ -sectional filters (Fig. 3 to 5 in [9]) (where  $B_n$  is represented by  $B$  and  $\beta$ ) it follows that  $B$  must have a small value and  $\beta$  should equal  $\pm N\pi$  at  $f_{st}$  to make the value of  $B_n$  small at the particular frequency and in the neighbouring frequency range. From Fig. 3a  $B_0 = B = 0$  is obtained when  $2L'/\lambda_{st} = \frac{1}{2}$  or when  $L' = \lambda_{st}/4$  in which case also it follows from Fig. 3b that  $\beta_0 = \pm \pi/2$ . The required value of  $l$  can now be determined with eq. (4) by taking e.g.  $\beta = -\pi$ ,  $\beta_0 = -\pi/2$  and  $\lambda = \lambda_{st} = 4L'$ . This yields  $l = L' = \lambda_{st}/4$  which is the well known condition for large attenuation of a side branch filter at a particular frequency and in the neighbouring frequency range [7]. The values of  $n$  and  $S'/S$  being specified the frequency characteristics of  $B_n$  (and  $\beta_n$ ) can then be determined completely with diagrams in the way discussed above.

## 7. Conclusions

Formulae and diagrams for representing the characteristic reflection and transmission factors of plane sound waves propagating along a main conducting duct with a closed side branch have been derived. The practical limits of the long-wavelength approximation are discussed experimentally for a particular side branch system having the same cross-section area as the main duct. The use of an accurate value

for the effective length of the side branch is shown to be important and a practical method of measuring this length is demonstrated. The technique adopted in this paper is considered to be practicable and useful in the design of acoustical filters with side branch systems, e.g. of  $n$ -sectional periodic structures.

(Received 15th January, 1956.)

## References

- [1] STEWART, G. W., Acoustic wave filters. *Phys. Rev.* **20** [1922], 528–551.
- [2] STEWART, G. W., Acoustic wave filters: Attenuation and phase factors. *Phys. Rev.* **23** [1924], 520–524.
- [3] STEWART, G. W., Acoustic wave filters: An extension of the theory. *Phys. Rev.* **25** [1925], 90–98.
- [4] MASON, W. P., A study of the regular combination of acoustic elements, with application to recurrent acoustic filters, tapered acoustic filters, and horns. *Bell Syst. tech. J.* **7** [1927], 258–294.
- [5] WAETZMANN, E. und NOETHER, F., Über akustische Filter. *Ann. Phys., Lpz.* (5) **13** [1932], 212–228.
- [6] LINDSAY, R. B., The filtration of sound I and II. *J. appl. Phys.* **9** [1938], 612–622; **10** [1939], 680–687.
- [7] MASON, W. P., Electromechanical transducers and wave filters. D. van Nostrand Comp. Inc., New York 1946.
- [8] LIPPERT, W., The measurement of sound reflection and transmission at right-angled bends in rectangular tubes. *Acustica* **4** [1954], 313–319.
- [9] LIPPERT, W., A new method of computing acoustical filters. *Acustica* **4** [1954], 479–488.
- [10] LIPPERT, W., A method of measuring discontinuity effects in ducts. *Acustica* **4** [1954], 307–312.
- [11] LIPPERT, W., An extended method of measuring acoustical filters. *Acustica* **5** [1955], 269–273.
- [12] LIPPERT, W., Wave transmission around bends of different angles in rectangular ducts. *Acustica* **5** [1955], 274–278.
- [13] LIPPERT, W., New filter theory of periodic structures. *Wirel. Engr.* **32** [1955], 260–266 and 305–310.
- [14] LIPPERT, W., Experimentelle Untersuchungen zur Theorie der Schallausbreitung in schalldämpfenden Röhren. *Akust. Z.* **6** [1941], 46–64.



# SCHWINGUNGSUNTERSUCHUNGEN AN EISENBAHNSCHIENEN IM ULTRASCHALL-BEREICH

von H. HAESKE

III. Physikalisches Institut der Universität Göttingen

## Zusammenfassung

1. Es wurden die Beschleunigungen ermittelt, die durch die Überfahrt eines Zuges im Schienenkopf erzeugt werden. Im untersuchten Frequenzbereich von 10 bis 100 kHz liegen diese in der Größenordnung von  $10 \text{ m/s}^2$  je kHz Bandbreite. Die Spektren fallen mit wachsender Frequenz nur allmählich ab; bei der waagerechten Komponente ist diesem Abfall eine Überhöhung von 8 dB im Bereich von 35 bis etwa 60 kHz überlagert.

Zur Schwingungsanregung der Schiene wurden zwei Modellversuche durchgeführt; aus ihnen geht hervor, daß der Verlauf des Beschleunigungsspektrums nur bedingt von der Art der Anregung abhängt.

2. Es wurden die Schwingungseigenschaften der Schiene untersucht. Bei der Messung der Wellenlängen zeigte sich — in Übereinstimmung mit früheren Untersuchungen von NAAKE — das Auftreten neuer Dispersionsäste bei etwa 35 und 60 kHz. Ferner wurde bei sinusförmiger Schwingungsanregung die resultierende Amplitudenverteilung längs der Schiene aufgenommen. Die erhaltenen Diagramme zeigen je nach Frequenz sehr verschiedene Gestalt; es treten große Welligkeiten auf, die durch stehende Wellen wie auch durch Superposition mehrerer Wellentypen verursacht werden. Die resultierende Amplitudenverteilung hängt stark vom Ort der Anregung ab.

Die Dämpfung der Wellenausbreitung im Schienenkopf beträgt im untersuchten Frequenzbereich meist weniger als 0,3 dB/m. Die Untersuchung von Schweißstellen ergab für Abbreinstumpfschweißungen kaum eine Dämpfung ( $< 1 \text{ dB}$ ), Thermit-Schweißstellen hingegen dämpfen die durchlaufende Welle bis zu 6 dB.

## Summary

1. The accelerations in the frequency range 10 to 100 kc/s experienced by the rail during the passage of a train are measured. The spectrum falls off slowly with rising frequency; this depends only on the type of excitation (as shown by model research).

2. The mode of vibration of the rail is investigated. Dispersion regions appear between 35 and 60 kc/s. A large waviness appears along the rail, ascribed to the superposition of standing waves of many types, and a function of the place of excitation. The attenuation in this frequency range is less than 0.3 dB/m. Electric welds produced an attenuation  $< 1 \text{ dB}$ , but thermite welds up to 6 dB, for the progressive waves.

## Sommaire

1. On a déterminé les accélérations qui sont produites dans le champignon d'un rail par le passage d'un train. Dans la gamme des fréquences étudiée, soit 10 à 100 kHz, ces accélérations sont d'un ordre de grandeur de  $10 \text{ m/s}^2$  par kHz de largeur de bande. Les spectres ne s'affaiblissent que progressivement quand la fréquence augmente; dans le cas des composantes horizontales, il se superpose à cette décroissance une pointe de 8 dB dans la gamme allant de 35 à environ 60 kHz.

Pour exciter la vibration des rails, on a procédé à deux essais sur maquette; les résultats montrent que l'allure du spectre d'accélération n'est déterminée que par le mode d'excitation.

2. On a étudié les caractéristiques vibratoires des rails. La mesure des longueurs d'onde a mis en évidence — en bon accord avec les résultats des études antérieures de NAAKE — de nouvelles branches de dispersion à environ 35 et 60 kHz. On a relevé en outre, dans le cas d'une excitation de forme sinusoïdale, la distribution des amplitudes résultantes le long du rail. Le diagramme obtenu a une forme qui diffère beaucoup suivant la fréquence; il se produit des ondulations importantes qui sont dues à des ondes stationnaires ainsi qu'à la superposition de plusieurs types d'ondes. La distribution résultante de l'amplitude dépend fortement du point où se fait l'excitation.

L'amortissement des ondes dans le champignon du rail est le plus généralement inférieur à 0,3 dB/m dans la gamme des fréquences étudiées. Les régions de soudure ne produisent qu'un amortissement insignifiant dans le cas de joints soudés électriquement ( $< 1 \text{ dB}$ ). Les soudures thermiques amortissent par contre l'onde jusqu'à 6 dB.



## Einleitung

Die seinerzeit von NAAKE [1] durchgeführten Schwingungsuntersuchungen ergaben unter anderem den überraschenden Sachverhalt, daß im Tonfrequenzbereich die Dämpfung einer in der Schiene entlanglaufenden Welle mit wachsender Frequenz abnimmt. Es war daher von Interesse, das Verhalten der Schiene im Ultraschallbereich kennen zu lernen. In neuen Untersuchungen wurden deshalb die Schwingungseigenschaften der Schiene im Frequenzbereich von 10 bis 100 kHz ermittelt und die Beschleunigungen gemessen, die durch die Überfahrt eines Zuges in der Schiene erzeugt werden.

## 1. Aufnahme und Spektralanalyse des Überfahrtgeräusches

### 1.1. Die Meßmethode

Es wurden die senkrechten und die waagerechten Transversalbeschleunigungen ermittelt. Zu diesem Zweck wurde am Kopf der Schiene ein magnetischer Körperschall-Empfänger befestigt, dessen abgegebene Spannung nach FOURIER analysiert wurde, um die Beschleunigung als Funktion der Frequenz zu erhalten. Zur Analyse diente ein Überlagerungsempfänger mit einer Bandbreite von 80 Hz; die Umwandlung der der Schnelle proportionalen Mikrophonspannung in eine der Beschleunigung proportionale Eingangsspannung für den Analysator wurde durch einen entsprechenden Frequenzgang des Vorverstärkers erzielt.

Die zur Analyse des gesamten Bereiches von 10 bis 100 kHz erforderliche Zeit betrug etwa 2,5 Minuten. Da eine Speicherung des Geräusches wegen der hohen Frequenzen nicht möglich war, mußten die an mehreren Zügen gewonnenen Meßergebnisse zusammengesetzt werden, um den ganzen Frequenzbereich zu überdecken. Es wurde dazu in Vorversuchen sichergestellt, daß während der Überfahrt eines Zuges eine beliebige Frequenz zu jeder Zeit mit etwa gleicher Amplitude angeregt wird und daß gleichartige Züge mit gleicher Fahrgeschwindigkeit im Mittel dieselben Beschleunigungen hervorrufen. Die gefundenen Schwankungen betragen 2 bis 5 dB und liegen damit im Bereich der bei derartigen Messungen zu erwartenden Ungenauigkeiten.

### 1.2. Die Meßergebnisse

Die Analyse wurde für Güterzüge und für Schnellzüge durchgeführt. In Abb. 1 sind zwei Beispiele für die erhaltenen Spektren wiedergegeben. Um den Einfluß von Zufälligkeiten oder verschiedener Wagentypen zu eliminieren, wurde über mehrere derartige Spektrogramme gemittelt. Daraus ergaben sich die in Abb. 2 gezeigten Diagramme. Es treten demnach im Ultraschallbereich noch beträchtliche

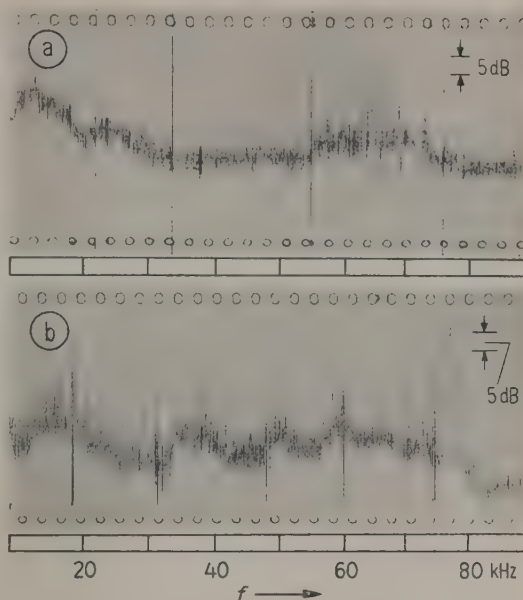


Abb. 1. Beispiele für die bei der Analyse erhaltenen Pegelschreiberstreifen; (a) senkrechte, (b) waagerechte Beschleunigungen des Schienenkopfes.

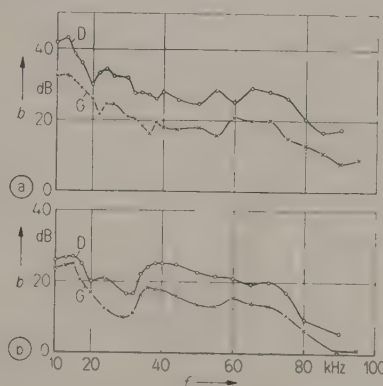


Abb. 2. Die durch die Überfahrt eines Zuges im Schienenkopf hervorgerufenen Beschleunigungen als Funktion der Frequenz; (a) senkrechte, (b) waagerechte Beschleunigungen. Die mit „D“ gekennzeichneten Kurven wurden bei Schnellzügen, die mit „G“ bezeichneten bei Güterzügen gemessen. Der Bezugspegel 0 dB entspricht einer Beschleunigung von  $0,1 \text{ m/s}^2$  je 80 Hz Bandbreite.

Beschleunigungen auf, die in der Größenordnung von  $10 \text{ m/s}^2$  je kHz Bandbreite liegen. Alle vier Diagramme zeigen im Prinzip einen ähnlichen, mit zunehmender Frequenz leicht abfallenden Verlauf, nur liegen die Pegel bei den D-Zügen infolge größerer Fahrgeschwindigkeit höher als bei den Güterzügen (95 bzw. 55 km/h). Ein Vergleich der senkrechten mit den waagerechten Beschleunigungen zeigt jedoch



bei letzteren außer einem — leicht verständlichen — geringeren Gesamtpegel eine auffällige Überhöhung von 8 bis 9 dB, die bei etwa 35 kHz beginnt und sich bis 60 kHz hinzieht.

### 1.3. Modellversuche

Die auf vorstehend beschriebene Weise erhaltenen Spektren unterscheiden sich bei Zügen mit verschiedenen Wagentypen nur geringfügig. Und da selbst die Diagramme von Güterzügen und von Schnellzügen (mit ihrer etwa doppelten Fahrgeschwindigkeit!) einen sehr ähnlichen Verlauf zeigen, erhebt sich die Frage, inwieweit das erhaltene Spektrum überhaupt ein Charakteristikum für den betreffenden Zug darstellt und wie stark es durch die Schwingungseigenschaften der Schiene selbst bedingt wird. Als Beitrag zu dieser Überlegung wurden zwei Modellversuche durchgeführt:

Die Schwingungsanregung der Schiene während der Überfahrt eines Zuges erfolgt durch die nur sehr geringe Relativbewegung zwischen Rad und Schiene, aber die dabei auftretenden Kräfte sind sehr groß (Achslast bis 20 t!). Im Versuch wurde nun das rollende Rad durch eine kleine rotierende Eisenscheibe von 8 cm Durchmesser und 2 cm Dicke ersetzt, die an einem festen Ort gegen die Schiene gedrückt wurde. Die Relativgeschwindigkeit dieser schleifenden Scheibe gegen die Schiene betrug etwa 2 m/s, die andrückende Kraft etwa 50 kg. Obwohl die Anregungsbedingungen bei diesem Modellversuch äußerst verschieden waren von den Verhältnissen bei der Überfahrt eines Zuges, zeigen die erhaltenen Beschleunigungsspektren wieder die gleichen Merkmale.

In einem zweiten Modellversuch wurde die Anregung der Schiene noch stärker idealisiert, indem auf eine Relativbewegung zwischen anregendem System und Schiene ganz verzichtet wurde. Die Schiene wurde durch einen mit einer Rauschspannung gespeisten Körperschall-Sender angeregt, der an verschiedenen Stellen der Schiene befestigt wurde. Die auf diese Art erhaltenen Spektren zeigen zwar große Abweichungen voneinander und hängen in ihrem Verlauf stark vom Anregungsort ab, allen gemeinsam ist jedoch wieder die Überhöhung des Pegels im Frequenzbereich von 35 bis etwa 60 kHz, ähnlich wie im ersten Modellversuch oder wie in praxi beim Überfahrtgeräusch der Züge. Das erhaltene Beschleunigungsspektrum hängt demnach nur bedingt von der Art der Anregung ab.

## 2. Untersuchung der Schwingungseigenschaften der Schiene

Die weiteren Untersuchungen hatten zum Ziel, die Schwingungseigenschaften der Schiene selbst zu

ermitteln. Die Messungen erfolgten an geschweißten Langschienen. Die Schwingungen wurden durch einen piezoelektrischen Körperschall-Sender erzeugt, als Mikrophon diente ein magnetischer Körperschall-Empfänger, der sich in einem kleinen Wagen befand und in konstantem Abstand längs der Schiene bewegt werden konnte.

### 2.1. Die Wellenlängen auf der schwingenden Schiene

Zunächst wurden die Wellenlängen für die Transversalkomponenten der im Schienenkopf entlanglaufenden Wellen ermittelt. Die Messung erfolgte in üblicher Weise durch Aufsuchen der Orte gleicher Phase mit Hilfe von Lissajous-Figuren auf dem Schirm eines Kathodenstrahl-Oszillographen. Die erhaltenen Werte sind in Abb. 3 dargestellt<sup>1</sup>. Die

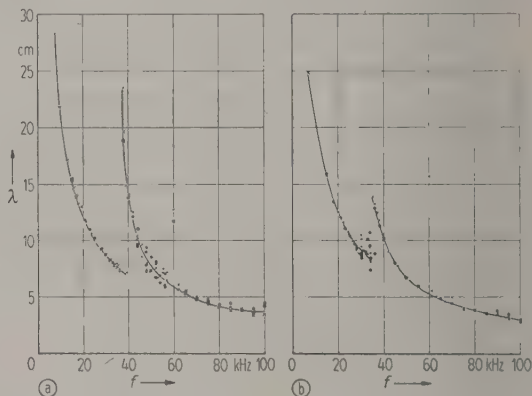


Abb. 3. Die Wellenlängen der Transversalkomponenten der im Schienenkopf entlanglaufenden Wellen als Funktion der Anregungsfrequenz; (a) senkrechte, (b) waagerechte Schwingungskomponente.

Kurven zeigen den gleichen Verlauf, wie ihn schon NAAKE gefunden hatte: Der Abfall der Wellenlänge mit zunehmender Frequenz ist infolge der frequenzabhängigen Phasengeschwindigkeit nicht rein hyperbolisch. Bei etwa 35 kHz (für beide Schwingungsrichtungen etwas verschieden) tritt für beide Komponenten ein neuer Dispersionsast auf, d. h. hier schwingt der Schienenkopf nicht mehr gleichförmig über den ganzen Querschnitt. Ein weiterer Ast ist an den Meßpunkten bei 60 kHz zu erkennen.

Die Art der Meßmethode bringt es mit sich, daß bei Überlagerung mehrerer Wellentypen stets nur die Wellenlänge der Schwingungsform gemessen wurde, die besonders stark angeregt war. Daher

<sup>1</sup> Die Punkte bezeichnen die Ergebnisse für eine Schiene aus Thomas-Stahl, die Kreuze gelten für eine aus Siemens-Martin-Stahl. Da die Härten beider bis auf etwa 2% gleich waren, unterscheiden sich die ermittelten Wellenlängen kaum voneinander.



kann man den Diagrammen zusätzlich entnehmen, daß der Schienenkopf oberhalb 35 kHz kaum mehr ohne Unterteilung schwingt, daß aber die nächst höhere Schwingungsform (ab 60 kHz) fast gar nicht angeregt wird. Genauso sind die Streuungen der Meßwerte bei einigen Frequenzen dahingehend zu deuten, daß dort zwei verschiedene Wellentypen etwa gleichstark auftreten. (An verschiedenen Orten der Schiene ergaben sich bei diesen Frequenzen durch Überlagerung verschiedene Wellenlängen.)

## 2.2 Die räumliche Amplitudenverteilung auf der schwingenden Schiene

Die Schiene wurde an einem festen Ort, z. B. am Schweißstoß, durch den Körperschall-Sender sinusförmig angeregt und die resultierende räumliche Verteilung der Schwingungsamplituden mit dem Körperschall-Mikrophon abgetastet, das mit konstanter Geschwindigkeit auf der Schiene entlanggefahren wurde.

Die gefundenen Amplitudenverteilungen haben sehr unterschiedliche Gestalt, wie aus den in Abb. 4 wiedergegebenen Ausschnitten hervorgeht. Die Reproduzierbarkeit wurde sorgfältig geprüft; dabei ergab sich, daß Verlauf und Aussehen der Amplitudenverteilung sich sofort änderten, wenn die Anregung an einem anderen, wenn auch benachbarten Ort auf der Schiene erfolgte.

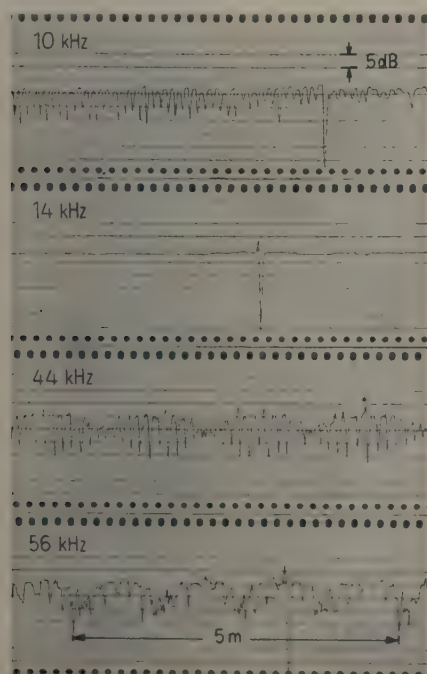


Abb. 4. Beispiele für die Verteilung der Schwingungsamplituden längs der Schiene; senkrechte Schwingungskomponente.

## 2.2.1. Die Abstände der Schwingungsmaxima

Auf den erhaltenen Pegelschreiberstreifen wurden die Abstände der Maxima ausgemessen. Waren mehrere Welligkeiten gleichzeitig vorhanden, so wurde jede von ihnen einzeln ausgezählt. Die erhaltenen Werte sind in Abb. 5 dargestellt. Durch Vergleich mit den aus einer Phasenmessung gewonnenen Wellenlängen (Abb. 3) zeigt sich, daß bei Frequenzen zwischen 10 und 20 kHz (bei den waagerechten Schwingungen bis 32 kHz) die Maxima einen Abstand von einer halben Wellenlänge besitzen, also durch Reflexionen hervorgerufen werden. Der bei 34 (bzw. 32) kHz beginnende steil ansteigende Kurvenzug läßt sich durch eine Superposition zweier mit verschiedener Phasengeschwindigkeit fortlaufender Wellen (entsprechend den ersten beiden Dispersionsästen in Abb. 3) erklären. Die übrigen noch aufgefundenen Abstände der Maxima sind keine

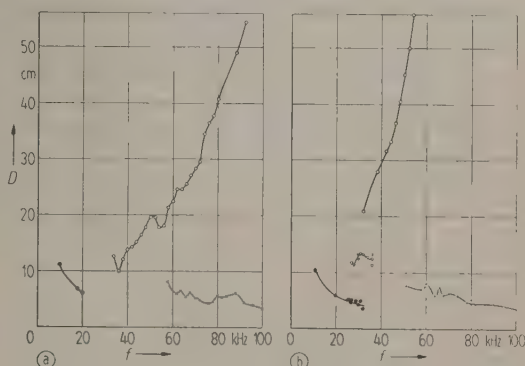


Abb. 5. Die Abstände der Schwingungsmaxima auf der Schiene; (a) senkrechte, (b) waagerechte Schwingungskomponente.

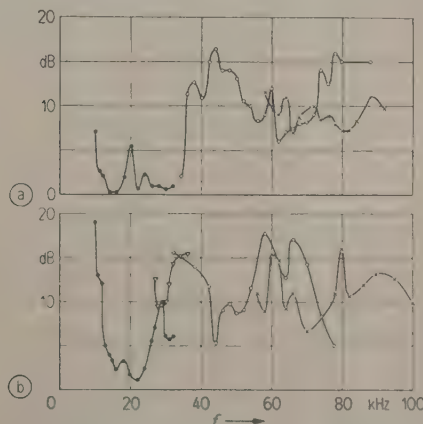


Abb. 6. Die Welligkeiten in der Schwingungsverteilung auf der Schiene; (a) senkrechte, (b) waagerechte Schwingungskomponente. Die einander entsprechenden Kurvenstücke in den Abb. 5 und 6 sind in gleicher Weise bezeichnet.



ganzzahligen Vielfachen einer halben Wellenlänge. Ihre Entstehung muß daher auf eine Überlagerung von mehreren Schwingungsformen zurückgeführt werden.

## 2.2.2. Die Welligkeit auf der schwingenden Schiene

Aus den gemessenen Amplitudenverteilungen längs der Schiene wurde ferner das Verhältnis der Maxima zu den Minima, also die Welligkeit, ermittelt, die quasi als Gewichtungsfaktor bei der Beurteilung der Abstände der Schwingungsmaxima verwendet werden muß. Diese Welligkeiten sind in Abb. 6 für die einzelnen Kurvenzüge der Abb. 5 dargestellt.

## 2.2.3. Die Dämpfung der Wellenausbreitung längs der Schiene

Die Dämpfungen der beiden Schwingungskomponenten wurden ebenfalls den registrierten Amplitudenverteilungen entnommen und sind in Abb. 7 wiedergegeben: In Übereinstimmung mit den Untersuchungen von NAAKE, der bereits im Tonfrequenzbereich einen Abfall der Dämpfung mit zunehmender Frequenz gefunden hatte, besitzt die Dämpfung im Ultraschallbereich außerordentlich niedrige Werte und bleibt im wesentlichen unterhalb 0,3 dB/m.

Es wurde ferner die Dämpfung ermittelt, die eine Welle beim Passieren einer Stoßstelle erfährt:

Für Schienen mit Stoßlücken fand NAAKE seinerzeit eine stark mit der Frequenz ansteigende Dämpfung, die bei 2,35 kHz den Wert von 21 dB pro Stoß besaß. Die hier referierten Untersuchungen hingegen wurden an lückenlosen Gleisen durchgeführt. Dabei ergab sich für Abbrennstumpfschweißungen eine kaum meßbare Dämpfung; an

Stößen, die durch Thermit-Schweißstellen verbunden waren, betrug die Dämpfung der durchgehenden Welle maximal 6 dB.

## 2.3. Deutung der Schwingungseigenschaften der Schiene

Zusammenfassend ergeben sich für die Schwingungseigenschaften der Schiene folgende Hauptmerkmale:

Die Dämpfung der in der Schiene entlanglaufenden Wellen ist im Ultraschallbereich äußerst gering und auch die Abbrennstumpfschweißungen rufen kaum einen Abfall der Amplitude hervor. Dadurch können sich irgendwelche in der Schiene, z. B. durch Schläge, angeregte Wellenzüge ungehindert ausbreiten, zumindest bis zum nächsten Thermit-Schweißstoß, an dem sie teilweise reflektiert werden.

Wird die Schiene irgendwie zum Schwingen angeregt, so zeigen sich große Welligkeiten in der Amplitudenverteilung längs der Schiene: Zu einem Teil stammen diese von Reflexionen an den Thermit-Schweißstellen her, bei höheren Frequenzen können außerdem in der Schiene gleichzeitig mehrere Schwingungsformen auftreten, die sich zu ortsfesten Schwebungen superponieren. Da die in der Schiene vorhandene Gesamtwelligkeit durch Überlagerung dieser Schwebungen mit den stehenden Wellen entsteht, muß die resultierende Amplitudenverteilung sehr stark vom Anregungsort der Schwingungen abhängen, eine Folgerung, die durch den experimentellen Befund voll bestätigt wurde (vgl. Abschnitt 2.2).

Eine Korrelation zwischen der gemessenen Amplitudenverteilung auf der Schiene und den aufgenommenen Beschleunigungsspektren bei der Überfahrt eines Zuges tritt nicht auf und war auch nicht zu erwarten: Bei der Überfahrt wird die Schiene an mehreren Stellen gleichzeitig, nämlich durch die Räder, zum Schwingen angeregt, und erst die Überlagerung sämtlicher dabei erzeugter ortsfester Amplitudenverteilungen ergibt den tatsächlich, durch den Zug verursachten Schwingungszustand der Schiene.

Ich danke Herrn Prof. Dr. E. MEYER für sein Interesse an diesen Untersuchungen und zahlreiche wertvolle Hinweise.

Die Mittel zur Durchführung der Untersuchungen wurden vom Bundesbahnzentralamt, Minden (Westf.), zur Verfügung gestellt.

(Eingegangen am 10. April 1956.)

## Schrifttum

- [1] NAAKE, H.-J., *Acustica* 3 [1953], Beiheft 1, 139 bis 147.

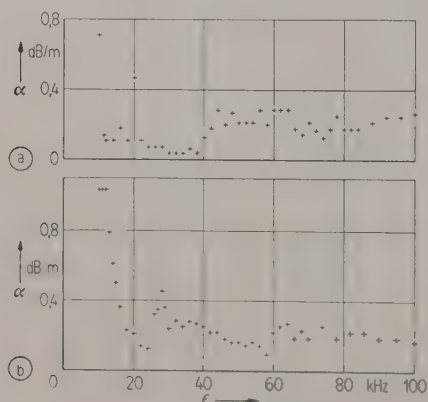


Abb. 7. Die Dämpfung einer im Schienenkopf entlanglaufenden Welle; (a) senkrechte, (b) waagerechte Schwingungskomponente.



# THEORY OF THE ACOUSTIC INTERFEROMETER FOR PLANE WAVES\*

by F. E. BORGNIS

Gordon McKay Laboratory of Applied Science, Harvard University, Cambridge, Mass., U.S.A.

## Summary

A detailed investigation is presented of the electric input impedance of a piezoelectric bar and plate, loaded at one face with the acoustic impedance of an interferometer path, and free at the opposite face. The calculations start from the basic piezoelectric equations of state and lead rigorously to the strict expression for the total electric input impedance. The various properties of this impedance are discussed for variable path length of the interferometer, for variable acoustic wavelength and for a variation of the driving electric frequency. Under ordinary experimental conditions the input impedance can be represented by means of circle diagrams. The theoretical results are illustrated by numerical examples for water at 15 Mc/s and air at 1 Mc/s.

The theory presented provides a rigorous foundation for the well known theory of the acoustic interferometer given by HUBBARD and extends it in various directions. The treatment includes the basic equations needed for the investigation of highly absorptive media.

## Sommaire

On présente une étude détaillée de l'impédance électrique d'entrée d'un barreau et d'une plaque piézoélectrique, chargés d'un côté par l'impédance acoustique d'un trajet interférométrique et libres de l'autre côté. Les calculs sont faits à partir des équations piézoélectriques fondamentales et conduisent à une expression rigoureuse de l'impédance électrique totale d'entrée. On examine les différentes propriétés de cette impédance en fonction de la longueur du trajet dans l'interféromètre, de la longueur d'onde acoustique et de la fréquence électrique d'excitation. On peut représenter l'impédance d'entrée par un diagramme circulaire, dans les conditions expérimentales habituelles. Les résultats théoriques sont illustrés par des exemples numériques relatifs à l'eau (15 MHz) et à l'air (1 MHz).

La théorie présentée constitue une base rigoureuse pour la théorie bien connue de HUBBARD relative à l'interféromètre acoustique, et peut être étendue dans différentes directions. L'exposé concerne aussi les équations fondamentales nécessaires pour étudier les milieux très absorbants.

## Zusammenfassung

Die elektrische Eingangsimpedanz eines piezoelektrischen Generators (Stab und Platte) wird ausführlich diskutiert; die eine Seite des Generators ist frei, während die andere durch die akustische Impedanz einer Interferometerstrecke belastet ist. Ausgehend von den piezoelektrischen Grundgleichungen wird ein exakter Ausdruck für die gesamte elektrische Eingangsimpedanz hergeleitet. Ihr Verhalten wird für veränderlichen Reflektorabstand, veränderliche akustische Wellenlänge und veränderliche Generatorfrequenz untersucht. Unter den üblichen experimentellen Bedingungen läßt sich die Eingangsimpedanz durch Kreisdiagramme beschreiben. Die Ergebnisse werden an zwei Beispielen für Wasser bei 15 MHz und Luft bei 1 MHz erläutert.

Die vorliegende Theorie gibt der bekannten Theorie des akustischen Interferometers nach HUBBARD eine strenge Grundlage und erweitert diese in verschiedenen Richtungen. Sie enthält auch die Ausgangsgleichungen zur Untersuchung von Medien hoher Absorption.

## PART I

### GENERAL EXPRESSIONS FOR THE ELECTRIC INPUT IMPEDANCE OF A PIEZOELECTRIC BAR AND PLATE, LOADED AT ONE SURFACE

#### 1. Introductory remarks

The acoustic interferometer is regarded as consisting of a piezoelectric crystal which is free at one face and radiates from the opposite face into the interferometer path containing the fluid or solid medium whose properties are to be studied (Fig. 1). The interferometer path ends at a plane reflector, whose

surface is parallel to the radiating face. The width of the acoustic beam is assumed so large in compa-

\* This paper is essentially based on work done under a contract between the Office of Naval Research, Washington, D.C., and the California Institute of Technology, Pasadena, Cal. (Techn. Report Nr. 3, January 25, 1952). The publication of the paper was made possible by support of the Division of Engineering and Applied Science, Harvard University.



riason with the acoustic wavelength  $\lambda$  that the wave front can be treated as plane. The piezoelectric crystal is driven by an alternating voltage  $V$  of angular frequency  $\omega = 2\pi f$ , the current to the crystal being  $I$ . The response of the interferometer to the driving voltage is completely characterized by the electric input impedance  $Z$ . Indeed, if  $Z$  is known, the response of the device in any driving electric circuit can be calculated.

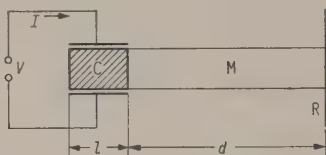


Fig. 1. Schematic outline of the acoustic interferometer. C=piezoelectric crystal of length  $l$ , M=medium filling the path of length  $d$ , R=plane reflector,  $V, I$ =voltage and current at crystal input.

The reaction of the acoustic wave-motion in the medium upon the crystal can be expressed in terms of the acoustic input impedance  $Z_m$  of the interferometer path as measured at the boundary between crystal and medium. Our first step therefore will be to calculate the electric input impedance  $Z$  of a piezoelectric crystal loaded at its radiating surface by an acoustic impedance  $Z_m$ . The opposite surface of the crystal is assumed to be free (non-radiating).

The crystal is assumed to have the shape of either a thin bar, whose breadth and thickness are small in comparison with the length, or a plate, whose linear surface dimensions are large in comparison with the thickness. The bar is regarded as driven in compressional lengthwise vibration, the plate in compressional thickness vibration.

These assumptions are those commonly made in dealing theoretically with piezoelectric bars or plates. The waves in the interferometer path are treated as plane, which implies that the dimensions of the radiating cross-section are large in comparison with the wavelength. In the case of a plate this condition is well met. In the case of a bar, however, only vibrations of high-order harmonics would meet the two conditions that the lateral dimensions are small in comparison with the length of the bar, and large in comparison with the wavelength. If the bar

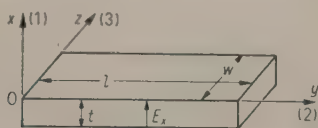


Fig. 2. Piezoelectric bar of length  $L$ , breadth  $w$  and thickness  $t$ , driven by a uniform electric field  $E_x$ .

is driven in its fundamental mode, the admissibility of assuming plane waves will depend upon experimental conditions and the nature of the desired results.

## 2. Electric input impedance of a piezoelectric bar in lengthwise vibration with an acoustic load at one face

Both the breadth  $w$  and the thickness  $t$  of the bar (Fig. 2) are supposed to be small in comparison with the length  $l$ . The ratio  $w/t$  is assumed to be large enough to ensure a practically uniform electric field  $E_x$  within the bar. The electrodes are assumed to cover the entire lateral faces of area  $A = wl$ . All surfaces except that at  $y = l$ , which is adjacent to the interferometer path, are free. Consequently all stresses except  $T_{yy} = T_2$  can be assumed to vanish everywhere ([15], p. 61);  $T_2$  vanishes at  $y = 0$ . Only displacements parallel to  $y$ , and the compressional strain  $S_2$ , need be considered.

The appropriate equations of state for a quartz X-cut bar with length parallel to a  $y$ -axis are<sup>1</sup>

$$S_2 = s_{22}^E T_2 + d_{12} E_1, \quad (1.1)$$

$$D_1 = d_{12} T_2 + \epsilon_1^T E_1. \quad (1.2)$$

For the present purpose we write  $q^E = 1/s_{22}^E$ ,  $H = d_{12}/s_{22}^E$  effective piezoelectric stress-constant;  $V = E_1 t$  is the driving voltage, assumed to be sinusoidal in time.  $E_1$  is uniform throughout the bar, but the electric displacement  $D_1$ , while uniform in the  $x$ -direction, varies in the  $y$ -direction owing to  $T_2(y)$ .

Equations (1.1) and (1.2) may now be written as follows, with subscripts omitted, for any point  $y$  along the length of the bar:

$$T = q^E S - H V/t, \quad (1.3)$$

$$D = H T/q^E + \epsilon^T V/t. \quad (1.4)$$

Since these equations are linear and  $V$  is sinusoidal, the instantaneous values of  $T$ ,  $S$ , and  $D$  are sinusoidal in time as well as being functions of  $y$ . In what follows, time-dependence will be represented by the factor  $e^{j\omega t}$ , which itself is suppressed.

The equation of motion, in Lagrangian coordinates, for a plane compressional wave with displacement  $\eta$  in the  $y$ -direction, is

$$\rho_c \frac{\partial^2 \eta}{\partial t^2} = \frac{\partial T(y)}{\partial y} \quad (1.5)$$

or, since  $\partial/\partial t = j\omega$ ,

$$-\omega^2 \rho_c \eta = \partial T/\partial y. \quad (1.6)$$

<sup>1</sup> See [6], p. 67 and [7], p. 580; also [2]. For other crystals than quartz suitable changes in subscripts can be made ([6] and [7]). Numerical values for quartz are given in Appendix A.



From eqs. (1.6) and (1.3),

$$\frac{\partial^2 T}{\partial y^2} = -\omega^2 \varrho_c \frac{\partial \eta}{\partial y} = -\omega^2 \varrho_c S = -\omega^2 \varrho_c \left( \frac{T}{q^E} + \frac{H V}{q^E t} \right)$$

or 
$$\frac{\partial^2 T}{\partial y^2} + \frac{\omega^2 \varrho_c}{q^E} T = -\frac{\omega^2 \varrho_c}{q^E} \frac{H V}{t} \quad (1.7)$$

Introducing  $\gamma_c^2 = \omega^2 \varrho_c / q^E$ , we get

$$\frac{\partial^2 T}{\partial y^2} + \gamma_c^2 T = -\gamma_c^2 \frac{H V}{t} \quad (1.8)$$

In general  $\gamma_c$  is complex. The losses in the crystal are included in the complex stiffness  $q^E$ . They are treated in the same way as the losses due to viscosity in fluids.

Setting 
$$q^E = q_{c0} + j \omega F, \quad (1.9)$$

where  $q_{c0}$  is real, we have

$$\gamma_c^2 = \frac{\omega^2 \varrho_c}{q_{c0} + j \omega F} \quad (1.10)$$

For small losses ( $\omega F \ll q_{c0}$ ), we may write

$$\gamma_c \approx \omega \sqrt{\frac{\varrho_c}{q_{c0}}} \left( 1 - \frac{j \omega F}{2 q_{c0}} \right),$$

or, introducing the crystal phase velocity  $c_c = \sqrt{q_{c0} / \varrho_c}$  and, as usual, a space-attenuation constant  $\alpha$ , we have

$$\gamma_c \approx \frac{\omega}{c_c} - j \alpha = \frac{2 \pi}{\lambda_c} - j \alpha. \quad (1.11)$$

Although the crystal losses are treated as small, still eq. (1.11) can be regarded as correct for large losses also; but in this case the phase velocity  $c_c$  and the acoustic wavelength  $\lambda_c$  in the crystal are functions of  $\omega$  and  $F / q_{c0}$ , as is found by taking the square root of eq. (1.10).

Further losses can arise if imaginary components of  $H$  and  $\varepsilon^T$  are taken into account. Within the range of frequencies observed so far, no such imaginary component of  $H$  — due for instance to relaxation effects — seems to be indicated and we therefore regard  $H$  as real. A complex  $\varepsilon^T$  would imply dielectric losses in the crystal. For quartz, at least, these losses are extremely small. We shall treat  $\varepsilon^T$  as real; the imaginary component could be introduced if necessary.

The solution of eq. (1.8) for  $T$  can be written

$$T = a \sin(\gamma_c y + \vartheta) - H V / t. \quad (1.12)$$

The constants  $a$  and  $\vartheta$  are determined by the boundary conditions. At the free surface  $y = 0$  the stress  $T$  vanishes. From (1.12) we have therefore

$$a \sin \vartheta = H V / t. \quad (1.13)$$

At the opposite surface  $y = l$  the crystal is in contact with the medium in the interferometer path. The reaction of the medium upon the crystal can be characterized by the acoustic input impedance  $Z_m$

of the interferometer path, which is defined in the usual way by

$$Z_m = p(l) / u(l), \quad (1.14)$$

$p(l)$  representing the excess pressure and  $u(l)$  the particle-velocity at the boundary between crystal and medium. Both pressure and particle-velocity must be continuous at this boundary. Since a stress is usually called positive when extensional, whereas a pressure is called positive when compressional, we write  $p(l) = -T(l)$ . Furthermore,  $u = \partial \eta / \partial t = j \omega \eta$ . Thus the boundary condition at  $y = l$  can be written

$$T(l) / \eta(l) = -j \omega Z_m. \quad (1.15)$$

The expression for  $Z_m$  will be computed in Part III, Section 1. From eqs. (1.6) and (1.12)  $\eta$  is found to be

$$\eta = -\frac{1}{\gamma_c q^E} a \cos(\gamma_c y + \vartheta),$$

and, introducing  $\varphi = \gamma_c l$ , we obtain by eqs. (1.12) and (1.15)

$$\frac{a \sin(\varphi + \vartheta) - H V / t}{a \cos(\varphi + \vartheta)} = \frac{j \omega}{\gamma_c q^E} Z_m.$$

It is convenient to introduce here the dimensionless quantity

$$z_m = \omega Z_m / \gamma_c q^E. \quad (1.16)$$

Thus we obtain

$$a \sin(\varphi + \vartheta) = \frac{H V}{t} + j a z_m \cos(\varphi + \vartheta). \quad (1.17)$$

By developing  $\sin(\varphi + \vartheta)$  and  $\cos(\varphi + \vartheta)$  in terms of  $\sin \varphi$  and  $\cos \varphi$  and replacing  $a \sin \vartheta$  by means of eq. (1.13), we find by a short calculation

$$a \cos \vartheta = \frac{H V}{t} \frac{1 - \cos \varphi - j z_m \sin \varphi}{\sin \varphi - j z_m \cos \varphi}. \quad (1.18)$$

In order to establish a relation between the current  $I$  and the voltage  $V$ , which will lead to the electric input admittance  $Y$ , we integrate eq. (1.4) with respect to  $y$  :

$$\int_0^l D \, dy = \frac{H}{q^E} \int_0^l T \, dy + \varepsilon^T \frac{V l}{t}. \quad (1.19)$$

The displacement-current  $I$  through the crystal is given by

$$I = w \int_0^l \frac{\partial D}{\partial t} \, dy = j \omega w \int_0^l D \, dy. \quad (1.20)$$

From (1.12) we find

$$\begin{aligned} \int_0^l T \, dy &= \frac{a}{\gamma_c} [\cos \vartheta (1 - \cos \varphi) + \\ &\quad + \sin \vartheta \sin \varphi] - \frac{H V l}{t}. \end{aligned} \quad (1.21)$$



Replacing  $a \sin \vartheta$  and  $a \cos \vartheta$  by eqs. (1.13) and (1.18) and inserting (1.20) and (1.21) into (1.19), we find finally, with  $\gamma_c = \varphi/l$ ,

$$I = j \omega V \varepsilon^T \left( 1 - \frac{H^2}{\varepsilon^T q^E} \right) \frac{A}{t} + j \frac{2 \omega A H^2 V \tan \varphi/2 - j z_m/2}{\varphi q^E t (1 - j z_m \cot \varphi)}.$$

The input admittance  $Y$  of the crystal is defined by  $I = YV$  and is found immediately from this equation to be

$$Y = j \omega C_1 + j \omega \frac{2 A H^2 \tan \varphi/2 - j z_m/2}{\varphi q^E t (1 - j z_m \cot \varphi)} \quad (1.22)$$

where 
$$C_1 = \varepsilon^T \left( 1 - \frac{H^2}{\varepsilon^T q^E} \right) \frac{A}{t} \quad (1.23)$$

The admittance  $Y$  can be represented by the electric circuit shown in Fig. 3.  $C_1$  is the parallel capacitance of the crystal, with an effective permittivity

$$\varepsilon = \varepsilon^T \left( 1 - \frac{H^2}{\varepsilon^T q^E} \right). \quad (1.23 a)$$

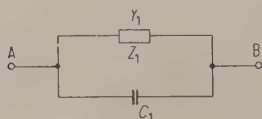


Fig. 3. Equivalent electric circuit for the loaded piezoelectric crystal.

The impedance of the branch in parallel with  $C_1$  is given by

$$Z_1 = \frac{1}{Y_1} = j \frac{\varphi q^E t}{2 \omega A H^2 \tan \varphi/2 - j z_m/2} \quad (1.24)$$

Eq. (1.24) is the rigorous expression for the electric input impedance (or admittance) of a piezoelectric bar, loaded at one end with an acoustic impedance  $Z_m$  (expressed by  $z_m$ ). By including imaginary parts of the quantities  $\varphi$ ,  $q^E$ ,  $\varepsilon^T$ , and  $H$  in eqs. (1.22), (1.23) and (1.24), all conceivable losses in the crystal can be taken into account.

### 3. Electric input impedance of a piezoelectric plate in thickness vibration with an acoustic load at one face

The piezoelectric plate (Fig. 4) is assumed to be infinitely extended in the  $y$ - and  $z$ -directions. The acoustic wave motion is treated as a plane problem ( $\partial/\partial y = \partial/\partial z = 0$ ), the only displacement  $\xi$  being in the  $x$ -direction and the only strain being  $S_1$ . In a finite plate other strain-components, together with all six stress-components, may be present, de-

pending on the piezoelectric and elastic coefficients of the particular crystal; they are disregarded in the present treatment. It will therefore be assumed that associated with the strain  $S_1$ , only the single stress  $T_1$  need be considered.

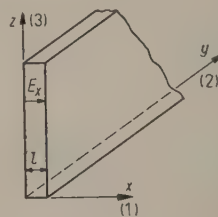


Fig. 4. Piezoelectric plate of thickness  $l$ , driven by an electric field  $E_x$ .

The equations of state for a quartz  $X$ -cut plate then become ([7], p. 580; [2])

$$T_1 = c_{11}^E S_1 - e_{11}^E E_1, \quad (1.25)$$

$$D_1 = e_{11}^S S_1 + \varepsilon_1^S E_1. \quad (1.26)$$

Owing to the polarization produced by the strain  $S_1(x)$ , the electric field  $E_1$  is a function of  $x$  over the thickness  $l$  of the plate. The electric displacement  $D_1$ , however, is independent of  $x$ , as no free space charge exists within the plate. We write eqs. (1.25) and (1.26) in the simplified form

$$T = q^E S - H E, \quad (1.27)$$

$$D = H S + \varepsilon^S E. \quad (1.28)$$

These equations for the plate are similar to eqs. (1.3) and (1.4) for the bar. The numerical values of the constants, however, are in general not the same as for the bar (see Appendix A).

Proceeding in the same way as in the case of the bar, we shall establish the differential equation for  $T$ . It is desirable to use the electrical parameter  $D$ , which is independent of  $x$ , instead of  $E$ . By eliminating  $E$  between eqs. (1.27) and (1.28) one finds

$$T = q^E \left( 1 + \frac{H^2}{\varepsilon^S q^E} \right) S - \frac{H}{\varepsilon^S} D. \quad (1.29)$$

Introducing

$$q^D = q^E \left( 1 + \frac{H^2}{\varepsilon^S q^E} \right) \quad (1.30)$$

we have

$$T = q^D S - \frac{H}{\varepsilon^S} D. \quad (1.31)$$

By a procedure analogous to that used in deriving eq. (1.8), we obtain

$$\frac{\partial^2 T}{\partial x^2} + \gamma_c^2 T = - \gamma_c^2 \frac{H}{\varepsilon^S} D, \quad (1.32)$$

where, in the case of the plate,  $\gamma_c^2 = \omega^2 \rho_c / q^D$ .



Applying the same boundary conditions<sup>2</sup> as in eq. (1.15) at  $x=l$  and the condition  $T=0$  at  $x=0$ , we obtain the solution for  $T$  corresponding to eq. (1.32):

$$T = a \sin(\gamma_c x + \vartheta) - \frac{H}{\epsilon^S} D. \quad (1.33)$$

The two equations determining the constants of integration  $a$  and  $\vartheta$  are found from the boundary conditions; they are

$$a \sin \vartheta = \frac{H}{\epsilon^S} D \quad (1.34)$$

and

$$a \sin(\varphi + \vartheta) = \frac{H}{\epsilon^S} D + j a z_m \cos(\varphi + \vartheta), \quad (1.35)$$

where

$$z_m = \frac{\omega Z_m}{\gamma_c q^D} \quad \text{and} \quad \varphi = \gamma_c l. \quad (1.36)$$

From eq. (1.35) it follows by means of eq. (1.34) that

$$a \cos \vartheta = \frac{H D}{\epsilon^S} \frac{1 - \cos \varphi - j z_m \sin \varphi}{\sin \varphi - j z_m \cos \varphi}. \quad (1.37)$$

On eliminating  $S$  between eqs. (1.27) and (1.28) we find

$$T = -\left(H + \frac{\epsilon^S q^E}{H}\right) E + \frac{q^E D}{H} \quad (1.38)$$

and integrating eq. (1.38) with respect to  $x$ , we have

$$\int_0^l T dx = -\left(H + \frac{\epsilon^S q^E}{H}\right) V + \frac{q^E D l}{H}. \quad (1.39)$$

On the other side we find from eq. (1.33)

$$\int_0^l T dx = \frac{1}{\gamma_c} [a \cos \vartheta (1 - \cos \varphi) + a \sin \vartheta \sin \varphi] - \frac{H D}{\epsilon^S}. \quad (1.40)$$

Inserting  $a \sin \vartheta$  and  $a \cos \vartheta$  from eqs. (1.34) and (1.37) we obtain after a short calculation

$$\int_0^l T dx = \frac{2 H D}{\gamma_c \epsilon^S} \frac{\tan \varphi/2 - j z_m/2}{1 - j z_m \cot \varphi} - \frac{H D l}{\epsilon^S}. \quad (1.41)$$

Introducing this result into eq. (1.39), we get

$$\left(H + \frac{\epsilon^S q^E}{H}\right) V = \frac{D l}{\epsilon^S} \left(H + \frac{\epsilon^S q^E}{H}\right) - \frac{2 H D}{\gamma_c \epsilon^S} \frac{\tan \varphi/2 - j z_m/2}{1 - j z_m \cot \varphi}.$$

<sup>2</sup> The metallic coating on the plate is assumed to be so thin that its acoustic impedance is negligible.

Now, by eq. (1.30)

$$H + \frac{\epsilon^S q^E}{H} = H + \frac{\epsilon^S}{H} \left(q^D - \frac{H^2}{\epsilon^S}\right) = \frac{\epsilon^S q^D}{H},$$

and we find, introducing the current  $I = j \omega D A$ ,

$$V = \frac{I l}{j \omega A \epsilon^S} - \frac{2 H^2 l I}{j \varphi \omega A (\epsilon^S)^2 q^D} \frac{\tan \varphi/2 - j z_m/2}{1 - j z_m \cot \varphi} = I Z,$$

where  $Z$ , the input impedance of the crystal is

$$Z = \frac{1}{j \omega C_1} \left(1 - \frac{2 H^2}{\varphi \epsilon^S q^D} \frac{\tan \varphi/2 - j z_m/2}{1 - j z_m \cot \varphi}\right) \quad (1.42)$$

with

$$C_1 = A \epsilon^S / l. \quad (1.43)$$

According to eq. (1.42) the impedance  $Z$  can be represented by the equivalent circuit of Fig. 5, where

$$Z_1 = \frac{j}{\omega C_1} \frac{2 H^2}{\varphi \epsilon^S q^D} \frac{\tan \varphi/2 - j z_m/2}{1 - j z_m \cot \varphi}. \quad (1.44)$$

Eq. (1.42) gives rigorously the electric input impedance of a plate in thickness vibration; as in the case of the bar, all conceivable losses are included, if  $\varphi$ ,  $q^D$ ,  $H$ , and  $\epsilon^S$  are regarded as complex quantities.

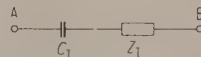


Fig. 5. Equivalent electric series circuit for the loaded piezoelectric plate.

Although Fig. 5 corresponds to the simplest analytical expression for the impedance of the crystal plate, as given by eq. (1.42), it is of advantage in many cases to transform the circuit of Fig. 5 into the more usual form shown in Fig. 3. It can easily be shown that the two circuits are equivalent in that they represent at all frequencies the same input impedance or admittance with respect to the points A and B, if the following relations exist:

$$Z_1 = \frac{1 + j \omega C_1 Z_1}{\omega^2 C_1^2 Z_1}; \quad C_1 = C_1. \quad (1.45)$$

Inserting  $Z_1$  from eq. (1.44) and  $C_1 = C_1$  from eq. (1.43) into eq. (1.45) we obtain after a short calculation

$$Z_1 = \frac{\varphi q^D l}{2 \omega A H^2} \left(1 - \frac{H^2}{\epsilon^S q^D} \frac{\tan \varphi/2 - j(z_m/2)}{\varphi/2} \left(2 \cot \varphi - \frac{2 H^2}{\varphi \epsilon^S q^D}\right) \frac{1}{j \tan \varphi/2 + z_m/2}\right). \quad (1.46)$$

As already stated, the expression for  $Z_1$  is more complicated than that for  $Z_I$ . For the crystals commonly used, however, the quantity  $|H^2/\epsilon^S q^D|$  is small in comparison with unity; this fact permits a simplification of eq. (1.46).



## PART II

### ELECTRIC INPUT IMPEDANCE OF THE FREE PIEZOELECTRIC BAR AND PLATE

#### 1. The free bar

The formulas for a free crystal, that is in absence of any external load, follow immediately from the previous general formulas. If the surface at  $y=l$  is free, the stress  $T(l)$  vanishes. Therefore in eq. (1.15), the condition that  $T(l)=0$  is equivalent to  $Z_m=0$  and  $z_m=0$  according to eq. (1.16) for a bar and (1.36) for a plate. Thus we obtain the impedance  $Z_1$  for the free bar, corresponding to the upper branch of the equivalent circuit in Fig. 3, by setting  $z_m=0$  in eq. (1.24):

$$Z_{1c} = -j \frac{q^E t}{\omega A H^2} \frac{\varphi}{2} \cot \frac{\varphi}{2}. \quad (2.1)$$

Usually this impedance is represented in the neighbourhood of the series resonance  $\omega_s$  by the circuit shown in Fig. 6. Series resonance occurs when the imaginary part of  $Z_1$  vanishes, or, in terms of  $C$  and  $L$ , when  $\omega_s^2 C L = 1$ .

With

$$\varphi = \gamma_c l = \frac{\omega l}{c_c} - j \alpha l$$

and regarding the losses in the crystal as small so that  $\alpha l \ll 1$ , we have

$$\frac{\varphi}{2} \cot \frac{\varphi}{2} = \left( \frac{\omega l}{2 c_c} - j \frac{\alpha l}{2} \right) \cot \left( \frac{\omega l}{2 c_c} - j \frac{\alpha l}{2} \right)$$

or, retaining only first-order terms in  $\alpha l/2$  and developing the cot-term,

$$\frac{\varphi}{2} \cot \frac{\varphi}{2} = \frac{\omega l}{2 c_c} \cot \frac{\omega l}{2 c_c} - j \frac{\alpha l}{2} \left[ \cot \frac{\omega l}{2 c_c} - \frac{\omega l/2 c_c}{\sin^2(\omega l/2 c_c)} \right] + \dots \quad (2.2)$$

The imaginary part of  $Z_1$  therefore vanishes when  $\cot(\omega l/2 c_c) = 0$

$$\text{or} \quad \omega_s l/2 c_c = (2n+1) \pi/2, \quad (2.3)$$

where  $n=0, 1, 2, 3, \dots$ . Thus, as is well known, series resonance for the bar occurs at

$$\omega_s = (2n+1) \pi c_c/l. \quad (2.4)$$

The real part of  $Z_1$ , representing the resistance  $R_b$  of the bar at resonance, follows from eqs. (2.2), (2.3), and (2.1)<sup>3</sup>:

$$(R_b)_{\omega=\omega_s} = \alpha l \frac{q^E t l}{4 A H^2 c_c}. \quad (2.5)$$

<sup>3</sup> The consideration of small imaginary parts of  $q^E$  or  $H$  would only lead to corrections in second order terms and can therefore be omitted.

As seen from eq. (2.2) the real part of  $Z_1$  is a function of  $\omega$ ; this means that  $R_b$  varies with  $\Delta\omega = \omega - \omega_s$ . But as  $\alpha l$  is assumed to be small, terms of order  $\alpha l \cdot \Delta\omega$  can be ignored near resonance, and  $R_b$  can be regarded as a constant as is commonly the case.

The quantities  $L_b$  and  $C_b$  for the bar in Fig. 6 are found from eqs. (2.1) and (2.3) by using the relations<sup>4</sup>

$$L_b = \frac{1}{2} \left| \frac{dZ_1}{d\omega} \right|_{\omega=\omega_s} \quad \text{and} \quad C_b = \frac{1}{\omega_s^2 L_b}. \quad (2.6)$$

After short calculations one finds easily

$$L_b = \frac{q^E t l^2}{8 A H^2 c_c^2} \quad (2.7)$$

$$\text{and} \quad C_b = \frac{8 A H^2}{\pi^2 q^E t} \frac{1}{(2n+1)^2},$$

in agreement with the well-known values of these quantities ([5], p. 297).

Antiresonance is here defined as occurring when the imaginary part of the total admittance  $Y$  becomes zero, that is, when  $\text{Im}(j \omega C_1 + 1/Z_1) = 0$  (see Fig. 3). Disregarding terms of order higher than  $\alpha l$ , the angular frequency  $\omega_a$  for antiresonance follows from eqs. (2.1), (2.2), and (1.23):

$$\frac{\omega_a l}{2 c_c} \cot \frac{\omega_a l}{2 c_c} = - \frac{H^2}{\varepsilon^T q^E - H^2}. \quad (2.8)$$

Assuming that  $H^2/\varepsilon^T q^E \ll 1$ , and moreover that  $\omega_a l/2 c_c$  is very close to  $(2n+1) \pi/2$ , we can write

$$\frac{\omega_a l}{2 c_c} = (2n+1) \frac{\pi}{2} + \delta_b \quad (H^2/\varepsilon^T q^E \ll 1).$$

Then after a short calculation it is found from eq. (2.8) that

$$\delta_b \approx \frac{2 H^2}{(2n+1) \pi \varepsilon^T q^E} \ll 1 \quad (H^2/\varepsilon^T q^E \ll 1). \quad (2.9)$$

From eqs. (2.3), (2.9), and (2.10) it is seen that

$$\omega_a - \omega_s \approx 2 c_c \frac{\delta_b}{l} = \frac{H^2}{\varepsilon^T q^E} \frac{4 \omega_s}{(2n+1)^2 \pi^2}. \quad (2.10)$$

This is the difference in angular frequency between antiresonance and series resonance for a free bar. For the usual crystals it is a very small quantity (see Appendix A.1).

<sup>4</sup> Since  $Z_1$  is represented in the neighbourhood of resonance by  $Z_1 = j \omega L_b + 1/j \omega C_b + R_b$ ,  $dZ_1/d\omega = j(L_b + 1/\omega^2 C_b)$ , and since  $\omega_s^2 L_b C_b = 1$ ,  $|dZ_1/d\omega|_{\omega=\omega_s} = 2 L_b$ .

In the foregoing treatment, as well as in what follows, the effect of the electric circuit (matching network, generator, etc.) is disregarded. So far as the use of a crystal in the interferometer is concerned, the theory shows that only crystal-resonance is of interest. Therefore no heed will be given to the characteristics of the external electric circuit.

## 2. The free plate

The impedance  $Z_1$  corresponding to Fig. 3 for this case is obtained from eq. (1.46) if we set  $z_m = 0$ . We find

$$Z_{1c} = -j \frac{q^D l}{\omega A H^2} \left( \frac{\varphi}{2} \cot \frac{\varphi}{2} - \frac{H^2}{\epsilon^S q^D} \right). \quad (2.11)$$

The term  $H^2/\epsilon^S q^D$  may be attributed to the effect of polarization, which makes the electric field  $E_x$  vary along the  $x$ -direction (Fig. 4). Such an effect does not occur in the bar, where the electric field is perpendicular to the direction of mechanical vibration. As already mentioned,  $H^2/\epsilon^S q^D$  is a small quantity for the crystals commonly in use. When this term is neglected, the expression for  $Z_1$  in eq. (2.11) has the same form as the expression for the free bar in eq. (2.1).

Series resonance for the free plate occurs, according to eq. (2.11) when<sup>5</sup>

$$\operatorname{Re} \left[ \frac{q^D}{H^2} \left( \frac{\varphi}{2} \cot \frac{\varphi}{2} - \frac{H^2}{\epsilon^S q^D} \right) \right] = 0. \quad (2.12)$$

For small losses ( $\alpha l \ll 1$ ) we make use of the same development of  $(\varphi/2) \cot(\varphi/2)$  that led to eq. (2.2). Assuming that the imaginary parts of  $q^D/H^2$  and of  $\epsilon^S$  are small quantities, we find the condition for series resonance to be

$$\frac{\omega_s l}{2 c_c} \cot \frac{\omega_s l}{2 c_c} = \operatorname{Re} \left( \frac{H^2}{\epsilon^S q^D} \right). \quad (2.13)$$

A simple approximate solution of this equation follows under the assumption that  $\operatorname{Re}(H^2/\epsilon^S q^D) \ll 1$ , by setting  $\omega_s l/2 c_c = (2n+1)(\pi/2) - \delta_p$ , where  $\delta_p$  is a small quantity. Retaining only first order terms in  $\delta_p$  and ignoring an imaginary part of  $H^2/\epsilon^S q^D$ , we find from eq. (2.13):

$$\delta_p = \frac{2}{(2n+1)\pi} \frac{H^2}{\epsilon^S q^D}. \quad (2.14)$$

<sup>5</sup> Eq. (2.12) is identical with the result obtained by a different approach by R. BECHMANN in his theory of the vibrating plate ([1], eq. 41). BECHMANN's corrective term in  $q^D$  ( $c' - c$  in his notation, eq. (32 a)), however, is too great by a factor 2, due to the omission of a factor 1/2 in his expression for the piezoelectric interaction-potential  $\psi$  (in BECHMANN's notation); see also R. BECHMANN [2 a].

Thus series resonance for the plate occurs at<sup>6</sup>

$$\omega_s = (2n+1) \frac{\pi c_c}{l} - \frac{4 c_c}{(2n+1)\pi l} \frac{H^2}{\epsilon^S q^D}. \quad (2.15)$$

$$(H^2/\epsilon^S q^D \ll 1).$$

The real part of  $Z_1$ , representing the loss-resistance  $R_p$  (Fig. 6) for the plate, is found in the same way as for the bar. From eqs. (2.11), (2.12), (2.14), and using the development eq. (2.2) for small losses, we obtain by a short calculation, assuming  $\alpha l \ll 1$  and  $\delta_p \ll 1$ ,

$$(R_p)_{\omega = \omega_s} = \alpha l \frac{q^D l^2}{4 A H^2 c_c}. \quad (2.16)$$

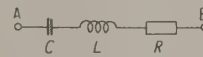


Fig. 6. Representation of  $Z_1$  in Fig. 3 near resonance by  $C$ ,  $L$  and  $R$  in series.

The quantities  $L_p$  and  $C_p$  for the plate, corresponding to the equivalent network of Fig. 6, are obtained by using eq. (2.6). Neglecting terms in  $\delta_p$ , we have

$$L_p = \frac{q^D l^3}{8 A H^2 c_c^2} \quad (2.17)$$

and

$$C_p = \frac{8 A H^2}{\pi^2 q^D l} \frac{1}{(2n+1)^2},$$

in agreement with the well known values of these quantities ([5], p. 323).

Antiresonance of the free plate occurs when  $\operatorname{Im}(1/Z_1 + j\omega C_1) = 0$ . From eqs. (2.11), (1.43), and (1.45) we obtain

$$\operatorname{Re} \left( \frac{\varphi}{2} \cot \frac{\varphi}{2} \right) = 0$$

and for small losses, replacing  $\frac{\varphi}{2} \cot \frac{\varphi}{2}$  by eq. (2.2), we find

$$\omega_a l/2 c_c = (2n+1)\pi/2. \quad (2.18)$$

From eqs. (2.15) and (2.18) it is seen that for a free plate the difference in angular frequency between series resonance and antiresonance is  $(2c_c/l)\delta_p$ , where  $\delta_p$  is given by eq. (2.14) when  $H^2/\epsilon^S q^D \ll 1$ . Thus<sup>7</sup>

$$\omega_a - \omega_s = \frac{H^2}{\epsilon^S q^D} \frac{4 \omega_a}{(2n+1)^2 \pi^2} \quad (H^2/\epsilon^S q^D \ll 1). \quad (2.19)$$

<sup>6</sup> It is easily shown that eq. (2.15) agrees with BECHMANN's expression for series resonance, as given in [1], also in [5], p. 314.

<sup>7</sup> Eq. (2.19) agrees with BECHMANN's results, [1], eqs. (61) and (61 a).



### PART III

## MECHANICAL AND ELECTRICAL IMPEDANCE OF THE INTERFEROMETER PATH

#### 1. Mechanical impedance of the interferometer path

The mechanical input impedance of the interferometer path at the radiating boundary of the crystal is by definition, eq. (1.14),

$$(Z_m)_{x=-d} = -\frac{T(-d)}{u(-d)} = \frac{p(-d)}{u(-d)}, \quad (3.1)$$

if we choose the coordinate system of the interferometer path as indicated in Fig. 7.  $T$ ,  $p$ , and  $u$  denote stress, excess pressure, and particle velocity of the medium in the path. R is a plane reflector parallel to the crystal boundary. The differential equation

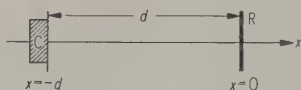


Fig. 7. Simplified sketch of interferometer with crystal C at  $x = -d$  and reflector R at  $x = 0$ .

for a plane compressional wave motion, in Lagrangian coordinates (displacement  $\xi$ ), is

$$\varrho_m \frac{\partial^2 \xi}{\partial t^2} = -\omega^2 \varrho_m \xi = \frac{\partial T}{\partial x} = -\frac{\partial p}{\partial x} = q_m \frac{\partial^2 \xi}{\partial x^2} \quad (3.2)$$

where  $\varrho_m$  is the density and  $q_m$  the stiffness of the medium. To include the losses we assume  $q_m$  to be complex:

$$q_m = q_{m0} + j \omega F_m. \quad (3.3)$$

The solution of eq. (3.2) is

$$\xi(x) = \xi_0 (e^{-j\gamma_m x} + \Gamma e^{j\gamma_m x}), \quad (3.4)$$

where 
$$\gamma_m^2 = \left( \frac{\omega}{c_m} - j \alpha_m \right)^2 = \omega^2 \frac{\varrho_m}{q_m}. \quad (3.5)$$

The phase velocity of the plane waves according to the solution eq. (3.4) is, by definition,  $c_m = \omega / \text{Re}(\gamma_m)$ . If the losses in the medium are assumed to be small,  $c_m$  can be expressed by

$$c_m^2 = q_{m0} / \varrho_m \quad (\omega F_m \ll q_{m0}). \quad (3.6)$$

The quantity  $\Gamma$  in eq. (3.4) is the reflection coefficient of the reflector R. The particle velocity  $u = \partial \xi / \partial t = j \omega \xi$  at the reflector ( $x = 0$ ) is given by eq. (3.4):

$$(u)_{x=0} = j \omega \xi_0 (1 + \Gamma). \quad (3.7)$$

If we construe the two terms in eq. (3.4) as belonging to two wave components progressing in the positive and negative  $x$ -directions, the ratio of the particle velocity  $u_+$  of the positive wave to  $u_-$  of the

negative wave at the reflector is given, according to eq. (3.7), by

$$\left( \frac{u_+}{u_-} \right)_{x=0} = \Gamma = |\Gamma| e^{j\Theta}. \quad (3.8)$$

In general  $\Gamma$  is complex; the modulus  $|\Gamma|$  indicates the diminution of the reflected wave-amplitude with respect to the incident amplitude, and is associated with the energy absorption in the reflector. The phase angle  $\Theta$  indicates the "phase-jump" which the reflected wave undergoes with respect to the incident wave. For a perfectly rigid reflector  $(u)_{x=0}$  is zero by definition, and therefore  $\Gamma = -1$  (or  $|\Gamma| = 1$  and  $\Theta = \pi$ )<sup>8</sup>.

The stress  $T = q_m \partial \xi / \partial x$  is, according to eq. (3.4),

$$T(x) = -j \gamma_m q_m \xi_0 (e^{-j\gamma_m x} - \Gamma e^{j\gamma_m x}). \quad (3.9)$$

Thus the mechanical input impedance  $Z_m$ , as defined in eq. (3.1), is found by using eqs. (3.4) and (3.9) at  $x = -d$ :

$$Z_m = -\frac{T}{j \omega \xi} = \frac{\gamma_m q_m}{\omega} \frac{1 - \Gamma e^{-2j\gamma_m d}}{1 + \Gamma e^{-2j\gamma_m d}}. \quad (3.10)$$

Introducing the dimensionless quantity

$$r = \Gamma e^{-2j\gamma_m d} \quad (3.11)$$

we have, at  $x = -d$ ,

$$Z_m = \frac{\gamma_m q_m}{\omega} \frac{1 - r}{1 + r}. \quad (3.12)$$

The dimensionless quantity  $z_m$  in eq. (1.16) for the bar and eq. (1.36) for the plate becomes

$$z_m = \frac{\omega}{\gamma_c q_c} Z_m = \frac{\gamma_m q_m}{\gamma_c q_c} \frac{1 - r}{1 + r}, \quad (3.13)$$

where  $q_c = q^E$  is the stiffness of the bar, and  $q_c = q^D$  is that of the plate. We introduce

$$m = m_0 + j m_1 = \frac{\gamma_m q_m}{\gamma_c q_c} \quad (3.14)$$

<sup>8</sup> The suggestion is sometimes found in the literature that some kind of "reflection-losses" may occur also at the boundary between crystal and medium and that such losses might affect the value of  $\Gamma$ . There is no room, however, for such considerations within the scope of the theory given here. The boundary conditions at the interface between crystal and medium require continuity of pressure and displacement in the two adjacent media. Nothing else has to be introduced. The situation would be different if dissipation by heat transfer or surface layers due to impurities were taken into account; but such effects are beyond the scope of the theory treated here.

and have 
$$z_m = m \frac{1-r}{1+r} \quad (3.15)$$

From eq. (3.5) and the expression preceding eq. (1.8), the quantity  $m$  can be expressed by

$$m = \frac{\gamma_m q_m}{\gamma_c q_c} = \sqrt{\frac{\varrho_m q_m}{\varrho_c q_c}} = \sqrt{\frac{\varrho_m q_{m0}(1+j\omega F_m/q_{m0})}{\varrho_c q_{c0}(1+j\omega F_c/q_{c0})}}$$

or 
$$m = m_0 + j m_1 = \frac{\varrho_m c_m}{\varrho_c c_c} \sqrt{\frac{1+j\omega F_m/q_{m0}}{1+j\omega F_c/q_{c0}}} \quad (3.16)$$

If the losses in both crystal and medium are small, we can write

$$m - m_0 + j m_1 = \frac{\varrho_m c_m}{\varrho_c c_c} \left[ 1 + \frac{j\omega}{2} \left( \frac{F_m}{q_{m0}} - \frac{F_c}{q_{c0}} \right) \right],$$

where

$$m_0 = \frac{\varrho_m c_m}{\varrho_c c_c}, \quad (\omega F_m \ll q_{m0}) \quad (3.17)$$
$$m_1 = \frac{\omega m_0}{2} \left( \frac{F_m}{q_{m0}} - \frac{F_c}{q_{c0}} \right). \quad (\omega F_c \ll q_{c0})$$

The quantity  $m_1$  can also be expressed by introducing the space-attenuation parameter  $\alpha$ , as defined by eqs. (1.11) and (3.5):

$$m_1 = \frac{m_0}{\omega} (c_m \alpha_m - c_c \alpha_c). \quad (3.17 a)$$

## 2. Electrical impedance associated with the interferometer path

The impedance  $Z_1$ , as given in the general form of eqs. (1.24) and (1.46) for the bar and the plate, can be thought of as containing two parts: one belonging to the driving crystal, the other to the load, that is to the interferometer path, as represented in our formulas by the quantity  $z_m$ . It is possible, indeed, to split the expression for  $Z_1$  into the sum of two such parts. It can be verified easily that  $Z_1$ , according to eqs. (1.24) and (1.46), can be written as follows:

a) Bar :

$$Z_1 = \frac{q^E t}{\omega A H^2} \frac{1}{j} \cot \frac{\varphi}{2} + \frac{q^E t}{\omega A H^2} \frac{\varphi/2}{2 z_m - j \cot \frac{\varphi}{2}}, \quad (3.18)$$

b) Plate :

$$Z_1 = \frac{q^D l}{\omega A H^2} \frac{1}{j} \left( \cot \frac{\varphi}{2} - \frac{H^2}{\epsilon^S q^D} \right) + \frac{q^D l}{\omega A H^2} \frac{\varphi/2}{2 z_m - j \cot \frac{\varphi}{2}}. \quad (3.19)$$

The first terms in eqs. (3.18) and (3.19) correspond exactly to the expressions for  $Z_1$  found for the free bar in eq. (2.1) and for the free plate in eq. (2.11). The second terms may be construed as representing that part of the total electric impedance  $Z_1$  which is linked with the interferometer path.

Writing  $Z_1$  as the sum of the input impedance of the free crystal  $Z_{1c}$  and the impedance of the interferometer path  $Z_{1i}$ , that is  $Z_1 = Z_{1c} + Z_{1i}$ , and introducing  $\varphi = \gamma_c l$  we find

$$Z_{1i} = z_0 \frac{1}{2 \frac{1}{z_m} - j \cot \frac{\varphi}{2}}, \quad (3.20)$$

where

$$(z_0)_{\text{bar}} = \frac{\varphi q^E t}{2 \omega A H^2} = \sqrt{q^E \varrho_c} \frac{l t}{2 A H^2} \quad (3.21)$$

and

$$(z_0)_{\text{plate}} = \frac{\varphi q^D l}{2 \omega A H^2} = \sqrt{q^D \varrho_c} \frac{l^2}{2 A H^2}. \quad (3.22)$$

The equivalent circuit of Fig. 3 for the loaded crystal can be replaced by that shown in Fig. 8;  $Z_{1c}$  is the impedance of the free crystal, which may be represented in the neighbourhood of resonance by the  $RLC$ -branch in Fig. 6, with the values of  $R$ ,  $L$  and  $C$  as given in Part II.

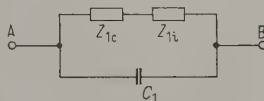


Fig. 8. Equivalent electric circuit for the loaded piezoelectric crystal.  $Z_{1c}$  impedance of the free crystal,  $Z_{1i}$  impedance of the interferometer path.

Our main interest lies in the impedance  $Z_{1i}$ , as represented by eq. (3.20). This impedance is given by the same expression for the bar as for the plate, but  $z_0$  might have different values in the two cases. Inserting  $z_m$  from eq. (3.15), we obtain

$$Z_{1i} = z_0 \frac{1}{2 \frac{1+r}{m} - j \cot \frac{\varphi}{2}}. \quad (3.23)$$

## 3. Circle diagram for the electric impedance $Z_{1i}$ of the interferometer path

The usual purpose of the acoustic interferometer is the determination of the velocity  $c_m$  of sound and the absorption coefficient  $\alpha_m$  of the medium filling the interferometer path. This is accomplished by changing the distance  $d$  or the acoustic wavelength  $\lambda_m$  in the medium and observing, for example, the corresponding changes of the current  $I$  to the crystal (Fig. 1) at constant voltage  $V$ . All changes of parameters of the matching electric circuit connected



with the crystal are associated with the changes of the electric input impedance  $Z_1 = Z_{1c} + Z_{1i}$  of the loaded crystal (Fig. 8). The behavior of  $Z_{1c}$  belonging to the free crystal has been treated in Part II. In all cases except when the frequency is varied,  $Z_{1c}$  is constant, because it is independent of the variables of the interferometer path. Our main interest lies in the variation of  $Z_{1i}$ , associated with the interferometer path.

Eq. (3.23) gives  $Z_{1i}$  as a function of  $r$  and  $\varphi = \gamma_c l$ . First we note that, according to eq. (3.5),  $\gamma_m$  can be written for any medium as

$$\gamma_m = \frac{\omega}{c_m} - j\alpha_m. \quad (3.24)$$

Then, according to eqs. (3.11) and (3.8),

$$r = I e^{-2j\omega d/c_m} e^{-2\alpha_m d} \quad (3.25)$$

or

$$r = |I| e^{j(\theta - 4\pi d/\lambda_m)} \cdot e^{-2\alpha_m d} = R e^{-j\varphi}, \quad (3.26)$$

where

$$R = |I| \cdot e^{-2\alpha_m d}$$

$$\text{and} \quad \varphi = \frac{4\pi d}{\lambda_m} - \theta = \frac{2\omega d}{c_m} - \theta. \quad (3.27)$$

The variation of  $r$  is effected either by a) changing the pathlength  $d$  at constant acoustic wavelength  $\lambda_m$  (variable path interferometer), or by b) changing  $\lambda_m$  at constant  $d$  (fixed path interferometer). The reflection coefficient  $|I| e^{j\theta}$  is treated here as a constant, independent of the frequency.

Case a):

The variation of  $d$  usually is of the order of magnitude of a few half-wavelengths  $\lambda_m/2$ . Each change in  $d$  by  $\lambda_m/2$  changes the term  $\exp(j \cdot 4\pi d/\lambda_m)$  in eq. (3.26) by  $2\pi$  and causes a periodic change in  $r$  by a full period. The term  $\exp(-2\alpha_m d)$  in eq. (3.26) decreases continuously with increasing  $d$ . If  $\alpha_m$  is not unusually large, this term can be regarded as "slowly" varying in comparison with the "rapidly" varying preceding factor in eq. (3.26).

Case b):

The term  $\exp(-2\alpha_m d)$  in eq. (3.26) is constant; the periodic changes in  $r$  are effected only by an alteration of the number of half-wavelengths within the interferometer path, either by a change in the sound velocity  $c_m$  (due to changes in pressure, temperature or composition of the medium) or by a change of the driving frequency  $f$ .

The first step in the graphical representation is to consider the locus of  $r$ . In the complex  $r$ -plane  $r = R e^{-j\varphi}$  describes exactly a circle with centre at the origin, when  $\lambda_m$  is changed steadily (Fig. 9a). A change of  $d$ , however, causes  $r$  to describe a spiral, due to the factor  $\exp(-2\alpha_m d)$  in eq.

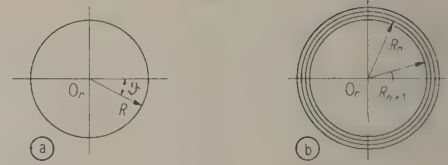


Fig. 9. Locus in the  $r$ -plane of the quantity  $r = R e^{-j\varphi}$  in eq. (3.26) with variation of (a) the acoustic wavelength  $\lambda_m$  and (b) the path length  $d$ . In (b) the ratio between two successive radii is given by  $R_{n+1} = R_n e^{-\alpha_m \lambda_m}$ .

(3.26). In what follows we assume  $\alpha_m$  to be a relatively small quantity; we may then replace the continuous spiral by a sequence of circles whose diameters decrease by a factor  $\exp(-\alpha_m \lambda)$  each time when  $r$  has undergone a change of one full period (Fig. 9b). Only for media with unusually large absorption will the spiral contract so quickly that this approximation has to be replaced by a more exact treatment. This can be done by using the general expressions of eqs. (3.23) and (3.26).

We next find the locus of  $Z_{1i}$  in eq. (3.23) when  $r$  describes a circle around the origin, as indicated in Fig. 9.  $Z_{1i}$  in eq. (3.23) can be written in the following form:

$$\frac{Z_{1i}}{z_0} = \frac{m}{(1+p)^2} \frac{1}{r + \frac{1-p}{1+p}} - \frac{m/2}{1+p}, \quad (3.28)$$

$$\text{where} \quad p = j \frac{m}{2} \cot \frac{\varphi}{2}. \quad (3.28a)$$

The term  $\varphi/2$  will be regarded as a constant, as is the case when the driving frequency is kept constant. Even if the interferometer is used at varying frequency,  $d/\lambda_m$  is usually a large number and  $\cot \varphi/2$  is a very slowly changing function near crystal resonance ( $\varphi \approx \pi$ ) in comparison with the rapid change of  $r$  so that, as a first approximation,  $\cot \varphi/2$  can be regarded as constant in eq. (3.28) (see also Part V). The kind of function connecting the variables  $Z_{1i}$  and  $r$  in eq. (3.28) is called a homographic or linear substitution. It is known that a circle in the  $r$ -plane is always transformed into a circle (or a straight line in special cases) in the  $Z_{1i}$ -plane (see, for example, [8], p. 605, Sec. 258)<sup>9</sup>.

To obtain the circle in the  $Z_{1i}$ -plane corresponding to the  $r$ -circles as indicated in Fig. 9, the following steps are to be performed in conformity with eq. (3.28) [8]:

<sup>9</sup> Circle diagrams in connection with the determination of sound absorption have been introduced also by C. W. KOSTEN [14].

1. Transformation of the origin  $O_r$  in the  $r$ -plane to a point  $P = -(1-p)/(1+p)$ .
2. Rotation of the plane through  $180^\circ$  around a line through  $P$  whose angle with the real axis is given by one-half of the angular coordinate of  $m/(1+p)^2$ .
3. Inversion with respect to  $P$  of the  $r$ -circle in its displaced position with a constant of inversion equal to  $|m/(1+p)^2|$ .
4. Displacement of the original origin  $O_r$  to the point  $O = (m/2)/(1+p)$ , which is the origin for the  $Z_{1i}/z_0$ -circle.

As these steps include only displacements of origins and an inversion, it is obvious that every  $r$ -circle is transformed into a circle (or straight line) in the  $Z_{1i}$ -plane. The position of the centre  $C$  as well as the radius  $\varrho$  of the corresponding  $Z_{1i}$ -circle can be calculated by the exact expression eq. (3.28). This calculation will be given in the following section under the simplifying assumption that  $\cot \varphi/2$  is constant and real; this assumption is justified under the usual experimental conditions. Fig. 10 shows schematically the positions of the  $r$ -circle and the  $Z_{1i}$ -circle. Since the real part of  $Z_{1i}$  is always to be positive, the  $Z_{1i}$ -circle must be situated at the right side of the imaginary axis of the  $Z_{1i}$ -plane. It is easy to see that the inner part of the  $r$ -circle is transformed into the inner part of the  $Z_{1i}$ -circle.

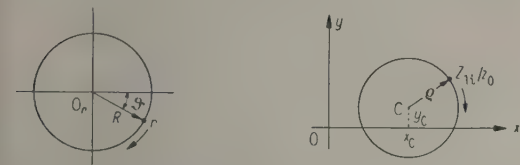


Fig. 10. Corresponding circular loci in the  $r$ -plane (left) for  $r = R e^{-j\varphi}$  and in the  $Z_{1i}$ -plane (right) for  $Z_{1i}/z_0 = x + jy$ . The circles are described by  $r$  and  $Z_{1i}/z_0$  as indicated by the sense of the arrows with increasing  $\varphi$ , that is with increasing frequency.

The greatest radius  $R$  occurring in the  $r$ -plane corresponds to the value  $d=0$ , as seen from eq. (3.27).  $R$  equals  $|T|$  in this case;  $R_{\max}=1$  for a perfect reflector. Owing to the absorption in the medium,  $R$  decreases steadily when  $d$  increases. If  $d$  tends toward infinity,  $R$  tends toward zero;  $d=\infty$  corresponds to a crystal radiating into an infinitely extended medium, where no reflected wave exists ( $r=0$ ). The corresponding value of  $Z_{1i}$  follows from eq. (3.23):

$$(Z_{1i})_{r=0} = \frac{z_0}{\frac{2}{m} - j \cot \frac{\varphi}{2}}. \quad (3.29)$$

This value of  $Z_{1i}$  represents the electric impedance equivalent to the radiation-load of a crystal radiat-

ing from one face into an infinitely extended medium. The sequence of  $r$ -circles with decreasing radii  $R$  is represented in the  $Z_{1i}$ -plane by a sequence of circles with decreasing radii  $\varrho$ . But whereas the centre  $O_r$  in the  $r$ -plane remains fixed, the centre  $C$  in the  $Z_{1i}$ -plane moves towards the point  $C_0$  given by eq. (3.29), since the coordinates  $(x_C, y_C)$  of  $C$  are functions of  $R$ . Fig. 11 gives a qualitative picture of the correspondence between circles in the two planes. Actually, as we saw above, a change in  $d$  causes  $r$  to describe a spiral around  $O_r$ , whose radius decreases slowly if the absorption in the medium is not extremely large. The corresponding locus of  $Z_{1i}$  is also strictly a kind of spiral whose "centre" is slowly moving as indicated by the sequence  $C_3 - C_2 - C_1 - C_0$  in Fig. 11.

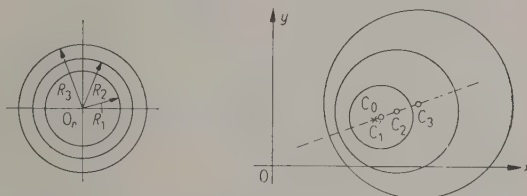


Fig. 11. Location of corresponding circles in the  $r$ -plane (left) and the  $Z_{1i}/z_0$ -plane (right).  $C_0$  denotes the centre with zero radius.

In practical interferometry, using a variable path-length  $d$ , only a few consecutive cycles in the  $r$ -plane are described, whose radii change slowly under ordinary conditions. Thus  $Z_{1i}$  describes the same number of cycles in the  $Z_{1i}$ -plane with slowly decreasing radii and a small displacement of  $C$ , when  $\alpha_m$  is not extremely large. A full cycle in the  $r$ -plane is performed when the change in  $(4\pi d/\lambda_m)$  equals  $2\pi$  (eq. (3.26)), or when

$$\Delta(2d/\lambda_m) = 1. \quad (3.30)$$

At constant  $T$  the initial radius  $R = |T| e^{-2\alpha_m d}$  changes into  $R' = |T| e^{-2\alpha_m(d+\Delta d)}$  in each cycle, or, using (3.30) at constant  $\lambda_m$ ,

$$R'/R = e^{-2\alpha_m \Delta d} = e^{-\alpha_m \lambda_m}. \quad (3.31)$$

If  $\alpha_m \lambda_m \ll 1$ ,  $R' \approx R$  or  $Z_{1i}' \approx Z_{1i}$  according to eq. (3.23). In other words, when we start at a certain distance  $d$  corresponding to a certain value of  $Z_{1i}$  and change  $d$  into  $d + \lambda_m/2$ , we obtain very approximately the same value of  $Z_{1i}$ , if  $\alpha_m \lambda_m$  can be assumed to be small. Or, a change of  $d$  by  $\lambda_m/2$  causes  $Z_{1i}$  to describe very approximately a complete cycle in the  $Z_{1i}$ -plane. This is not the case, however, if the product  $\alpha_m \lambda_m$  is relatively large.

In the case of the fixed-path interferometer, where  $\lambda_m$  is varied at constant  $d$ , the term  $e^{-2\alpha_m d}$  in eq. (3.27) remains unaltered. Here we



have to deal with only one circle of constant radius in the  $r$ -plane, corresponding to one circle with constant radius in the  $Z_{1i}$ -plane. A change in  $\lambda_m$  corresponding to eq. (3.30) causes  $Z_{1i}$  to describe exactly one full cycle, provided the term  $\cot \varphi/2$  can be regarded as constant in eq. (3.23). This means that an increase by one of the number of half-wavelengths filling the path-length  $d$  leads to exactly the same value of  $Z_{1i}$ .

#### 4. Radius and coordinates of the centre of the $Z_{1i}$ -circle

In the preceding section we dealt qualitatively with the conformal representation of the  $r$ -circle and the corresponding  $Z_{1i}$ -circle. Now we establish the analytical expressions for the coordinates  $x_C, y_C$  of the centre  $C$  and for the radius  $\varrho$  of the  $Z_{1i}$ -circle, which corresponds to an  $r$ -circle with radius  $R$  and centre  $O_r$  in the  $r$ -plane. In eq. (3.23) we put  $Z_{1i}/z_0 = w = x + jy$ ;  $r = R e^{-j\vartheta}$ ;  $\cot \varphi/2 = b$  (assuming  $b$  to be a real constant);  $m = m_0 + j m_1$ , and obtain

$$x + jy - \quad (3.32)$$

$$= \frac{(m_0 + j m_1) (1 - R e^{-j\vartheta})}{2(1 + R e^{-j\vartheta}) - (j m_0 - m_1) b (1 - R e^{-j\vartheta})} = 0.$$

Setting the real and imaginary parts of the left side of eq. (3.32) separately equal to zero and eliminating  $\cos \vartheta$  and  $\sin \vartheta$  from these two equations, for example, by squaring and adding them, we obtain the equation for the locus of  $w = Z_{1i}/z_0$  which corresponds to an  $r$ -circle with radius  $R$  and the origin as centre. The result is

$$\{x - [2 m_0 (1 + R^2)]/D^2\}^2 + \{y - [2 m_1 (1 + R^2) + |m|^2 b (1 - R^2)]/D^2\}^2 = \frac{4 m_0^2 (1 + R^2)^2 + [2 m_1 (1 + R^2) + |m|^2 b (1 - R^2)]^2}{D^4} - \frac{|m|^2 (1 - R^2)}{D^2}, \quad (3.33)$$

where

$$D^2 = 4(1 - R^2) + 4 m_1 b (1 + R^2) + m^2 b^2 (1 - R^2).$$

In most practical cases the quantities  $\cot \varphi/2 = b$  and  $m_1/m_0$  can be regarded as small (see also Part IV). Ignoring all terms of order  $b^2$ ,  $m_1 b$ , and higher, we find the following expressions for the coordinates  $x_C, y_C$  of the centre  $C$  and for the radius  $\varrho$  of the quantity  $w = Z_{1i}/z_0$ :

$$x_C = \frac{m_0}{2} \frac{1 + R^2}{1 - R^2},$$

$$y_C = \frac{m_1}{2} \frac{1 + R^2}{1 - R^2} + \frac{|m|^2}{4} \cot \frac{\varphi}{2}, \quad (3.34)$$

$$\varrho = \frac{|m| R}{1 - R^2},$$

( $\cot \varphi/2 \ll 1$  and real;  $m_1 \ll m_0$ ).

When  $\cot \varphi/2 = b = 0$ , these formulas are valid for any value of  $m_1/m_0$ , as is seen by eq. (3.33).

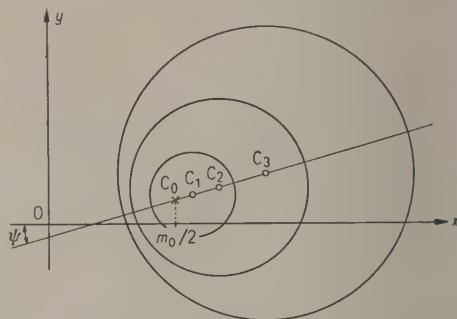


Fig. 12. Location of circles in the plane of  $w = x + jy = Z_{1i}/z_0$  corresponding to concentric circles in the  $r$ -plane with different values of radius  $R$ .

Eq. (3.34) gives immediately

$$y_C = \frac{m_1}{m_0} x_C + \frac{|m|^2}{4} \cot \frac{\varphi}{2} \quad (3.35)$$

and

$$\varrho^2 = \frac{|m|^2}{m_0^2} x_C - \frac{|m|^2}{4} \quad (3.36)$$

Thus the centres of the circles for different values of  $R$  are located on a straight line, whose angle  $\psi$

with the  $x$ -axis is given by  $\tan \psi = m_1/m_0$ . The radius  $\varrho$  increases with increasing  $x_C$  towards  $\varrho = \infty$  at  $x_C = \infty$  or  $R = 1$ . The smallest possible value for  $x_C$  is given by  $x_C = m_0/2$  with  $\varrho = 0$  or  $R = 0$ .

Fig. 12 shows the positions of different circles for different values of  $R$ ; it confirms the more qualitative picture in Fig. 11.

PART IV  
GENERAL PROPERTIES OF THE ELECTRIC INPUT IMPEDANCE  
OF THE ACOUSTIC INTERFEROMETER  
UNDER VARIOUS EXPERIMENTAL CONDITIONS

1. Quantitative considerations

Following the more qualitative considerations of Part III we now give attention to the values of the more important parameters in the main equation (3.23), as encountered under practical conditions.

a) The quantity  $m = m_0 + j m_1$ :

The imaginary part  $m_1$  is very small in comparison with  $m_0$  under ordinary conditions. Neglecting losses in the crystal in eq. (3.17 a), that is assuming  $\alpha_c c_c \ll \alpha_m c_m$ , and introducing  $c_m = \omega_0 \lambda_m / 2 \pi$ , we obtain from eq. (3.17):

$$\frac{m_1}{m_0} = \frac{\alpha_m \lambda_m}{2 \pi} \quad (4.1)$$

The order of magnitude of  $\alpha_m / f_0^2$  (in  $\text{cm}^{-1} \text{s}^2$ ) is known to be  $10^{-13}$  in gases and  $10^{-16}$  in liquids<sup>10</sup>.

The velocity of sound may be assumed to have the order of magnitude of  $c_m = 3 \cdot 10^4 \text{ cm/s}$  in gases and  $c_m = 10^5 \text{ cm/s}$  in liquids. The quantity  $\alpha_m \lambda_m$  may be assumed therefore to be in the order of magnitude of

$$\alpha_m \lambda_m = \frac{\alpha_m c_m}{f_0} \approx \begin{cases} 3 \cdot 10^{-9} \cdot f_0 & \text{in gases,} \\ 10^{-11} \cdot f_0 & \text{in liquids.} \end{cases} \quad (4.2)$$

Even up to the megacycle range the quantity  $\alpha_m \lambda_m$  can be regarded as small in comparison with unity (especially in liquids). Still one must be careful in special cases, where the assumptions made above may not be justified; for some substances  $\alpha_m$  and/or  $c_m$  may be of larger order of magnitude; then  $f_0$  must be smaller to justify the assumption that  $\alpha_m \lambda_m \ll 1$ .

Therefore, according to eq. (4.1),  $m_1$  can be neglected ordinarily in comparison with  $m_0$  and  $m$  may be regarded as a real quantity  $|m| \approx m_0$ .

b) The quantity  $r = R e^{-j\phi}$ :

The foregoing considerations, which resulted in the estimates for  $\alpha_m \lambda_m$  according to eq. (4.2), justify also the assumption mentioned already in Part III concerning  $R$ , namely that  $R$ , according to eq. (3.27), is a slowly varying function, when  $d$  is steadily changed by an amount of a few half-wavelengths. Thus the spiral in the  $Z_{11}$ -plane mentioned in Part III, Section 3, due to a variation of the path-length, contracts very slowly with the change of  $d$  and may reasonably be replaced by a sequence of circles, as outlined.

<sup>10</sup> See [3], for example pp. 464 and 538.

c) The quantity  $\cot \varphi / 2$ :

According to eq. (1.11)  $\varphi = \gamma_c l = 2 \pi (l / \lambda_c) - j \alpha_c l$ ; the crystal is usually driven at or near its fundamental mode, that is  $l \approx \lambda_c / 2$  and  $\varphi / 2 \approx (\pi / 2) - j \alpha_c \lambda_c / 2$ . The attenuation in crystals is known to be extremely small, so that we may regard  $\varphi / 2$  as a real quantity, neglecting the term  $j \alpha_c \lambda_c / 2$ .

In the neighbourhood of  $\varphi / 2 = \pi / 2$  the cotangent function can be replaced by  $(\pi / 2) \Delta \lambda / \lambda_0$ , where  $\Delta \lambda$  is defined by  $\lambda = \lambda_0 + \Delta \lambda = 2 l + \Delta \lambda$  in a piezoelectric plate. Usually  $\lambda$  equals  $2 l$  very approximately and the cotangent term in the denominator of eq. (3.23) is a small quantity which can be neglected in comparison with the other term. The order of magnitude of  $m \approx m_0$  is  $10^{-5}$  for gases and  $10^{-1}$  for liquids. Thus in gases the weight of the cotangent term is considerably smaller when compared with the weight of the first term, which contains the factor  $1 / m$ , than it is in liquids. The cotangent term may become important when  $r$  in eq. (3.23) comes very close to  $-1$ , that is when  $R = |I| e^{-2 \alpha_m d}$  is close to unity.

It is therefore advisable to choose the driving frequency so that  $\cot \varphi / 2$  equals zero, that is at resonance for the free bar and antiresonance for the free plate (see Part II). If the interferometer is used at variable frequency, it will depend upon the experimental conditions ( $|I|$  and  $\alpha_m \cdot d$ ), whether the cotangent term in the denominator of eq. (3.23) has to be taken into consideration or not.

2. Connection between  $Z_{11}$  and the formulas of Hubbard for the acoustic interferometer

J. C. HUBBARD [12] was the first to develop a theory for the acoustic interferometer. Upon his theory are based all subsequent investigations with this device. The difference between his theory and that given here is that HUBBARD's method, although leading by an ingenious procedure quite quickly to his well-known results, nevertheless makes it difficult to perceive the significance of the various assumptions involved. On the other hand, the theory offered here starts from the basic piezoelectric equations of state and leads in a rigorous and straightforward way to more general results.

HUBBARD showed that the reaction of the interferometer load upon the electric input impedance of the driving crystal can be expressed by an impedance, which for convenience we call



$$Z_H = \text{const}(P - jQ),$$

in series with the impedance of the free crystal. This is, as it should be, quite in agreement with the foregoing considerations, which led to the equivalent circuit of Fig. 8. The impedance  $Z_{11}$  in our notation must consequently be identical with HUBBARD's  $Z_H$ , if the assumptions implicitly involved in his calculations are introduced in our eq. (3.23). These assumptions turn out to be the following:

1.  $\cot \varphi/2 = 0$ : The crystal is driven exactly at its resonant frequency in the case of a bar (cf. eq. (2.4)) or at antiresonant frequency in the case of a plate (cf. eq. (2.18)). The losses in the crystal are negligible.
2.  $m = m_0$ ;  $m_1 = 0$ : The losses in the medium are not unusually large, so that  $m_1$  can be neglected in comparison with  $m_0$  (cf. Part IV, Section 1 a).
3.  $\Theta = \pi$ : The phase-jump of the reflected wave in the interferometer path equals  $180^\circ$  exactly (eqs. (3.8) and (3.27)).

Introducing these assumptions in the general expression (3.23), we obtain

$$Z_{11} = \frac{m_0 z_0}{2} \frac{1 - R e^{-j\vartheta}}{1 + R e^{-j\vartheta}}. \quad (4.3)$$

After separating the right side into real and imaginary parts, we find

$$Z_{11} = \frac{m_0 z_0}{2} \left( \frac{1 - R^2}{1 + R^2 + 2R \cos \vartheta} + j \frac{2R \sin \vartheta}{1 + R^2 + 2R \cos \vartheta} \right). \quad (4.4)$$

Comparing this expression with HUBBARD's impedance

$$Z_H = \text{const}(P - jQ) \quad (4.5)$$

and introducing

$\vartheta = (2\omega d/c_m) - \pi$  and  $R = | \Gamma | e^{-2\alpha_m d}$  according to eq. (3.27) with  $\Theta = \pi$ , we get

$$P = \frac{1 - | \Gamma |^2 e^{-4\alpha_m d}}{1 + | \Gamma |^2 e^{-4\alpha_m d} - 2 | \Gamma | e^{-2\alpha_m d} \cos \frac{2\omega d}{c_m}} \quad (4.6)$$

$$Q = \frac{2 | \Gamma | e^{-2\alpha_m d} \sin \frac{2\omega d}{c_m}}{1 + | \Gamma |^2 e^{-4\alpha_m d} - 2 | \Gamma | e^{-2\alpha_m d} \cos \frac{2\omega d}{c_m}}$$

in conformity with HUBBARD's expressions  $P_{x=0}$  and  $Q_{x=0}$  (in his notation), as given, for example, by F. E. Fox ([9], formulas (6) and (7)). The constant in eq. (4.5) is found by using eqs. (3.17), (3.21) and (3.22), and introducing  $\gamma = \varphi/l = \pi/2l = \omega \sqrt{\rho_c/q_c} = \pi c \sqrt{\rho_c/q_c}/l$ :

$$\text{const} = \frac{m_0 z_0}{2} = \begin{cases} \frac{\rho_m \epsilon_m l t}{2 A H^2} & \text{for the bar,} \\ \frac{\rho_m c_m l^2}{2 A H^2} & \text{for the plate.} \end{cases} \quad (4.7)$$

We may repeat that HUBBARD's formulas do not include the cases where a) the frequency differs from  $c_c/2l$ , b) the reflector induces a phase jump of the reflected wave different from  $\pi$ , and c) the absorption coefficient  $\alpha_m$  is unusually large. Eq. (3.23) is rigorous, covering all possible cases. Still, under ordinary experimental conditions, one would find no appreciable numerical difference between the two formulas.

### 3. Maxima and minima of the impedance $Z_{11}$ of the interferometer path and their relations to $\alpha_m$ , $| \Gamma |$ , and $\Theta$

Assuming ordinary experimental conditions we shall describe some characteristic features of the periodic changes of the impedance  $Z_{11}$ , as given in eq. (3.23), due to changes of the path length  $d$  or the acoustic wavelength  $\lambda_m$ .

By ordinary experimental conditions, the following is meant:

1.  $f_0 = \text{const.}$
2.  $\varphi/2 = \pi/2$ ;  $\cot \varphi/2 = 0$ . The losses in the crystal are negligible, so that  $\varphi$  is real. The corresponding frequency  $f_0$  is given by  $f_0 = c_c/2l$ ; thus  $\varphi/2 = \pi l/\lambda = \pi/2$  and the cotangent term in eq. (3.23) vanishes. This means that the crystal is driven at its resonant frequency in the case of a bar, or at its antiresonant frequency in the case of a plate (see Part II, eqs. (2.4) and (2.18)).
3. The coefficient of absorption  $\alpha_m$  in the medium is not unusually large, so that the quantity  $\alpha_m \lambda_m$  is small in comparison with unity (see eq. (4.2)). Then the locus of  $Z_{11}$ , due to a change in  $d$  of amount  $\lambda_m/2$ , may be regarded as practically a circle. When  $d$  remains fixed and  $\lambda_m$  is changed, the locus of  $Z_{11}$  is an exact circle, regardless of the value of  $\alpha_m \lambda_m$ .

If the assumptions mentioned under 1. 2. and 3. are valid,  $Z_{11}$  describes a circle as  $d$  or  $\lambda_m$  is varied. The radius  $\varrho$  and the coordinates  $x_C, y_C$  of the centre C of the circle described by the dimensionless quantity  $w = Z_{11}/z_0$  has been given in eq. (3.34).

For experimental reasons it may be desirable to know also the locus of the admittance  $Y_{11} = 1/Z_{11}$ . The corresponding radius  $\bar{\varrho}$  and coordinates  $\bar{x}_C, \bar{y}_C$  of the centre C of the circle described by the dimensionless quantity  $\bar{w} = z_0 Y_{11}$  are easily found by inverting the  $w$ -circle as illustrated in Fig. 13. The inversion is effected by  $w = 1/\bar{w}$  or in coordi-

nates, according to the notation in Fig. 13, by

$$x = \frac{x}{x^2 + y^2}, \quad y = \frac{y}{x^2 + y^2}, \quad (4.8)$$

where  $x + jy = w$ , and  $\bar{x} + j\bar{y} = \bar{w}$ . A circle  $(x - x_c)^2 + (y - y_c)^2 = \varrho^2$  in the  $w$ -plane corresponds to the circle  $(\bar{x} - \bar{x}_c)^2 + (\bar{y} - \bar{y}_c)^2 = \bar{\varrho}^2$  in the  $\bar{w}$ -plane; the values of  $\bar{x}_c, \bar{y}_c$  and  $\bar{\varrho}$  of the inverted circle are found by means of eq. (3.34) with  $\cot \varphi/2 = 0$ :

$$\begin{aligned} \bar{x}_c &= \frac{2m_0}{|m|^2} \frac{1+R^2}{1-R^2}, & \bar{y}_c &= \frac{2m_1}{|m|^2} \frac{1+R^2}{1-R^2}, \\ \bar{\varrho} &= \frac{4}{|m|} \frac{R}{1-R^2}; \quad (\cot \varphi/2 = 0) \end{aligned} \quad (4.9)$$



Fig. 13. Loci of the quantities  $w = Z_{1i}/z_0$  (left) and  $\bar{w} = z_0 Y_{1i}$  (right) corresponding to the impedance and admittance of the interferometer path. The sense of the arrows corresponds to an increase in frequency.

Fig. 13 shows that the maximal and minimal values of  $|w|$  and  $|\bar{w}|$ , occurring at the points A and B or  $\bar{B}$  and  $\bar{A}$ , are given at any  $m = m_0 + jm_1$ , by

$$\begin{aligned} |w|_{\max} &= \sqrt{x_c^2 + y_c^2} + \varrho, & |\bar{w}|_{\max} &= \sqrt{\bar{x}_c^2 + \bar{y}_c^2} + \bar{\varrho}, \\ |w|_{\min} &= \sqrt{x_c^2 + y_c^2} - \varrho, & |\bar{w}|_{\min} &= \sqrt{\bar{x}_c^2 + \bar{y}_c^2} - \bar{\varrho}. \end{aligned}$$

From eqs. (3.34) and (4.9) we obtain

$$\begin{aligned} |Z_{1i}|_{\max} &= \frac{z_0}{2} \frac{|m|}{1-R}, & |Y_{1i}|_{\max} &= \frac{2}{z_0 |m|} \frac{1+R}{1-R}, \\ |Z_{1i}|_{\min} &= \frac{z_0}{2} \frac{|m|}{1+R}, & |Y_{1i}|_{\min} &= \frac{2}{z_0 |m|} \frac{1-R}{1+R}. \end{aligned} \quad (4.10)$$

The following relations result:

$$\begin{aligned} |Z_{1i}|_{\max} \cdot |Z_{1i}|_{\min} &= \frac{z_0^2 |m|^2}{4}, \\ |Y_{1i}|_{\max} \cdot |Y_{1i}|_{\min} &= \frac{4}{z_0^2 |m|^2}; \end{aligned} \quad (4.11)$$

$$\frac{|Z_{1i}|_{\min}}{|Z_{1i}|_{\max}} = \left( \frac{1-R}{1+R} \right)^2, \quad \frac{|Y_{1i}|_{\min}}{|Y_{1i}|_{\max}} = \left( \frac{1-R}{1+R} \right)^2.$$

The products of the maximal and minimal values of  $|Z_{1i}|$  or  $|Y_{1i}|$  are independent of  $R$ , that is of  $|F|$  and  $\alpha_m d$ . On the other hand their ratio is independent of the properties of the crystal and

of  $m$ , but depends upon the absorption in the medium. From this ratio the quantity  $R$  can be determined, which involves the absorption of the medium ( $\alpha_m d$ ) as well as the losses ( $|F|$ ) at the reflector. Measurements at two different values of  $d$  allow one to separate the losses in the medium from those at the reflector, as is well known [10]. Eqs. (4.11) are obtained under the assumption that the change in  $R$  due to the factor  $e^{-2\alpha_m d}$  is small; therefore they should be applied to adjacent maxima and minima at each of the two path-lengths.

The coefficient of absorption  $\alpha_m$  and the coefficient of reflection  $|F|$  can be calculated as follows, if the ratio  $|Z_{1i}|_{\min}/|Z_{1i}|_{\max}$  or  $|Y_{1i}|_{\min}/|Y_{1i}|_{\max}$  is known for two different path lengths  $d_1$  and  $d_2$ :

Introducing

$$\sigma = \frac{1-R}{1+R} = \sqrt{\frac{|Z_{1i}|_{\min}}{|Z_{1i}|_{\max}}} = \sqrt{\frac{|Y_{1i}|_{\min}}{|Y_{1i}|_{\max}}} \quad (4.12)$$

$$\text{and} \quad X = 2\alpha_m d - \ln |F|, \quad (4.13)$$

we have, according to eq. (3.27),

$$R = |F| e^{-2\alpha_m d} = e^{-X}, \quad (4.14)$$

and from eq. (4.12)

$$\sigma = \frac{1-e^{-X}}{1+e^{-X}} = \tanh \frac{X}{2}, \quad \text{or} \quad X = \ln \frac{1+\sigma}{1-\sigma}. \quad (4.15)$$

Denoting by  $\sigma_1$  and  $\sigma_2$  the values of  $\sigma$  measured at the two distances  $d_1$  and  $d_2$ , we have the relations

$$\begin{aligned} X_1 &= 2\alpha_m d_1 - \ln |F| = \ln [(1+\sigma_1)/(1-\sigma_1)], \\ X_2 &= 2\alpha_m d_2 - \ln |F| = \ln [(1+\sigma_2)/(1-\sigma_2)], \end{aligned} \quad (4.16)$$

whence we find

$$\alpha_m = \frac{1}{2(d_2 - d_1)} \ln \frac{(1+\sigma_1)(1+\sigma_2)}{(1-\sigma_1)(1-\sigma_2)} \quad (4.17)$$

$$\text{and} \quad |F| = e^{\alpha_m (d_1 + d_2)} \sqrt{\frac{(1-\sigma_1)(1-\sigma_2)}{(1+\sigma_1)(1+\sigma_2)}}; \quad (4.18)$$

$$\text{also} \quad |F| = e^{2\alpha_m d_1} \frac{1-\sigma_{1,2}}{1+\sigma_{1,2}}. \quad (4.19)$$

When  $d$  can be made so large that  $2\alpha_m d \gg \ln |F|$ , the following simplified formula may be used, which is obtained from eq. (4.16), neglecting  $\ln |F|$ :

$$\alpha_m \approx \frac{1}{2d} \ln \frac{1+\sigma}{1-\sigma} \quad (2\alpha_m d \gg \ln |F|). \quad (4.20)$$

On the other hand if  $d$  can be made so small that  $e^{-2\alpha_m d} \approx 1$ ,  $|F|$  can be measured directly. Eq. (4.19) then becomes

$$|F| \approx \frac{1-\sigma}{1+\sigma} \quad (2\alpha_m d \ll 1). \quad (4.20a)$$

Returning to assumption 3. at the beginning of this section,  $m_1$  is very small in comparison with  $m_0$  under ordinary conditions. This means that  $y_c$  in



eq. (3.34) or (4.9) is very small in comparison with  $x_C$ . Thus the centres C and C' of the circles in the  $w$ - and  $\bar{w}$ -planes lie practically on the real axis; the maximal and minimal values of  $Z_{1i}$  or  $Y_{1i}$  are practically pure resistances and conductances. Under the condition that  $m_1$  is ignored in comparison with  $m_0$ , C and C' are located exactly on the real axis and the difference in  $\vartheta$  between the points A and B or B' and A' in Fig. 13 is exactly to  $\Delta\vartheta = \pi$ ; from eq. (3.27) it is seen that this corresponds to a variation  $\Delta d = \pi c_m / 2\omega = \lambda_m / 4$ . Indeed, according to eq. (4.4),  $Z_{1i}$  is real when  $\sin \vartheta = 0$  or  $\vartheta = \pm n\pi$ ; in this case  $|Z_{1i}|$  reaches its maximum ( $n=1, 3, 5, \dots$ ) or its minimum ( $n=0, 2, 4, \dots$ ). Therefore the difference in  $\vartheta$  in proceeding from a maximum to the next minimum or from a minimum to the next maximum in  $|Z_{1i}|$  (or  $|Y_{1i}|$  of course) is equal to  $\pi$ . Or, if  $m_1 \ll m_0$ , a change in path-length of  $\lambda_m / 4$  leads from the real maximum of  $|Z_{1i}|$  or  $|Y_{1i}|$  to the adjacent real minimum or vice versa. This is not so, however, if the absorption in the medium is unusually large; in this case the corresponding change in path-length differs from  $\lambda_m / 4$  and the maximal or minimal values of the moduli of  $Z_{1i}$  or  $Y_{1i}$  occur at complex values of  $Z_{1i}$  or  $Y_{1i}$ .

Since for  $m_1 \ll m_0$  the maxima or minima of  $|Z_{1i}|$  or  $|Y_{1i}|$  occur at  $\vartheta = \pm n\pi$ , we find from eq. (3.27) that the corresponding values of  $d = d_m$  are given by

$$\vartheta = \pm n\pi = \frac{2\omega d_m}{c_m} - \Theta$$

$$\text{or} \quad d_m = \left(n + \frac{\Theta}{\pi}\right) \frac{\lambda_m}{4} \quad (m_1 \ll m_0). \quad (4.21)$$

$n=1, 3, 5, \dots$  correspond to a maximum and  $n=0, 2, 4, \dots$  to a minimum of  $|Z_{1i}|$ . The phase jump  $\Theta$  of the reflected wave can be determined by means of eq. (4.21), when the distance  $d_m$  and the number of quarter-wavelengths filling the interferometer path are known. The difference in  $d_m$ , corresponding to a maximum and an adjacent minimum in  $|Z_{1i}|$  or  $|Y_{1i}|$ , is always  $\lambda_m / 4$ , whatever  $\Theta$  may be, if  $\Theta$  can be regarded as a constant.

Eq. (4.21) can be applied also to the fixed-path interferometer, where  $d$  is kept constant and the acoustic wavelength  $\lambda_m$  is changed.

With either type of interferometer, for a perfect reflector ( $\Theta = \pi$ ), eq. (4.21) states that a maximum of  $|Z_{1i}|$  occurs always when an even number of quarter-wavelengths, that is a whole number of half-wavelengths, fills the interferometer path; a minimum of  $|Z_{1i}|$  occurs at an odd number of quarter-wavelengths in the path. If the phase jump  $\Theta$  differs from  $\pi$ , the number of wavelengths filling the path at a maximal or minimal value of  $|Z_{1i}|$  is no longer a whole multiple of  $\lambda_m / 4$ .

The difference, however, in the number of quarter-wavelengths filling the interferometer path, and corresponding to a maximum and an adjacent minimum of  $|Z_{1i}|$  or  $|Y_{1i}|$ , is always unity, whatever the value of the constant  $\Theta$  (or  $|F|$  of course, which quantity does not enter eq. (4.22) at all) may be.

#### 4. Determination of the velocity of sound $c_m$ from the maxima and minima of the impedance $|Z_{1i}|$ <sup>11</sup>

As is well known, the velocity of sound  $c_m$  in the medium can be found from the distance between maxima and minima of  $|Z_{1i}|$  (or  $|Y_{1i}|$ ). Under the assumptions 2. and 3. of the preceding section,  $Z_{1i}/z_0$  describes a full circle in the  $w$ -plane (Fig. 13), when the change in  $\vartheta$  amounts to  $2\pi$  (see eqs. (3.26) and (4.3)). Thus the distance between two adjacent maxima or minima of  $|Z_{1i}|$  (or  $|Y_{1i}|$ ) corresponds to a change

$$\Delta \left( \frac{2\omega d}{c_m} \right) = \Delta \left( \frac{4\pi d}{\lambda_m} \right) = 2\pi \quad (4.22)$$

for constant  $\Theta$ , as seen from eq. (3.27).

If the variation of  $Z_{1i}$  (or  $Y_{1i}$ ) is caused by a change of path-length  $\Delta d$ , we obtain from eq. (4.22)

$$c_m = \frac{\omega}{\pi} \Delta d = 2f \Delta d \quad (m_1 \ll m_0), \quad (4.23)$$

where  $\Delta d$  is the change in path-length necessary to proceed from one maximum of  $|Z_{1i}|$  to the adjacent maximum or from one minimum of  $|Z_{1i}|$  to the adjacent minimum.

If the variation of  $Z_{1i}$  (or  $Y_{1i}$ ) is produced at constant frequency  $f_0$  by a small change  $\Delta\lambda_m$  in the acoustic wavelength  $\lambda_m$ , owing, for example, to a change of pressure, temperature or composition of the medium, the corresponding change  $\Delta c_m$  is found from eq. (4.22) to be

$$-\frac{\Delta c_m}{c_m} = \frac{\pi c_m}{\omega_0 d} = \frac{\lambda_{0m}}{2d}. \quad (4.24)$$

This is the relative change in  $c_m$  corresponding to a change in  $\lambda_m$  by an amount  $\Delta\lambda_m = \Delta c_m / f_0$  great enough to make  $|Z_{1i}|$  change from one maximum to the adjacent maximum, or from one minimum to the adjacent minimum.

If the variation of  $Z_{1i}$  (or  $Y_{1i}$ ) is produced by a change of the driving frequency  $f = \omega / 2\pi$ , the necessary change  $\Delta f$  to proceed from one maximum of  $|Z_{1i}|$  (or  $|Y_{1i}|$ ) to the next or from one minimum to the next is, according to eq. (4.22),

$$\Delta f = \Delta\omega / 2\pi = c_m / 2d,$$

whence the velocity  $c_m$  is

$$c_m = 2d \Delta f. \quad (4.25)$$

<sup>11</sup> See also [4].

A change of  $2\pi$  in  $\vartheta$  always corresponds to a full "period" of  $Z_{1i}$ , that is to a closed circle in the  $w$ -plane; it is obvious that the foregoing formulas (4.22) to (4.25) hold not only for adjacent maxima or minima of  $|Z_{1i}|$  but also for the more general case in which one proceeds from an arbitrary value of  $Z_{1i}$  (or  $Y_{1i}$ ) to exactly the same adjacent corresponding value.

Still, as pointed out in the preceding section, under ordinary conditions ( $m_1 \ll m_0$ ) the change in  $\vartheta$  necessary to proceed from a maximum of  $|Z_{1i}|$  to the adjacent minimum equals  $\pi$ , that is just half the amount found necessary to proceed from a maximum to the adjacent maximum in the general case. The foregoing formulas can therefore be modified for the case in which a maximum of  $|Z_{1i}|$  and an adjacent minimum are chosen for the determination of  $c_m$ . The formulas read in this case as follows:

$$c_m = 4 f \cdot \Delta d', \tag{4.23 a}$$

$$-\frac{\Delta c_m'}{c_m} = \frac{\lambda_0}{4 d}, \quad (m_1 \ll m_0) \tag{4.24 a}$$

$$c_m = 4 d \cdot \Delta f'. \tag{4.25 a}$$

5. On the form of the periodic curves for  $|Z_{1i}|$  or  $|Y_{1i}|$

Assuming again  $m_1 \ll m_0$ , that is circles in the  $w$ - and  $\bar{w}$ -planes (Fig. 14) with centres on the real axis, we now see what happens if  $\vartheta$  changes, for example, from  $\vartheta_B = 0$  at B (or B) to  $\vartheta_D = \pm \pi/2$ . This change in  $\vartheta$  corresponds to a change in  $d$  of  $\pm \lambda/8$ , as is seen from eq. (3.27). The corresponding values of  $w = Z_{1i}/z_0$  and  $\bar{w} = z_0 Y_{1i}$  are found from eq. (4.3):

$$w_D = \frac{m_0}{2} \frac{1 \pm j R}{1 \mp j R} \quad \text{and} \quad \bar{w}_D = \frac{2}{m_0} \frac{1 \pm j R}{1 \mp j R} \tag{4.26}$$

whence

$$w_D = \frac{m_0}{2} \left( \frac{1 - R^2}{1 + R^2} \pm j \frac{2 R}{1 + R^2} \right), \quad |w_D|^2 = \frac{m_0^2}{4}, \tag{4.27}$$

$$\bar{w}_D = \frac{2}{m_0} \left( \frac{1 - R^2}{1 + R^2} \pm j \frac{2 R}{1 + R^2} \right), \quad |\bar{w}_D|^2 = \frac{4}{m_0^2}. \tag{1.28}$$

By means of eqs. (3.34) and (4.9) the coordinates of  $w_D = x_D + jy_D$  and  $\bar{w}_D = x_{\bar{D}} + jy_{\bar{D}}$  can be written as

$$x_D = x_C - \frac{2 R}{1 + R^2} \varrho, \quad x_{\bar{D}} = x_C - \frac{2 R}{1 + R^2} \varrho, \tag{4.29}$$

$$y_D = \pm \frac{1 - R^2}{1 + R^2} \varrho, \quad y_{\bar{D}} = \pm \frac{1 - R^2}{1 + R^2} \varrho.$$

Fig. 14 shows the location of  $w_D$  and  $\bar{w}_D$ , denoted by D and  $\bar{D}$ , for different values of  $R$  (cf. the notation in Fig. 13). The circles vary from large

radii for  $R \approx 1$  to small radii for  $R \ll 1$ ; at  $R = 0$  the radii  $\varrho$  and  $\bar{\varrho}$  are zero (eqs. (3.34) and (4.9)) and the "centres" are at  $x_C = m_0/2$  and  $\bar{x}_C = 2/m_0$ . According to eqs. (4.27) and (4.28) the moduli  $|w_D| = m_0/2$ , and  $|\bar{w}_D| = 2/m_0$ , are independent of  $R$ . The circles with O and O as centres and radii  $m_0/2$  and  $2/m_0$  therefore intersect the  $w$ - and  $\bar{w}$ -circles for different values of  $R$  at the points D and D whose coordinates are given in eq. (4.29).

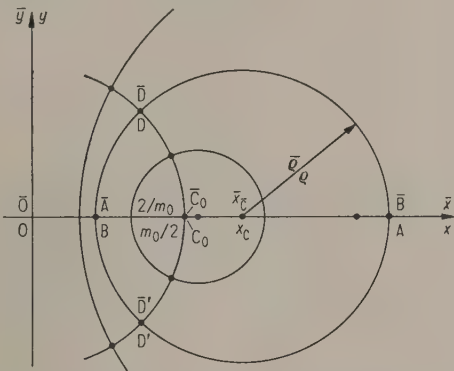


Fig. 14. Location of the points D (impedance) and  $\bar{D}$  (admittance) for  $\vartheta = 2n\pi + \pi/2$ , and of  $D'$  and  $\bar{D}'$  for  $\vartheta = 2n\pi - \pi/2$  in the  $w$ - or  $\bar{w}$ -plane. The points A or  $\bar{A}$  correspond to  $\vartheta = (2n+1)\pi$ , the points B or  $\bar{B}$  to  $\vartheta = 2n\pi$ .

Fig. 14 can be used to represent the  $w$ -plane as well as the  $\bar{w}$ -plane with the notation given in Fig. 13; only the scale-values have to be chosen properly. Incidentally, if  $m_0 = 2$  the scale values are the same for both planes, as seen from eqs. (4.27) and (4.28).

From Fig. 14 qualitative curves for  $(2/m_0 z_0) |Z_{1i}|$  or  $(m_0 z_0/2) |Y_{1i}|$  plotted against  $\vartheta$  can be found, as shown in Fig. 15. If  $R$  is close to unity, the  $w$ - or  $\bar{w}$ -circle is large, and D or  $\bar{D}$  (or, correspondingly,  $D'$ ) are much nearer to the minimum B or A than to the maximum A or B of  $(2/m_0 z_0) |Z_{1i}|$  or  $(m_0 z_0/2) |Y_{1i}|$ . At any  $R$  the quantity  $(2/m_0 z_0) |Z_{1i}|$  (and also  $(m_0 z_0/2) |Y_{1i}|$ ) has the same value at  $\vartheta = \pm \pi/2$ . Thus at  $R \approx 1$  the curves drop down rather rapidly from their maximal values to the value 1 at  $\vartheta = \pi/2$  and have comparatively flat minima.

When  $R \ll 1$  the circles in the  $w$ - or  $\bar{w}$ -plane are small and the points D or  $\bar{D}$  have nearly the same distance from B as from A (or from A as from B). Thus, as  $R$  decreases, maxima and minima assume more and more closely the same shape. At  $R = 0$ , corresponding to a reflector located at infinity or to a perfect absorber, the periodicity vanishes altogether, and a constant value of  $|Z_{1i}|$  or  $|Y_{1i}|$  is reached.



ed, namely the value for a crystal radiating into an infinite medium (eq. (3.29)).

It may be noted that the curves for  $(m_0 z_0/2) |Y_{1i}|$  are obtained by shifting the curves for  $(2/m_0 z_0) |Z_{1i}|$  to the right or to the left by an amount of  $\vartheta = \pi$  in Fig. 15, since

$$[(2/m_0 z_0) |Z_{1i}|]_{\vartheta+\pi} = [(m_0 z_0/2) |Y_{1i}|]_{\vartheta}$$

according to eq. (4.3).

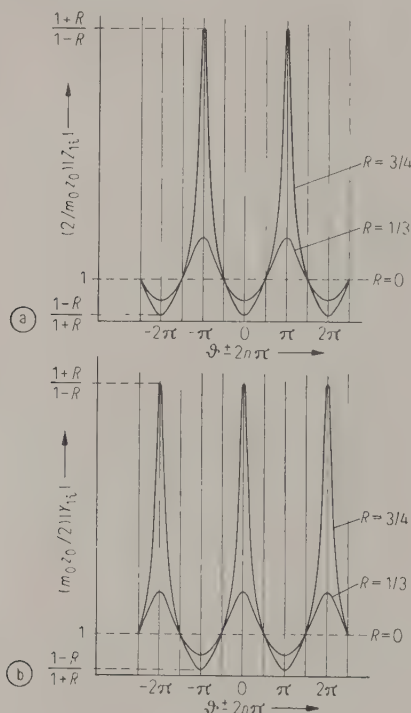


Fig. 15. Representation of (a)  $\frac{2}{m_0 z_0} |Z_{1i}|$  and (b)  $\frac{m_0 z_0}{2} |Y_{1i}|$  versus  $\vartheta \pm 2n\pi$  for different values of  $R$ .

The curves in Fig. 15 permit the following conclusions. At the same path-length  $d$  and the same reflection coefficient  $|r|$  the curves for  $|Z_{1i}|$  or  $|Y_{1i}|$  show sharp maxima and flat minima as long as the absorption  $\alpha_m$  is small. With large absorption this difference between maxima and minima tends to disappear. Or, for the same medium and the same reflector, the curves for  $|Z_{1i}|$  or  $|Y_{1i}|$  in the neighbourhood of two different distances  $d_1$  and  $d_2$  such that  $\alpha_m d_1 \ll 1$  and  $\alpha_m d_2 \gg 1$ , show a sharp maximum and a flat minimum at  $d_1$ , whereas at  $d_2$  this difference disappears. Different curves for  $|Z_{1i}|$  or  $|Y_{1i}|$  always intersect at whole multiples of  $\vartheta = \pm \pi/2$ ; the multiplicity can be found by the number of quarter-wavelengths along the path-length  $d$ .

We may add the following remark at this point: the total input-impedance  $Z_1$  of the interferometer is given by the sum  $Z_{1c} + Z_{1i}$ , as shown in Section 2 of Part III. In all cases where the crystal is driven at constant frequency, the constant term  $Z_{1c}$  has to be added to  $Z_{1i}$ . When  $\varphi/2 = \pi/2$ , as we have been assuming,  $Z_{1c}$  is the real "loss-resistance" due to losses in the crystal and mounting.  $Z_{1i}$  contains the factor  $m_0 z_0$  (eq. (4.3)), and is therefore proportional to  $m_0/f^2$ , as seen from eqs. (3.21) and (3.22). Since  $m_0$  is about 4000 times smaller in gases (at atmospheric pressure) than in liquids, at the same frequency the crystal is considerably more loaded by a liquid than by a gas.

Under ordinary circumstances, that is at frequencies not exceeding the order of magnitude of 1 Mc/s, a gaseous medium contributes essentially in the neighbourhood of  $|Z_{1i}|$  to the total impedance  $Z_1$ , whereas in the neighbourhood of  $|Z_{1i}|_{\min}$  the value of  $Z_{1c}$  is predominant. Fig. 16 illustrates this case. The distance OB, corresponding to  $|Z_{1i}|_{\min}$ , is only a small fraction of  $O_1O$ , corresponding to  $Z_{1c}$ .

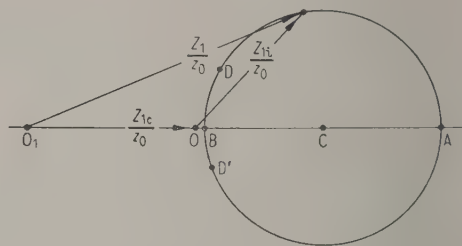


Fig. 16. Total input impedance  $Z_1 = Z_{1c} + Z_{1i}$  for a gaseous medium.

The minimum of  $Z_1$  is chiefly determined by  $Z_{1c}$ , and is therefore rather flat. The sharp maximum of  $Z_1$  is due to the sharp maximum of  $|Z_{1i}|$ , as shown in Fig. 15 a, occurring at  $\vartheta = \pi, 3\pi, 5\pi, \dots$  or  $d_m = n \lambda_m/2$  according to eq. (4.21).

In liquids, owing to the much greater value of  $m_0$ , the crystal is considerably loaded, up to very high frequencies, even when the impedance  $|Z_{1i}|$  has its minimal value, because the ratio  $|Z_{1i}|/Z_{1c}$  is so much larger than in gases. The position of  $O_1$  in Fig. 16 is then rather near to O. The behavior of  $|Z_1|$  is therefore approximately the same as that of  $|Z_{1i}|$  alone (Fig. 15) <sup>12</sup>.

<sup>12</sup> See also [9], (Fig. 2c). The characteristic difference in the shapes of the curves for current versus  $d$  in gases and in liquids, as experimentally observed and described in that paper (see also [3], Fig. 186, p. 245) is a consequence of the characteristic features of  $|Z_{1i}|$ , as described above and also mentioned by Fox. The particular curves for the current as given by Fox are essentially due to the particular circuit connected with his interferometer and to the frequencies applied.

6. Locus of minima and maxima of  $|Z_{1i}|$  and  $|Y_{1i}|$

If the path-length  $d$  is steadily increased, the minima of  $|Z_{1i}|$  or  $|Y_{1i}|$  rise and the maxima fall continuously, both finally tending towards the same value as  $d$  approaches infinity. Assuming the same conditions as mentioned in Section 3, and making use of eq. (4.10), we see that the locations of the minima and maxima of both  $|Z_{1i}|$  and  $|Y_{1i}|$  are associated with the function

$$f(d) = \frac{1-R}{1+R} = \frac{1-\exp(-2\alpha_m d + \ln|I|)}{1+\exp(-2\alpha_m d + \ln|I|)}$$
  
or 
$$f(d) = \tanh\left(\alpha_m d - \frac{1}{2} \ln|I|\right). \quad (4.30)$$

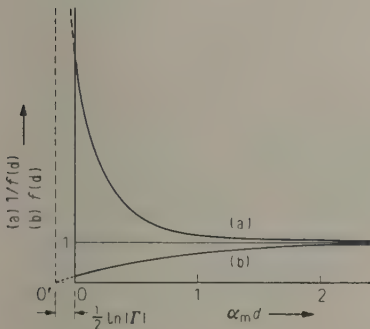


Fig. 17. Locus containing (a) the maxima and (b) the minima of  $\frac{2}{|m|z_0}|Z_{1i}|$  and  $\frac{|m|z_0}{2}|Y_{1i}|$  versus  $\alpha_m d$ .

Indeed,  $f(d)$  contains all the minima of  $|Z_{1i}| \cdot 2/(z_0|m|)$  or of  $|Y_{1i}| \cdot z_0|m|/2$ , whereas the maxima of these quantities are on the reciprocal curve  $1/f(d)$ , as seen from eq. (4.10).

Fig. 17 shows the curves for  $f(d)$  and  $1/f(d)$  according to eq. (4.30). The origin  $O$  is at a distance of  $(1/2) \ln|I|$  from the origin  $O'$  of the curve for  $f' = \tanh \alpha_m d$ . If  $|I|$  is close to unity and  $\alpha_m d$  small, we can set  $|I| = 1 - \varepsilon$ , where  $\varepsilon$  is a small quantity, and obtain from eq. (4.30) as a first approximation

$$f(d) \approx \alpha_m d + \frac{\varepsilon}{2} \quad (4.31)$$
  
 $(\alpha_m d \ll 1, \varepsilon \ll 1).$

It will be noted that the minima are located approximately on a straight line, which intersects the ordinate-axis at  $f(d) = \varepsilon/2 = (1/2)(1 - |I|)$ . The maxima lie on a hyperbola  $1/f(d)$ . This corresponds to remarks, found in the literature, that the "peak envelope" is rather a hyperbola than an exponential. The envelope is never a simple exponential, as seen from eq. (4.30).

It may be noted that our statements concerning maxima and minima are related to  $|Z_{1i}|$  or  $|Y_{1i}|$  and not to the total impedance  $|Z_1| = |Z_{1c} + Z_{1i}|$  which is necessarily the observed impedance. Whether or not  $|Z_{1c}|$  may be neglected depends on the actual ratio  $|Z_{1c}|$  to  $|Z_{1i}|$ . In many cases, especially at small values of  $m$  and when  $R$  comes close to unity, proper consideration must be given to  $|Z_{1c}|$ .

PART V  
THE VARIABLE-FREQUENCY INTERFEROMETER

For those cases in which movable parts should be avoided, the fixed path interferometer offers considerable experimental advantages [13]. The change of  $|Z_{1i}|$  at constant path-length can be effected by a variation of the acoustic wavelength  $\lambda_m$  in the medium, as seen from eq. (3.26). This variation might take place at constant frequency  $f_0$ , as, for example, when the pressure, the temperature, or the composition of the medium is varied. From this variation the corresponding change  $\Delta c_m$  of the velocity  $c_m$  can be found, as shown by eq. (4.24). Still, the absolute initial value of  $c_m$  must be known in order to plot the changes  $\Delta c_m$  against the variable parameter that causes  $\lambda_m$  to change.

A determination of  $c_m$  itself can be accomplished by varying the driving frequency at constant path-length. If one could observe the corresponding change in  $|Z_{1i}|$ ,  $c_m$  could easily be found by means of eqs. (4.25) or (4.25 a). Also the absorption-coefficient  $\alpha_m$  could be calculated by formula (4.17)

or (4.20). The difficulty here is that the quantity determined experimentally is  $|Z_1| = |Z_{1c} + Z_{1i}|$ , where now  $Z_{1c}$  also varies due to the change in frequency.

At constant  $d$  the locus of  $|Z_{1i}|$  is practically a circle, whose centre, under ordinary conditions ( $m_1 \ll m_0$ ), lies practically on the real axis. The reason why this locus is not strictly a circle is seen from eq. (3.23): by changing the frequency the term  $\cot \varphi/2$ , which is zero for the reference frequency  $f_0 = c_m/2l$ , deviates from zero. According to eq. (3.34) the centre  $C$  of the circle for  $Z_{1i}$  moves away from the  $x$ -axis, as the frequency, and consequently  $\varphi$ , changes. Still, under most practical conditions the "coupling" term  $\cot \varphi/2$  in the denominator of eq. (3.23) may be kept so close to zero that it can be neglected in comparison with the term  $2(1+r)/m(1-r)$  (see also Part IV, Section 1 c). Quantitatively we may say that the cotangent term may be ignored, if





they would be if the crystal impedance  $Z_{1c} = O_1'O$  did not change. If  $\Delta f$  is inserted into eq. (4.25), a value of  $c_m$  smaller than the correct value results, because formula (4.25) is based on the assumption that the change in  $\vartheta$ , corresponding to adjacent maxima (or minima) equals  $2\pi$  exactly.

As the frequency decreases from the reference-frequency ( $\Delta\omega = 0$ ), the centre  $O_1^*$  in Fig. 19 may shift to  $O_1^{**}$ , the corresponding maxima of  $|Z_1|$  being  $A^*$  and  $A^{**}$ . A decrease in  $f$  corresponds to a decrease in  $\vartheta$ , and the circle for  $Z_{1i}$  is described counter-clockwise from  $A^*$  towards  $A^{**}$ .

Here too the change in  $\vartheta$  between  $A^*$  and  $A^{**}$  is less than  $2\pi$ , and the maxima or minima are spaced more closely than they would be if  $\vartheta$  equaled  $2\pi$ .

Thus the value for  $c_m$  found from formula (4.25) is less than the correct value, when derived from the maxima or minima on either side of the reference-frequency. The variable-frequency interferometer involves in principle an error of this nature in the determination of  $c_m$ ; the error might be made negligible if the shift of the centre  $O_1$  could be kept sufficiently small.

## APPENDICES

### A. Numerical values for the constants of an X-cut quartz crystal

#### 1. The bar in lengthwise vibration

The numerical values needed for the bar are  $s_{22}^E$ ,  $d_{12}$  and  $\epsilon_1^T$ , as seen from eqs. (1.1) and (1.2). The constants, converted to mks units, are taken from W. G. Cady [5]<sup>13</sup>. The page references below are from this book.

$$\begin{aligned} s_{22}^E &= s_{11}^E = 1.27 \cdot 10^{-11} \text{ m}^2/\text{newton (pp. 55 and 137)}, \\ d_{12} &= -d_{11} = -2.3 \cdot 10^{-12} \text{ coulomb/newton (p. 219)}, \\ \epsilon_1^T &= 4.0 \cdot 10^{-11} \text{ farad/m (} k_{\perp} \text{ on p. 414)}. \end{aligned}$$

From these quantities we derive

$$\begin{aligned} q^E &= 1/s_{22}^E = 7.9 \cdot 10^{10} \text{ newton/m}^2, \\ H &= d_{12}/s_{22}^E = -0.181 \text{ coulomb/m}^2, \\ H^2/\epsilon^T q^E &= 1.04 \cdot 10^{-2}. \end{aligned}$$

Thus the term  $H^2/\epsilon^T q^E$  can be regarded as small in comparison with unity, as repeatedly assumed. The relative difference between the frequencies for anti-resonance and series resonance for the free bar in the fundamental mode ( $n=0$ ) is given by eq. (2.10):

$$\frac{\omega_a - \omega_s}{\omega_s} = \frac{\Delta\omega}{\omega_s} = \frac{4}{\pi^2} \frac{H^2}{\epsilon^T q^E} \approx 4 \cdot 10^{-3}.$$

#### 2. The plate in thickness vibration

The constants needed for the plate are  $q^E = c_{11}^E$ ,  $H = e_{11}$ , and  $\epsilon_1^S$ , as seen from eqs. (1.25), (1.26), (1.27), (1.28):

$$\begin{aligned} q^E &= c_{11}^E = 8.7 \cdot 10^{10} \text{ newton/m}^2 \text{ (p. 137)}, \\ H &= e_{11} = 0.173 \text{ coulomb/m}^2 \text{ (p. 219)}, \\ \epsilon_1^S &= 3.9 \cdot 10^{-11} \text{ farad/m (} k_{\perp}' \text{ on p. 414)}. \end{aligned}$$

<sup>13</sup> Numerical values are also given in [3], pp. 90 and 91 and [15], pp. 84 and 85.

From this we obtain

$$\begin{aligned} H^2/\epsilon^S q^E &= 0.88 \cdot 10^{-2}, \\ q^D &= q^E \left( 1 + \frac{H^2}{\epsilon^T q^E} \right) = 8.8 \cdot 10^{10} \text{ newton/m}^2. \end{aligned}$$

Thus  $H^2/\epsilon^T q^D$ , which occurs in the treatment of the plate, is small compared with unity. The values for  $q^E$  and  $H$  are somewhat different for the plate and the bar, as stated already in Part I, Section 3, but still of the same order of magnitude.

The relative difference in frequency between series resonance and antiresonance for the free plate in the fundamental mode ( $n=0$ ) follows from eq. (2.19):

$$\frac{\omega_a - \omega_s}{\omega_a} = \frac{\Delta\omega}{\omega_a} = \frac{4}{\pi^2} \frac{H^2}{\epsilon^S q^D} = 3.5 \cdot 10^{-3}.$$

The value of  $\cot \varphi/2$  at series resonance of the free plate, neglecting crystal losses, follows from eq. (2.15):

$$\begin{aligned} \cot \varphi/2 &= \cot \frac{\omega_s l}{2 c_c} = \frac{2}{(2n+1)\pi} \frac{H^2}{\epsilon^S q^D} \\ &= \frac{(2n+1)\pi}{2} \frac{\Delta\omega}{\omega_a} \end{aligned}$$

and for the fundamental mode ( $n=0$ )

$$\cot \varphi/2 = \frac{\pi}{2} \frac{\Delta\omega}{\omega_a} = 5.5 \cdot 10^{-3}.$$

The slight departure of  $\cot \varphi/2$  from zero corresponds to the fact that the thickness of the free plate at series resonance is slightly different from  $\lambda_s/2$  in the fundamental mode. Indeed, we have

$$\frac{\omega_s l}{2 c_c} = \frac{(2n+1)\pi}{2} \left( 1 - \frac{\Delta\omega}{\omega_a} \right)$$

and hence for  $n=0$

$$l = \frac{\lambda_s}{2} \left( 1 - \frac{\Delta\omega}{\omega_a} \right) = 0.9965 \frac{\lambda_s}{2}.$$

Actually, as is well known, the frequency measured experimentally for series resonance of a free plate is somewhat higher than the theoretical value, owing to the fact that the plate is of finite area and not infi-



ninitely extended as assumed by the theory. The slight departure of  $l$  from  $\lambda_s/2$ , as found above, is therefore chiefly of theoretical interest.

### B. Numerical examples of interferometer impedances

As an illustration of the foregoing theoretical considerations we offer two numerical examples, one for water and one for air. In each case the ultrasonic source is an X-cut quartz plate.

#### 1. Medium: Water, $f_0 = 15$ Mc/s

The following data are used:

$$\rho_c = 2.65 \cdot 10^3 \text{ kg/m}^3,$$

$$c_c = 5.8 \cdot 10^3 \text{ m/s},$$

$$\rho_m = 1.0 \cdot 10^3 \text{ kg/m}^3,$$

$$c_m = 1.5 \cdot 10^3 \text{ m/s},$$

$$m_0 = \rho_m c_m / \rho_c c_c = 0.1 \quad (\text{eq. (3.17)}),$$

$$A = 1 \text{ cm}^2 = 10^{-4} \text{ m}^2, \quad |I| = 0.9,$$

$$2\alpha_m = 0.11 \text{ cm}^{-1} = 11 \text{ m}^{-1}.$$

From appendix A 2 we have  $H = 0.173$  coulomb/m<sup>3</sup> and  $q^D = 8.8 \cdot 10^{10}$  newton/m<sup>2</sup>.

The thickness of the plate is  $l = \lambda_c/2 = c_c/2 f_0 = 1.9 \cdot 10^{-4}$  m, assuming the plate to be driven at its fundamental antiresonant frequency (eq. (2.18)).

$z_0$  is found from eq. (3.22):

$$z_0 = \sqrt{q^D} \rho_c \frac{l^2}{2AH^2} = 92\,000 \text{ ohms}.$$

The wavelength in water is  $\lambda_m = c_m/f_0 = 10^{-4}$  m = 0.01 cm. The quantity  $\alpha_m \lambda_m = 0.00055 \ll 1$ ; according to eq. (4.1),  $m_1$  can be neglected in com-

parison with  $m_0$  and the centre of the circle for  $Z_{11}$  can be assumed to be on the real axis. A change in path length of  $\lambda_m/2$ , corresponding to a full turn around the  $Z_{11}$ -circle causes a contraction of the radius  $R$  in the  $r$ -plane by the factor  $e^{-\alpha_m \lambda_m} = 0.99945$ ; evidently this contraction can be ignored (see Part IV, Section 1 b).

We choose several different values for the path length  $d$ ; the corresponding  $R$  is found from eq. (3.27). The location of the centre  $x_C$  and the radius  $\rho$  of the  $(Z_{11}/z_0)$ -circle follows from eq. (3.34);  $y_C = 0$ , since  $m_1 = 0$  and  $\cot \varphi/2 = 0$ . Maxima and minima of  $|Z_{11}|$  are then given by  $z_0(x_C \pm \rho)$  or by eq. (4.10). Table I shows the results.

It is seen that the crystal is loaded considerably by the water-column even at the minimal values of  $|Z_{11}|$ , as has been remarked at the end of Part IV, Section 5. The resistance  $Z_{1c}$  of the free crystal may be assumed to have a value between 100 and 1000 ohms; it is of the same order of magnitude as  $|Z_{11}|_{\min}$  and can therefore not be ignored for frequencies of this order of magnitude. Since the order of magnitude of  $|Z_{11}|$  is proportional to  $m_0/f_0^2$  (eq. (3.22)),  $|Z_{11}|$  extends to much larger values when the frequency is lowered, so that the influence of  $Z_{1c}$  may become negligible at lower frequencies.

#### 2. Medium: Air at atmospheric pressure and 0° C, $f = 1$ Mc/s

Using  $\rho_m = 1.3 \text{ kg/m}^3$  and  $c_m = 331 \text{ m/s}$  one finds  $m_0 = 0.28 \cdot 10^{-4}$ . The reflection coefficient  $|I|$  may be computed according to a formula given by HERZFELD [10]:

Table I  
Water,  $f_0 = 15$  Mc/s, area = 1 cm<sup>2</sup>, X-cut quartz plate ( $l = \lambda_c/2$ ).

$d$	$2d/\lambda_m$	$R$	$x_C z_0$	$\rho z_0$	$ Z_{11} _{\max}$	$ Z_{11} _{\min}$	$\frac{ Z_{11} _{\max}}{ Z_{11} _{\min}}$
cm			ohms	ohms	ohms	ohms	
1	200	0.81	22150	21670	43810	480	91.2
2	400	0.72	14500	13750	28250	750	37.7
5	1000	0.52	8010	6560	14570	1450	10.0
10	2000	0.30	5510	3030	8540	2480	3.4
$\infty$	$\infty$	0	4600	0	4600	4600	1.0

Table II  
Air at atmospheric pressure,  $f_0 = 1$  Mc/s, area = 1 cm<sup>2</sup>,  
X-cut quartz plate ( $l = \lambda_c/2$ ).

$d$	$2d/\lambda_m$	$R$	$x_C z_0$	$\rho z_0$	$ Z_{11} _{\max}$	$ Z_{11} _{\min}$	$\frac{ Z_{11} _{\max}}{ Z_{11} _{\min}}$
cm			ohms	ohms	ohms	ohms	
1	60.6	0.64	717	651	1368	66	20.7
2	121.2	0.43	437	317	754	120	6.3
5	303.0	0.13	311	79	390	232	1.7
10	606.1	0.018	301	11	312	290	1.07
$\infty$	$\infty$	0	300	0	300	300	1.00

$$|I'| = 1 - 4.4 \cdot 10^{-5} \sqrt{f} = 0.96.$$

The coefficient of absorption may be found from [3], Table 64, p. 540:

$\alpha_m = 2 \cdot f^2 \cdot 10^{-13} = 0.2 \text{ cm}^{-1}$  or  $2 \alpha_m = 0.4 \text{ cm}^{-1}$ . The wavelength in air is  $\lambda_m = c_m/f_0 = 3.31 \cdot 10^{-4} \text{ m} = 3.31 \cdot 10^{-2} \text{ cm}$ . The quantity  $\alpha_m \lambda_m = 0.0066 \ll 1$ ; thus  $m_1$  as well as the contraction of a circle in the  $r$ -plane due to a change of  $\lambda_m/2$  in  $d$ , can be ignored (Part IV, Section 1). Table II gives the numerical values, computed in the same way as for water in Table I.

Owing to the considerably smaller value of  $m_0$  in comparison with the foregoing example for water the crystal is much less loaded by the air than by the water, although the frequency chosen in the case of air is 15 times smaller. This latter fact increases the ratio  $|Z_{1i}|/|Z_{1c}|$  by a factor  $(15)^2 = 225$ . When the frequency is further lowered,  $|Z_{1i}|$  rises to higher values by the factor  $1/f^2$  and the crystal becomes heavily loaded even by a gaseous medium.

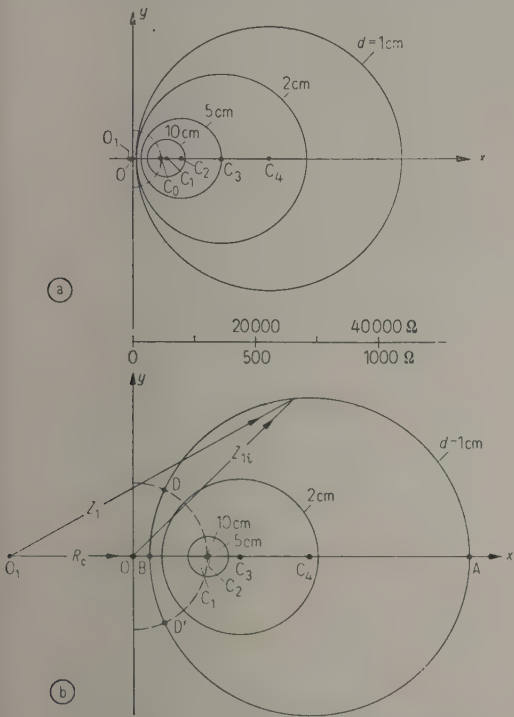


Fig. 20. Impedance diagrams for  $A=1 \text{ cm}^2$ ,  $R_c=500 \text{ ohms}$ , (a) water at 15 Mc/s, (b) air at 1 Mc/s.

Fig. 20 illustrates the two cases for water and air. In (b) the vector construction for  $Z_1=R_c+Z_{1i}$  is indicated. A similar construction would be used in (a).

### C. Note on the "free" (non-radiating) face of the piezoelectric crystal

All the results of the interferometer theory, as presented here, have been based upon the assumption that the crystal radiates into the medium within the interferometer path only, whereas the opposite surface is „free“, that is, non-radiating.

Actually the latter surface is usually bounded by air, rather than by vacuum, and the foregoing numerical example for air indicates that, especially at lower frequencies, the crystal may be considerably loaded at a surface bounded by a gaseous medium.

If the calculations in Part I are carried through with a modified boundary condition at  $x=0$ , corresponding to a load at  $x=0$  represented by an impedance  $Z_m'$  (or  $z_m'$ ), the following expression for the impedance  $Z_{1i}$  replaces eq. (3.20) <sup>14</sup>:

$$Z_{1i} = z_0 \frac{1 - 2j \cot \frac{\varphi}{2} \cdot \frac{z_m z_m'}{z_m + z_m'}}{2 \frac{\varphi}{z_m + z_m'} - j \cot \frac{\varphi}{2}} \quad (C1)$$

At resonance ( $l=\lambda_c/2$ ) the cotangent terms vanish and it is seen that  $z_m'$  simply constitutes an addition to  $z_m$ , the acoustic load of the interferometer path (cf. eq. (3.20)). Consequently at resonance we have to add an impedance  $Z_{1i}'$ , due to the gaseous medium at the free surface, to the impedance  $Z_{1i}$  of the interferometer path considered before. If a plane reflected wave on the free side of the crystal can be avoided by the use of highly absorbing material, or suitable configuration of the reflecting surface, or by having the path sufficiently long,  $Z_{1i}'$  equals  $m_0 z_0/2$  (eq. (3.29)). As seen from the previous example for air,  $Z_{1i}'$  then equals 300 ohms at  $f=1 \text{ Mc/s}$  for an area  $A$  of  $1 \text{ cm}^2$ .  $Z_{1i}'$  increases with  $1/f^2$ , becoming 30 000 ohms at 100 kc/s. If the radiation into the free side strikes some obstacle and produces a reflected plane wave, the gaseous path behaves like another fixed-path interferometer in series with the true interferometer, and  $Z_{1i}'$  may induce a considerable complex impedance in addition to  $Z_{1i}$ . Proper attention therefore should be given to the "free" surface of the crystal. The effect of  $Z_{1i}'$  is minimized when a plane reflector parallel

<sup>14</sup> It may be noted that eq. (C1) also describes the effect of a piezoelectric plate which is inserted normally to the direction of propagation of a plane compressional wave and which is loaded at its input by an electric impedance  $Z_{AB}$ . One only has to solve eq. (C1) for  $z_m'$  and to replace  $Z_{1i}$  by the expression  $[Z_{AB}/(1-j\omega C Z_{AB})] - Z_{1c}$  (see Fig. 8). However, the formula so obtained applies only to the case in which the centre of gravity of the plate is considered to be at rest.



and close to the free crystal surface is located at a distance of  $(2n+1)\lambda/4$ .

The author is indebted to Dr. W. G. CADY for many stimulating discussions.

(Received July, 1st 1955.)

### Symbols

$A$	electrode area,
$b$	$= \cot \varphi/2$ ,
$C_1, C_I$	parallel and series capacitance in the equivalent circuits of Figs. 3 and 5, eqs. (1.23), (1.43), (1.45),
$C_b, C_p$	$= C$ in Fig. 6, specialized for bar and plate, eqs. (2.6), (2.17),
$c_c, c_m$	velocity of sound in crystal and medium,
$D$	electric displacement,
$d$	length of interferometer path (Figs. 1 and 7),
$d_m$	interferometer path-length corresponding to a maximum or minimum of the electric impedance $Z_{ij}$ , eq. (4.21),
$E$	electric field-strength,
$F$	dissipation constant, eq. (1.9),
$f$	frequency $= \omega/2\pi$ ,
$H$	piezoelectric constant, eqs. (1.3), (1.4) and (1.27), (1.28),
$I$	current at crystal input,
$L_b, L_p$	$= L$ in Fig. 6, specialized for bar and plate, eqs. (2.6), (2.17),
$l$	length of crystal bar (Fig. 2) and thickness of crystal plate (Fig. 4),
$m$	$= \gamma_m q_m / \gamma_c q_c = m_0 + j m_1$ , eq. (3.17),
$n$	$= 0, 1, 2, 3, \dots$ ,
$q^E, q^D$	elastic stiffness, eqs. (1.3), (1.4), (1.27), (1.30),
$q_c$	$q_{c0} + j \omega F = q^E$ for a bar or $q^D$ for a plate, eq. (1.9),
$q_m$	$= q_{m0} + j \omega F$ , eq. (3.3),
$R_b, R_p$	$= R$ in Fig. 6, specialized for bar and plate, eqs. (2.5), (2.16),
$R_c$	loss-resistance of the crystal due to absorption and mounting,
$R$	$=  F  e^{-2\gamma_m d}$ , eq. (3.27),
$r$	$= R e^{-j\phi}$ , eq. (3.26),
$S, T$	strain and stress,
$t$	thickness of the crystal bar, Fig. 2,
$V$	sinusoidal driving voltage at crystal input,
$w$	$= x + j y = Z_{11}/z_0$ , eq. (3.32),
$w$	$= x + j y = z_0 Y_{11}$ , eq. (4.8),
$x_c, y_c$	coordinates of the centre of a circle in the $w$ -plane eq. (3.34),
$x_c, y_c$	coordinates of the centre of a circle in the $w$ -plane, eq. (4.9),
$Y$	$= 1/Z$ electric admittance,
$Z_1, Z_I$	electric impedance, Figs. 3, 5, 8,
$Z_m$	mechanical impedance of the interferometer path, eqs. (1.14) and (3.1),
$Z_{1c}$	electric impedance of the free crystal, Fig. 3,
$Z_{1i}$	electric impedance of the interferometer path, Fig. 8, eq. (3.23),
$Z_{II}$	$P - j Q$ HUBBARD's electric impedance of the interferometer path, eq. (4.5),
$z_0$	see eq. (3.21) and (3.22),
$z_m$	$(\omega/\gamma_c q_c) Z_m$ , eqs. (1.16), (1.36),
$\alpha_c, \alpha_m$	amplitude absorption coefficient in space for crystal and medium (in Part II $\alpha$ is written in place of $\alpha_c$ ),

$\gamma_c$	$= (\omega/c_c) - j \alpha_c = \omega \sqrt{\rho_c/q^E}$ for the bar, and $\omega \sqrt{\rho_c/q^D}$ for the plate, eq. (1.11),
$\gamma_m$	$= (\omega/c_m) - j \alpha_m$ , eq. (3.24),
$\Gamma$	$=  \Gamma  e^{j\theta}$ reflection coefficient, eq. (3.8),
$\epsilon^T, \epsilon^S$	permittivity, eqs. (1.2), (1.26),
$\Theta$	phase angle of the reflection coefficient, eq. (3.8),
$\theta$	$= 2\omega(d/c_m) - \Theta = 4\pi(d/\lambda_m) - \Theta$ , eq. (3.27),
$\lambda_c, \lambda_m$	acoustic wave length in crystal and medium,
$\rho_c, \rho_m$	density of crystal and medium,
$\varrho, \varrho'$	radius of circles in the $w$ - and $w'$ -planes, eqs. (3.34), (4.9),
$\sigma$	$= \sqrt{\frac{ Z_{1i} _{\min}}{ Z_{1i} _{\max}}} = \sqrt{\frac{ Y_{1i} _{\min}}{ Y_{1i} _{\max}}}$ , eq. (4.12),
$\varphi$	$= \gamma_c l = \omega(l/c_c) - j \alpha_c l = 2\pi(l/\lambda_c) - j \alpha_c l$ ,
$\omega_s$	angular frequency for series-resonance of the free crystal, eqs. (2.4), (2.15),
$\omega_a$	angular frequency for antiresonance of the free crystal, eqs. (2.9), (2.18),
$\omega$	$= 2\pi f$ .

### References

- [1] BECHMANN, R., Dickenschwingungen piezoelektrisch erregter Kristallplatten. Hochfrequenz-techn. u. Elektroakustik **56** [1940], 14.
- [2] BECHMANN, R., Einige Anwendungen der piezoelektrischen Zustandsgleichungen. Arch. elektr. Übertragung **9** [1955], 122.
- [2 a] BECHMANN, R., Über Dickenschwingungen piezoelektrischer Kristallplatten. Arch. elektr. Übertragung **6** [1952], 361.
- [3] BERGMANN, L., Der Ultraschall; 6th ed. S. Hirzel Verlag, Stuttgart 1954.
- [4] BORGNIS, F. E., On the theory of the fixed path acoustic interferometer. J. acoust. Soc. Amer. **24** [1952], 19.
- [5] CADY, W. G., Piezoelectricity. McGraw-Hill Book Co., New York 1946.
- [6] CADY, W. G., A theory of the crystal transducer for plane waves. J. acoust. Soc. Amer. **21** [1949], 65.
- [7] CADY, W. G., Piezoelectric equations of state and their application to thickness-vibration transducers. J. acoust. Soc. Amer. **22** [1950], 579.
- [8] FORSYTH, A. R., Theory of functions of a complex variable; 2nd edition. University Press, Cambridge (England), p. 605, Section 258.
- [9] FOX, F. E., Ultrasonic interferometry for liquid media. Phys. Rev. **52** [1937], 973.
- [10] FOX, F. E. and HUNTER, T. L., The ultrasonic interferometer with resonant liquid column. Proc. Inst. Radio Engrs. **36** [1948], 1500.
- [11] HERZFELD, K. F., Reflection of sound. Phys. Rev. **53** [1938], 899.
- [12] HUBBARD, J. C., The acoustic resonator interferometer: 1: The acoustic system and its equivalent electric network; 2: Ultrasonic velocity and absorption in gases. Phys. Rev. **38** [1931], 1011 and **41** [1932], 523.
- [13] HUBBARD, J. C. and ZARTMAN, I. F., A fixed path acoustic interferometer for the study of matter. Rev. sci. Instrum. **10** [1939], 382.
- [14] KOSTEN, C. W., A new method for measuring sound absorption. Appl. Sci. Res. **B 1** [1947], 35.
- [15] MASON, W. P., Piezoelectric crystals and their application to ultrasonics. Van Nostrand Co., New York 1950, p. 61.

# ZUR SYSTEMATIK DER ELASTISCHEN EIGENSCHWINGUNGEN ISOTROPER KREISZYLINDER

von E. SITTIG

1. Physikalisches Institut der Technischen Hochschule, Stuttgart

## Zusammenfassung

Die elastische Grundgleichung des isotropen Festkörpers liefert für den Grenzfall des unendlich langen Kreiszylinders außer den einfachen Lösungen, welche die Typen der Torsions-, Longitudinal- und Biegeschwingungen beschreiben, auch noch kompliziertere. Es wird gezeigt, daß insgesamt eine dreifach abzählbare Schar von Resonanzen auftritt, sich also eine jede Resonanz durch ein Tripel ganzer Zahlen  $(n, p, q)$  indizieren läßt. Diese Indizes lassen sich mit den Schwingungsknoten auf der Zylinderoberfläche in Beziehung bringen und sind durch diese experimentell zu bestimmen.

Da sich das Randwertproblem für den Zylinder endlicher Länge nicht streng lösen läßt, sind bei der experimentellen Nachprüfung gewisse Abweichungen zu erwarten. Für den Spezialfall der Resonanzen mit verschwindender Axialkomponente kann man jedoch durch den Vergleich mit den Werten der entsprechenden Resonanzen einer dünnen Kreisplatte den Fehler eingrenzen.

## Summary

The fundamental equations for the isotropic elastic solid in the form of an infinite circular cylinder yield, beside the simple modes of vibration (longitudinal, torsional, flexural), more complicated modes. Altogether there is a threefold band of resonances with each resonance characterised by a triplet of integral indices  $(n, p, q)$  which are related to the nodes on the cylindrical surface and can be experimentally determined.

As the boundary problem of the cylinder of finite length cannot be rigorously solved, some departure from experiment is to be anticipated. For the special case of resonances with vanishing axial components, the discrepancies can be limited by comparison with the corresponding resonances of a thin circular disc.

## Sommaire

L'équation fondamentale de l'élasticité du corps solide isotrope admet, dans le cas limite d'un cylindre circulaire de longueur indéfinie, non seulement les solutions simples qui correspondent aux types d'oscillations de torsion, longitudinales et de flexion, mais encore des solutions plus compliquées. On montre, dans le présent travail, qu'il apparaît en tout une famille triple de résonances, de sorte que chaque résonance peut être indicée sous la forme d'un triplet de nombres entiers  $(n, p, q)$ . On peut établir une relation entre les indices et les noeuds d'oscillation à la surface du cylindre, et ainsi déterminer expérimentalement ces indices.

Comme il n'est pas possible de résoudre de façon rigoureuse le problème des valeurs aux limites dans le cas d'un cylindre de longueur indéfinie, il faut s'attendre à trouver certains écarts dans la vérification expérimentale de la théorie. Toutefois, dans le cas particulier des résonances à composante axiale nulle, on peut limiter l'erreur par comparaison avec les valeurs des résonances correspondantes d'une plaque circulaire mince.

## 1. Einleitung

Für die Vermessung der elastischen Konstanten eines isotropen Festkörpers bieten sich seine elastischen Eigenschwingungen als bequemes und genaues Meßmittel an. Deren Frequenzen können bei Anwendung moderner elektronischer Methoden mindestens ebenso genau wie die geometrischen Abmessungen des Probekörpers bestimmt werden. Als solcher wird der genauen Herstellbarkeit wegen oft ein kreiszylindrischer Stab verwendet, und mit solchen Kreiszylindern sollen sich die folgenden Ausführungen ausschließlich befassen.

Die elementare Theorie unterscheidet im wesentlichen drei verschiedene Schwingungstypen: Tor-

sions-, Dehnungs- und Biegeschwingungen. Die bekannten Formeln für deren Phasengeschwindigkeiten und Eigenfrequenzen finden sich beispielsweise bei RAYLEIGH [1]. Indessen konstatierte dieser schon die Komplikationen, die durch die mit einer Längsdilatation verbundene Querkontraktion verursacht werden, und er gab Korrektionsformeln hierfür an. Schon die ersten, nach der Entwicklung der Ultraschalltechnik möglich gewordenen Messungen von BOYLE und SPROULE [2], RÖHRICH [3], SCHÖNECK [4] sowie SHEAR und FOCKE [5] zeigten aber die Unzulänglichkeit dieser Korrektionsformeln für größere Frequenzbereiche. Damit gewann eine bereits seit längerer Zeit bekannte theoretische Behandlungsweise an Interesse, die von der durch die allgemeine



Elastizitätstheorie gelieferten Bewegungsgleichungen des elastisch-isotropen Festkörpers ausgeht. Diese, erstmals von POCHHAMMER [6] angegeben, gilt streng nur für Stäbe unendlicher Länge, stellt aber mindestens qualitativ die auftretenden Erscheinungen befriedigend dar. Sie liefert für jeden Schwingungstyp eine Gleichung, die sogenannte Frequenzgleichung, die die Phasengeschwindigkeit des Schwingungsvorganges mit seiner Frequenz verknüpft. Diese Gleichungen haben im allgemeinen eine abzählbare Schar von Lösungen, die geometrische und elastische Daten des Stabes als Parameter enthalten.

## 2. Die Herleitung der allgemeinen Frequenzgleichung

Die oben erwähnte Bewegungsgleichung lautet für den Fall des isotropen, kräftefreien Festkörpers [7]

$$\varrho \frac{\partial^2 \vec{s}}{\partial t^2} = (A + 2G) \text{grad div } \vec{s} - G \text{rot rot } \vec{s}, \quad (1)$$

worin  $\vec{s}$  den Verschiebungsvektor,  $A$  die LAMÉsche Elastizitätskonstante des Materials,  $G$  seinen Torsionsmodul und  $\varrho$  seine Dichte bedeutet. Führt man die Zeitdifferentiation unter der Annahme sinusförmig periodischer Zeitabhängigkeit der Kreisfrequenz  $\omega$  aus, so nimmt Gl. (1) bei Verwendung der Abkürzungen

$$v_T = \sqrt{\frac{G}{\varrho}}, \quad v_L = \sqrt{\frac{A + 2G}{\varrho}} \quad (2)$$

die Form

$$0 = \omega^2 \vec{s} + v_L^2 \text{grad div } \vec{s} - v_T^2 \text{rot rot } \vec{s} \quad (3)$$

an. Setzt man in Zylinderkoordinaten

$$\vec{s} = (u_r, u_\varphi, u_z),$$

so lautet Gl. (3) ausgeschrieben

$$0 = \omega^2 u_r + v_L^2 \frac{\partial \text{div } \vec{s}}{\partial r} - v_T^2 \left( \frac{1}{r} \frac{\partial \Omega_z}{\partial \varphi} - \frac{\partial \Omega_\varphi}{\partial z} \right),$$

$$0 = \omega^2 u_\varphi + v_L^2 \frac{1}{r} \frac{\partial \text{div } \vec{s}}{\partial \varphi} - v_T^2 \left( \frac{\partial \Omega_r}{\partial z} - \frac{\partial \Omega_z}{\partial r} \right),$$

$$0 = \omega^2 u_z + v_L^2 \frac{\partial \text{div } \vec{s}}{\partial z} - v_T^2 \frac{1}{r} \left( \frac{\partial (r \Omega_\varphi)}{\partial r} - \frac{\partial \Omega_r}{\partial \varphi} \right) \quad (4)$$

mit

$$\text{div } \vec{s} = \frac{1}{r} \frac{\partial (r u_r)}{\partial r} + \frac{1}{r} \frac{\partial u_\varphi}{\partial \varphi} + \frac{\partial u_z}{\partial z},$$

$$\Omega_r = \frac{1}{r} \frac{\partial u_z}{\partial \varphi} - \frac{\partial u_\varphi}{\partial z},$$

$$\Omega_\varphi = \frac{\partial u_r}{\partial z} - \frac{\partial u_z}{\partial r},$$

$$\Omega_z = \frac{1}{r} \left( \frac{\partial (r u_r)}{\partial r} - \frac{\partial u_r}{\partial \varphi} \right), \quad (5)$$

wobei zwischen den drei letzten Formeln von Gl. (5) die Identität

$$\frac{1}{r} \frac{\partial (r \Omega_r)}{\partial r} + \frac{1}{r} \frac{\partial \Omega_\varphi}{\partial \varphi} + \frac{\partial \Omega_z}{\partial z} = 0 \quad (6)$$

besteht. Durch geeignetes Weiterdifferenzieren und Umrechnen erhält man aus Gl. (4) die drei Gleichungen

$$\left( \frac{\partial^2}{\partial r^2} + \frac{1}{r} \frac{\partial}{\partial r} + \frac{1}{r^2} \frac{\partial^2}{\partial \varphi^2} + \frac{\partial^2}{\partial z^2} + \frac{\omega^2}{v_L^2} \right) \text{div } \vec{s} = 0, \quad (7)$$

$$\left( \frac{\partial^2}{\partial r^2} + \frac{1}{r} \frac{\partial}{\partial r} + \frac{1}{r^2} \frac{\partial^2}{\partial \varphi^2} + \frac{\partial^2}{\partial z^2} + \frac{\omega^2}{v_T^2} \right) \Omega_z = 0, \quad (8)$$

$$\begin{aligned} & \left( \frac{\partial^2}{\partial r^2} + \frac{3}{r} \frac{\partial}{\partial r} + \frac{1}{r^2} \frac{\partial^2}{\partial \varphi^2} + \frac{\partial^2}{\partial z^2} + \frac{\omega^2}{v_T^2} + \frac{1}{r^2} \right) \Omega_r \\ & = - \frac{2}{r} \frac{\partial \Omega_z}{\partial z}, \end{aligned} \quad (9)$$

welche nach Einführen des Lösungsansatzes

$$u_r = U(r) \cos n \varphi e^{-i\omega z/v},$$

$$u_\varphi = V(r) \sin n \varphi e^{-i\omega z/v}, \quad (10)$$

$$u_z = W(r) \cos n \varphi e^{-i\omega z/v};$$

$$n = 0, 1, 2, \dots$$

in die Besselschen Differentialgleichungen

$$\left( \frac{\partial^2}{\partial r^2} + \frac{1}{r} \frac{\partial}{\partial r} + h^2 - \frac{n^2}{r^2} \right) \text{div } \vec{s} = 0, \quad (11)$$

$$\left( \frac{\partial^2}{\partial r^2} + \frac{1}{r} \frac{\partial}{\partial r} + k^2 - \frac{n^2}{r^2} \right) \Omega_z = 0, \quad (12)$$

$$\left( \frac{\partial^2}{\partial r^2} + \frac{3}{r} \frac{\partial}{\partial r} + k^2 - \frac{n^2 - 1}{r^2} \right) \Omega_r = -i \frac{\omega}{v} \frac{2}{r} \Omega_z \quad (13)$$

mit

$$\begin{aligned} h^2 &= \omega^2 \left( \frac{1}{v_L^2} - \frac{1}{v^2} \right), \\ k^2 &= \omega^2 \left( \frac{1}{v_T^2} - \frac{1}{v^2} \right) \end{aligned} \quad (14)$$

übergehen.

Bezeichnen nun  $A, B, C$  beliebige Konstanten, so lauten die mit der Endlichkeitsforderung für  $r=0$  verträglichen Lösungen

$$\text{div } \vec{s} = A J_n(hr), \quad (15)$$

$$\Omega_z = C J_n(kr), \quad (16)$$

$$\Omega_r = \frac{B}{r} J_n(kr) - i \frac{\omega/v}{k^2} C \frac{\partial J_n(kr)}{\partial r}. \quad (17)$$

Diese sind in die Gl. (5) einzuführen. Man erhält dann vier Gleichungen für die drei Komponenten  $U, V, W$ , aber von diesen sind wegen Gl. (6) nur drei unabhängig. Bildet man also etwa aus der 1., 2. und 4. Formel von Gl. (5) ein unabhängiges System, so ist der Lösungsansatz hierfür

$$\begin{aligned}
 U &= -\frac{A'}{\omega^2/v_L^2} \frac{\partial J_n(hr)}{\partial r} + \frac{B'}{\omega^2/v_T^2} \frac{\partial J_n(kr)}{\partial r} + \frac{C'}{k^2} \frac{n J_n(kr)}{r}, \\
 V &= \frac{A'}{\omega^2/v_L^2} \frac{n J_n(hr)}{r} - \frac{B'}{\omega^2/v_T^2} \frac{n J_n(kr)}{r} - \frac{C'}{k^2} \frac{\partial J_n(kr)}{\partial r}, \\
 W &= i \frac{A'}{\omega^2/v_L^2} \frac{\omega}{v} J_n(hr) + i \frac{B'}{\omega^2/v_T^2} \frac{k^2}{\omega/v} J_n(kr).
 \end{aligned}
 \tag{18}$$

Die hierin enthaltenen Konstanten  $A'$ ,  $B'$ ,  $C'$  sind durch das Randwertproblem zu bestimmen. Dieses Randwertproblem wird durch die Forderung des Verschwindens sämtlicher Spannungen auf der Zylinderoberfläche formuliert. Ist  $a$  der Radius des Zylinders und  $L$  seine Länge, so lautet es

$$\begin{aligned}
 P_{rr} &= \Delta \operatorname{div} \vec{s} + 2G \frac{\partial u_r}{\partial r} = 0 \quad \text{für } r=a, & P_{zr} &= P_{rz} = 0 \quad \text{für } z=0, L, \\
 P_{r\varphi} &= G \left[ \frac{1}{r} \frac{\partial u_r}{\partial \varphi} + r \frac{\partial}{\partial r} \left( \frac{u_\varphi}{r} \right) \right] = 0 \quad \text{für } r=a, & P_{z\varphi} &= G \left( \frac{\partial u_\varphi}{\partial z} + \frac{1}{r} \frac{\partial u_z}{\partial \varphi} \right) = 0 \quad \text{für } z=0, L, \\
 P_{rz} &= G \left( \frac{\partial u_r}{\partial z} + \frac{\partial u_z}{\partial r} \right) = 0 \quad \text{für } r=a; & P_{zz} &= \Delta \operatorname{div} \vec{s} + 2G \frac{\partial u_z}{\partial z} = 0 \quad \text{für } z=0, L.
 \end{aligned}
 \tag{19}$$

Zunächst seien die durch die ersten drei Formeln von Gl. (19) gestellten Bedingungen behandelt: Setzt man die durch Gl. (10) mit Gl. (18) gegebenen Lösungen darin ein, so erhält man ein homogenes lineares Gleichungssystem für die Konstanten  $A'$ ,  $B'$ ,  $C'$ , das sich nur erfüllen läßt, wenn die Determinante der Koeffizienten verschwindet. Mit den Bezeichnungen

$$\tau = \frac{a \omega}{v}, \quad x = \frac{1}{2} \frac{v^2}{v_T^2}, \quad \Theta_n(y) = \frac{y J_{n-1}(y)}{J_n(y)}
 \tag{20}$$

nimmt diese die Form

$$\begin{vmatrix}
 n^2 - 1 - \tau^2(x-1) & n^2 - 1 - \tau^2(2x-1) & 2(n^2-1)[\Theta_n(ka) - n] - \tau^2(2x-1) \\
 \Theta_n(ha) - n - 1 & \Theta_n(ka) - n - 1 & 2n^2 - 2[\Theta_n(ka) - n] - \tau^2(2x-1) \\
 \Theta_n(ha) - n & -(x-1)[\Theta_n(ka) - n] & n^2
 \end{vmatrix} = 0
 \tag{21}$$

an. Sie ist identisch mit der von HUDSON [8] angegebenen Frequenzgleichung. Ist Gl. (21) erfüllt, so kann man aus zweien der drei ersten Formeln von Gl. (19) die Konstantenverhältnisse  $A'/C'$  und  $B'/C'$  ausrechnen und erhält endlich

$$\begin{aligned}
 U &= C'' \left[ -A'' \frac{\partial J_n(hr)}{\partial r} + B'' \frac{\partial J_n(kr)}{\partial r} + n \frac{J_n(kr)}{r} \right], \\
 V &= C'' \left[ A'' n \frac{J_n(hr)}{r} - B'' n \frac{J_n(kr)}{r} - \frac{\partial J_n(kr)}{\partial r} \right], \\
 W &= C'' \left[ i A'' \frac{\omega}{v} J_n(hr) + i B'' \frac{k^2}{\omega/v} J_n(kr) \right]
 \end{aligned}
 \tag{22}$$

mit

$$\begin{aligned}
 A'' &= \frac{1}{2n} \frac{\begin{vmatrix} 2(n^2-1)[\Theta_n(ka) - n] - \tau^2(2x-1) & n^2 - 1 - \tau^2(2x-1) \\ 2n^2 - 2[\Theta_n(ka) - n] - \tau^2(2x-1) & \Theta_n(ka) - n - 1 \end{vmatrix}}{\begin{vmatrix} n^2 - 1 - \tau^2(x-1) & n^2 - 1 - \tau^2(2x-1) \\ \Theta_n(ha) - n - 1 & \Theta_n(ka) - n - 1 \end{vmatrix}}, \\
 B'' &= \frac{1}{2n} \frac{\begin{vmatrix} n^2 - 1 - \tau^2(x-1) & 2(n^2-1)[\Theta_n(ka) - n] - \tau^2(2x-1) \\ \Theta_n(ha) - n - 1 & 2n^2 - 2[\Theta_n(ka) - n] - \tau^2(2x-1) \end{vmatrix}}{\begin{vmatrix} n^2 - 1 - \tau^2(x-1) & n^2 - 1 - \tau^2(2x-1) \\ \Theta_n(ha) - n - 1 & \Theta_n(ka) - n - 1 \end{vmatrix}}.
 \end{aligned}
 \tag{23}$$

Geht man mit den nunmehr bestimmten Ausdrücken für  $u_r$ ,  $u_\varphi$ ,  $u_z$  in die letzten drei Formeln von Gl. (19) ein, so erweist sich das vorliegende Randwertproblem als überbestimmt, indem das gleichzeitige Verschwinden von  $\cos \omega(Lv)$  und  $\sin \omega(Lv)$  gefordert wird. Hierdurch wird der Näherungscharakter der so gewonnenen Lösungsdarstellung bedingt.



### 3. Diskussion der Frequenzgleichung

Jeder ganzzahlige Wert  $n$  in Gl. (21) liefert eine Darstellung des Typs

$$\frac{v}{v_T} = f\left(\tau, \frac{v_T}{v_L}\right) \quad \text{oder} \quad \frac{v}{v_T} = F(\tau, \sigma), \quad (24)$$

da ja  $v_T/v_L$  eine Funktion der Querkontraktionszahl  $\sigma$ , nämlich

$$\frac{v_T}{v_L} \equiv \alpha = \sqrt{\frac{1-2\sigma}{2(1-\sigma)}}, \quad 0 \leq \sigma \leq 0,5 \quad (25)$$

ist. Wegen der Quasiperiodizität der Besselfunktionen wird diese Darstellung (24) mehrdeutig, sie ist also für jeden festen Wert von  $\sigma$  durch eine Schar abzählbar vieler Kurvenäste wiederzugeben. Jeder dieser Äste kann durch eine ganze Zahl  $p$  indiziert werden und liefert eine Serie von Resonanzen, deren diskrete Frequenzwerte durch die Periodizität der  $z$ -Abhängigkeit in den Randbedingungen für die Endflächen des Zylinders bestimmt sind. Diese wiederum können durch eine Laufzahl  $q$  indiziert werden. Eine jede Resonanz ist demnach durch drei Indizes bestimmt:

1.  $n$  als Index für den Schwingungstyp,
2.  $p$  als Index für die Schwingungsserie des Typs,
3.  $q$  als Ordnungszahl innerhalb einer Serie.

Für  $n=0$  spaltet Gl. (21) auf in das Produkt der Gleichungen

$$2 \Theta_0(ka) = \tau^2 (2x-1), \quad (26)$$

$$x \Theta_0(ha) \Theta_0(ka) + \tau^2 (x-1)^2 \Theta_0(ka) + \tau^2 (2x-1) \Theta_0(ha) = 0, \quad (27)$$

welche zweckmäßigerweise mittels der Rekursionsformel

$$\Theta_n(y) = 2n - \frac{y^2}{\Theta_{n+1}(y)} \quad (28)$$

$$\text{in} \quad \Theta_1(ka) = 2 \quad (29)$$

und

$$(x-1)^2 \Theta_1(ha) = (2\alpha^2 x-1) [\Theta_1(ka) - x] \quad (30)$$

übergeführt werden. Gl. (30) ist die POCHHAMMERsche Frequenzgleichung. Einsetzen in Gl. (22) zeigt, daß Gl. (29) den Torsionstyp

$$U=0, \quad V = \begin{cases} C'' r & \text{für } k=0 \\ C'' J_1(kr) & \text{für } k>0 \end{cases}, \quad W=0 \quad (31)$$

beschreibt, hingegen Gl. (30) den Longitudinaltyp

$$U = C'' [A'' J_1(hr) - B'' J_1(kr)], \quad V=0, \quad (32)$$

$$W = C'' \left[ A'' i \frac{\omega}{v} J_0(hr) + B'' i \frac{k^2}{\omega/v} J_0(kr) \right].$$

Beim Torsionstyp liegen einfache Verhältnisse vor: Gl. (29) hat abzählbar viele und nur reelle Lösungen  $y_p = ka$ , deren jede entsprechend der Definition

(14) einen Kurvenast

$$2x = \frac{y_p^2}{\tau^2} + 1 \quad (33)$$

liefert.

Die numerische Auswertung von Gl. (29) ergibt

Tabelle I

$y_1 =$	0
$y_2 =$	5,136
$y_3 =$	8,417
$y_4 =$	11,620
$y_5 =$	14,795
...	...

$y_1=0$  bedeutet  $k=0$ , also  $v=v_T$ . Dies ist die bekannte, auch elementar zu berechnende Torsionsserie. Hiermit ist  $v_T$  eine anschauliche Bedeutung unterlegt.

Für die höheren  $y_p$  entstehen  $p$  zur Achse konzentrische Knotenzylinder, wenn man die Achse selbst als solchen mitzählt.

Das Randwertproblem auf den Endflächen ist hier streng lösbar und führt auf die Eigenwerte

$$\lambda \equiv \frac{2\pi v}{\omega} = \frac{2l}{q}, \quad q=1, 2, \dots \quad (34)$$

Beim Longitudinaltyp, der durch Gl. (30) und (32) beschrieben wird, treten insofern Komplikationen auf, als keine explizite Darstellung der einzelnen Serien mehr möglich ist, und diese überdies von der Querkontraktionszahl  $\sigma$  abhängig werden. Eine Tabelle des untersten Astes wurde von BANCROFT [9] mitgeteilt, eine solche der beiden nächsthöheren von DAVIES [10]. HÜTER [11] und HOLDEN [12] geben graphische Übersichtsverfahren an.

Folgende Spezialfälle seien noch erwähnt:

- a) Für  $a \rightarrow 0$  wird  $v=v_D = \sqrt{E/\rho}$ . Hierin ist  $E=2G(1+\sigma)$  der übliche Elastizitätsmodul.
- b) Für  $v=v_L$  reduziert sich Gl. (30) auf  $J_1(ka)=0$ , was allgemein durch  $a \rightarrow \infty$  erfüllt wird. Damit erhält auch  $v_L$  seine anschauliche Bedeutung.
- c) Für  $x=1$  reduziert sich Gl. (30) auf

$$\Theta_1(\xi) = 1 \quad \text{mit} \quad \xi = \tau. \quad (35)$$

Die numerische Auswertung ergibt

Tabelle II

$\xi_0 =$	1,842
$\xi_1 =$	5,333
$\xi_2 =$	8,533
$\xi_3 =$	11,785
...	...

Diese Werte liefern in jeder Serie einen von  $\sigma$  unabhängigen Kontrollpunkt.

Das Randwertproblem auf den Endflächen erweist sich hier als nicht mehr streng lösbar, wegen der

Phasenverschiebung der Radial- gegen die Axialkomponente. Wählt man die Wellenlänge  $\lambda$  wie in Gl. (34), so wird  $P_{zz}=0$ , und da wegen  $P_{zr}=P_{rz}$  und wegen des Bestehens von Gl. (30) jedenfalls  $P_{zr}=0$  für  $r=a$  gilt, wird für kleine  $\tau$  auch  $P_{zr}$  über die ganzen Endflächen hin klein bleiben.

Der Typ der Biegeschwingungen wird durch  $n=1$  charakterisiert. Von HUDSON [8] liegt eine Tabelle der untersten Serie vor. Höhere Serien sind nach Wissen des Verfassers noch nicht behandelt.

Das Randwertproblem auf den Endflächen ist hier nicht streng lösbar.

Typen mit  $n>1$  sind in der Literatur noch nicht erwähnt, aber experimentell nachweisbar [13].

4. Die Radial-Azimutal-Schwingungen

Rechnet man Gl. (21) auf den frequenzproportionalen Parameter

$$\tau_0 = a \omega / v_T, \quad \tau_0^2 = 2 x \tau^2 \tag{36}$$

um, so läßt sich der Grenzübergang  $x \rightarrow \infty$  vollziehen und man erhält, von einem Faktor  $[\Theta_n(\tau_0) - n]$  abgesehen,

$$\left| \begin{array}{cc} n^2 - 1 - \frac{\tau_0^2}{2} & 2(n^2 - 1) [\Theta_n(\tau_0) - n] - \tau_0^2 \\ \Theta_n(\alpha \tau_0) - n - 1 & 2n^2 - 2[\Theta_n(\tau_0) - n] - \tau_0^2 \end{array} \right| = 0. \tag{37}$$

Einsetzen in Gl. (22) zeigt, daß für die hierdurch

Gl. (39) eine rein radiale. Gl. (39) ist identisch mit der AIRYSchen Frequenzgleichung [14].

Für den azimutalen Typ als einzigen lassen sich die Randbedingungen auf den Endflächen streng erfüllen.

Interessant ist nun der Vergleich mit den entsprechenden Schwingungen einer dünnen Kreisplatte. Deren Frequenzgleichung [15] lautet

$$\left| \begin{array}{cc} n^2 - 1 - \frac{\tau_0^2}{2} & 2(n^2 - 1) [\Theta_n(\tau_0) - n] - \tau_0^2 \\ \Theta_n(\beta \tau_0) - n - 1 & 2n^2 - 2[\Theta_n(\tau_0) - n] - \tau_0^2 \end{array} \right| = 0 \tag{40}$$

mit 
$$\beta^2 = \frac{1 - \sigma}{2}. \tag{41}$$

Im Falle des Zylinders verschwinden bei diesen Schwingungen die Spannungen  $P_{zr}$  und  $P_{z\varphi}$ . Hingegen wird  $P_{zz} \sim J_n(\alpha \tau_0)$ . Mit wachsendem  $n$  und wachsender Laufzahl  $p$ , die hier die Rolle der Ordnungszahl der Resonanzen übernimmt, werden nun die Endflächen von einem immer dichteren Netz von Knotenradien und zur Achse konzentrischen Knotenkreisen für  $P_{zz}$  überzogen, zwischen denen aus Stetigkeitsgründen die Amplitude keinen großen Wert mehr annimmt. Man darf daher eine rasche Konvergenz der Werte für den Zylinder und die Scheibe erwarten, was die Tabelle III auch deutlich zeigt.

Tabelle III  
 $\tau_0$ -Werte für den Zylinder

<i>n</i>	$\sigma = 0$	$\sigma = 0,1$	$\sigma = 0,2$	$\sigma = 0,3$	$\sigma = 0,4$	$\sigma = 0,5$
0 (T)	5,136	5,136	5,136	5,136	5,136	5,136
0 (L)	2,604	2,885	3,294	3,997	5,519	$\infty$
1	2,474	2,583	2,698	2,817	2,937	3,054
2	2,336	2,341	2,344	2,348	2,351	2,354

$\tau_0$ -Werte für die Scheibe

<i>n</i>	$\sigma = 0$	$\sigma = 0,1$	$\sigma = 0,2$	$\sigma = 0,3$	$\sigma = 0,4$	$\sigma = 0,5$
0 (T)	5,136	5,136	5,136	5,136	5,136	5,136
0 (L)	2,604	2,855	3,138	3,463	3,851	4,332
1	2,473	2,573	2,659	2,734	2,800	2,857
2	2,336	2,340	2,343	2,345	2,347	2,349

bestimmten Frequenzen die Axialkomponenten verschwinden.

Für  $n=0$  zerfällt Gl. (37) in zwei Faktoren, deren einer für sich gleich Null gesetzt, folgende Gleichung liefert:

$$\Theta_0(\tau_0) = -\tau_0^2/2 \quad \text{oder} \quad \Theta_1(\tau_0) = 2, \tag{38}$$

der andere

$$\Theta_0(\alpha \tau_0) = -\tau_0^2/2 \quad \text{oder} \quad \Theta_1(\alpha \tau_0) = 2 \alpha^2. \tag{39}$$

Gl. (38) beschreibt eine rein azimutale Schwingung,

Diese Resonanzen lassen sich definitionsgemäß in das allgemeine Indizierungsschema einordnen, indem man ihnen die Laufzahl  $q=0$  zuordnet. Dann kann allgemein  $n$  als die Zahl der die Achse enthaltenden Knotenebenen der stationären Amplitudenverteilung einer bestimmten Schwingungskomponente gemessen werden,  $q$  als die Zahl der Knotenebenen senkrecht zur Achse,  $p$  schließlich kann in bestimmten Spezialfällen als Zahl der zur Achse konzentrischen Knotenzylinder bestimmt werden.



Dem Verfasser sei es erlaubt, Herrn Prof. Dr. H. O. KNESER für seine Unterstützung und Förderung dieser Arbeit an dieser Stelle zu danken.

(Eingegangen am 13. Juli 1956.)

#### Schrifttum

- [1] LORD RAYLEIGH, Theorie des Schalles. Braunschweig 1880, S. 266.
- [2] BOYLE, R. W. und SPOULE, D. O., Canad. J. Res. 5 [1931], 601.
- [3] RÖHRICH, E., Z. Phys. 73 [1932], 813.
- [4] SCHOENECK, H., Z. Phys. 92 [1934], 390.
- [5] SHEAR, S. K. und FOCKE, A. B., Phys. Rev. 57 [1940], 532.
- [6] POCHHAMMER, L., Crelles J. Math. 81 [1876], 324.

- [7] SOMMERFELD, A., Vorlesungen über theoretische Physik, Band II. Akad. Verlagsges. Leipzig 1945, S. 102.
- [8] HUDSON, G. E., Phys. Rev. 63 [1943], 46.
- [9] BANCROFT, D., Phys. Rev. 59 [1941], 588.
- [10] DAVIES, R. M., Phil. Transact. (A) 48 [1946], 375.
- [11] HÜTER, T., Z. angew. Phys. 1 [1949], 274.
- [12] HOLDEN, A. N., Bell Syst. tech. J. 3 [1951], 956.
- [13] EDMONDS, P. D. und SITTING, E., Experimentelle Untersuchung der elastischen Eigenschwingungen isotroper Kreiszylinder. Acustica 7 [1957], im Druck.
- [14] AIREY, J. R., Arch. Math. Phys. 20 [1913], 290.
- [15] LOVE, A. E. H. und TIMPE, A., Lehrbuch der Elastizität. B. G. Teubner Verlagsges., Leipzig 1907, S. 656.

## MEASUREMENTS OF THERMAL AND ORDINARY DIFFUSION IN GAS MIXTURES ( $H_2$ -He, $H_2$ -N<sub>2</sub> and $H_2$ -O<sub>2</sub>) BY USING ULTRASONICS

by A. VAN ITTERBEEK and J. NIHOUL

Instituut voor Lage Temperaturen en Technische Physica, Leuven, Belgium

#### Summary

Measurements are carried out on thermal diffusion of  $H_2$ -He,  $H_2$ -N<sub>2</sub> and  $H_2$ -O<sub>2</sub> mixtures whereby the change of the concentration is determined from sound velocity measurements. Using the method formulated by JONES and FURRY, measurements are made on the change of sound velocity caused by the change of concentration as a function of time and from this the mutual diffusion coefficient  $D_{12}$  can be determined for the different mixtures as a function of temperature. A good agreement is obtained with the values calculated from the equations of HIRSCHFELDER.

#### Sommaire

On a mesuré la diffusion thermique de mélanges  $H_2$ -He,  $H_2$ -N<sub>2</sub> et  $H_2$ -O<sub>2</sub>, en déterminant la variation de concentration par des mesures de la vitesse du son. On a mesuré, en fonction du temps, par la méthode de JONES et FURRY, la variation de vitesse du son due à un changement de concentration, ce qui a permis de déterminer le coefficient de diffusion mutuelle  $D_{12}$  pour les différents mélanges, en fonction de la température. On a obtenu un bon accord avec les valeurs calculées à partir des équations de HIRSCHFELDER.

#### Zusammenfassung

Bei Untersuchungen über die Thermodiffusion in Gasgemischen ( $H_2$ -He,  $H_2$ -N<sub>2</sub>,  $H_2$ -O<sub>2</sub>) wurde die Konzentrationsänderung durch Messung der Schallgeschwindigkeit bestimmt. Weiter wurde nach einer von JONES und FURRY angegebenen Methode der gegenseitige Diffusionskoeffizient  $D_{12}$  der verschiedenen Gasgemische als Funktion der Temperatur aus der durch Konzentrationsänderungen verursachten zeitlichen Änderung der Schallgeschwindigkeit ermittelt. Man erhält eine gute Übereinstimmung mit den aus HIRSCHFELDERS Gleichungen berechneten Werten.

#### 1. Introduction

A year ago we published [1] a few experimental data on thermal diffusion measurements in  $H_2$ -He gas mixtures using ultrasonics. We described at that time the experimental technique, which consists in measuring the velocity of sound with an acoustical interferometer. These velocity measurements are used to determine the concentration of the components of the gas mixtures and also the change of concentration produced under the influence of thermal

diffusion. Other investigators like IBBS and GREW [2] make use of heat conductivity measurements to determine the change of concentration.

In our previous paper we showed the possibility of separating with our experimental method the thermal diffusion coefficient from the ordinary diffusion coefficient. Independently NETTLEY [3] published just before ours a paper on the same subject. The experimental technique consists in measuring the change of the velocity as a function of time, and

to calculate from this the change of the concentration  $\Delta\gamma$  as a function of time  $t$ . Corresponding with CLARK JONES and FURRY's [4] theory we have

$$(\Delta\gamma)_t = (\Delta\gamma)_{t=\infty} (1 - e^{-t/\tau}). \quad (1)$$

The relaxation time  $\tau = C/D_{12}$ ;  $C$  being a constant (see further), which can be calculated from the dimensions of the apparatus used and from the known experimental conditions. We have carried out measurements on the mixtures  $H_2-N_2$ ,  $H_2-O_2$ ,  $H_2-He$ , from which we calculated the ordinary diffusion coefficient  $D_{12}$  for the mixtures in question and compared the experimental results with the values calculated from the equations given by HIRSCHFELDER [5].

## 2. Experimental apparatus and method

In order to check the theory of JONES and FURRY a new apparatus was built. The apparatus is conceived in such a manner that the conditions mentioned in the theory are approached as closely as possible.

In our previous apparatus the connecting tube between the cold volume (temperature  $T_2$ ; boiling point of liquid oxygen or hydrogen) and the volume

at room temperature  $T_1$  was not well defined. This was also the case for the ratio between the two volumes. In our previous experiments the velocity of sound was also measured in the cold volume  $V_2$ . However to determine the exact concentration we had some difficulty, because the velocity becomes a function of pressure at low temperatures. On the present apparatus the velocity is measured at room temperature. The apparatus (Fig. 1) is constructed of brass. It consists of two parts:  $V_1$  and  $V_2$ ,  $V_1$  contains a quartz crystal with a large diameter 5 cm, to have a great sensitivity.

The frequency of the quartz crystal ( $\pm 600$  kc/s) is determined at each velocity measurement by means of a precision frequency meter. a is a tube in german silver which connects the two volumes  $V_1$  and  $V_2$  (total length: 305 mm, inner diameter 3.9 mm). The other dimensions are indicated on the figure. The ratio  $V_1/V_2$  calculated from the dimensions is equal to 0.62.

After the apparatus has been evacuated and filled with hydrogen gas so that the different parts reach the desired temperature, the apparatus is evacuated again and filled with the mixture to be studied.

The technique consists further in measuring the change of the velocity of sound in the mixture as a function of time at intervals of 10 minutes. From the curves obtained we calculate the instantaneous change of the concentration  $\Delta\gamma$  in the volume  $V_1$ .

We used the equation

$$W^2 = \frac{c_p^{(1)} \gamma_1 + c_p^{(2)} (1 - \gamma_1)}{c_v^{(1)} \gamma_1 + c_v^{(2)} (1 - \gamma_1)} \frac{R_M T}{M_1 \gamma_1 + M_2 (1 - \gamma_1)} \quad (2)$$

in which the symbols have their ordinary significance. The total change of the concentration is obtained from

$$\Delta\gamma = \Delta\gamma_1 + \Delta\gamma_2.$$

$\Delta\gamma_2$  being the change of the concentration in the cold volume;  $\Delta\gamma_2$  is calculated from  $\Delta\gamma$ , by means of the equation

$$\Delta\gamma_2 = \Delta\gamma_1 \frac{V_1}{V_2} \cdot \frac{T_2}{T_1} = \Delta\gamma_1 \cdot 0.62 \cdot \frac{T_2}{T_1}$$

or

$$\Delta\gamma = k \Delta\gamma_1.$$

In our experiments the values of  $k$  used are:

$$T_1 = 290^\circ \text{K}, \quad T_2 = 90^\circ \text{K}, \quad k = 1.16;$$

$$T_1 = 290^\circ \text{K}, \quad T_2 = 77^\circ \text{K}, \quad k = 1.14;$$

$$T_1 = 290^\circ \text{K}, \quad T_2 = 20^\circ \text{K}, \quad k = 1.04.$$

So finally graphs are drawn for  $\Delta\gamma$  as a function of time. To these graphs we applied the equation (1) and calculated the relaxation time  $\tau$ . According to JONES and FURRY's theory the relaxation time  $\tau$  can be written

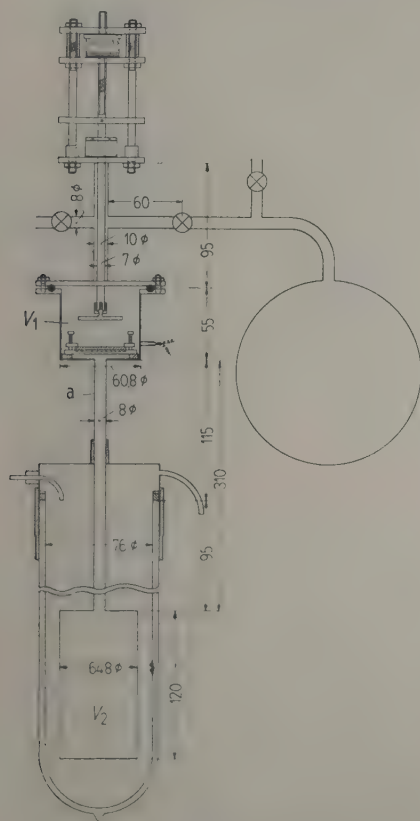


Fig. 1. Diagram of apparatus.



$$\tau = \frac{N_1 N_2}{N_1 + N_2} \frac{L}{n D_{12}} \frac{T_2}{S \Delta T} \ln \frac{T_1}{T_2} \quad (3)$$

$N_1$  and  $N_2$  being the number of molecules effectively in the volumes  $V_1$  and  $V_2$ ,  $n$  the molecular density in the volume  $V_2$ . Equation (3) can also be written

$$\tau = \frac{V_1 V_2}{T_1} \left( \frac{V_1}{T_1} + \frac{V_2}{T_2} \right)^{-1} \frac{L}{D_{12}} \frac{T_2}{S \Delta T} \ln \frac{T_1}{T_2}; \quad (4)$$

$\Delta T = T_1 - T_2$ ;  $L$  is the length of the connection tube,  $S$  its cross-section.

From the values obtained for  $\tau$  and using equation (3), the coefficient  $D_{12}$  corresponding to the average temperature can be calculated

$$T = \frac{T_1 T_2}{T_2 + T_1} \ln \frac{T_2}{T_1}.$$

The measurements were carried out with two different cross-sections of connecting tube, but there was a complete agreement.

### 3. Experimental results

#### 3.1. H<sub>2</sub>-He mixtures

The measurements are carried out for mixtures with concentrations of approximately 50%, for the reason that for those mixtures the thermal diffusion effect is largest.

In Table I are given the experimental results together with the change of the concentration calculated from the measurements.

Measurements were also carried out for the same mixture but with  $T_2 = 17.1^\circ \text{K}$  for which we obtained for  $\tau$  (1 atm)  $= 9.52 \times 10^3$  s.

In Fig. 2 are represented as an example the measurements corresponding to the fourth series of measurements.

In Fig. 2 three curves are brought together: curve 1 represents the change of  $\bar{W}$  as a function of  $t$ , curve 2 represents  $\gamma$  or  $\Delta\gamma$  as a function of  $t$ , and finally curve 3 gives  $-\ln[1 - (\Delta\gamma/\Delta\gamma_\infty)]$  as a function of  $t$ . From Fig. 2 we see that curve 3 is a straight line, which agrees with JONES and FURRY's theory.

#### 3.2. H<sub>2</sub>-O<sub>2</sub> and H<sub>2</sub>-N<sub>2</sub> mixtures

The same kind of measurements were also carried out on mixtures H<sub>2</sub>-O<sub>2</sub> and H<sub>2</sub>-N<sub>2</sub>. The results of those measurements are given in Table II.

In Fig. 3 we have graphically drawn the values of  $-\ln[1 - (\Delta\gamma/\Delta\gamma_\infty)]$  for the H<sub>2</sub>-N<sub>2</sub> mixtures as a function of  $t$ . We see that again straight lines are obtained. The same is the case for the H<sub>2</sub>-O<sub>2</sub> mixtures.

Table I  
Thermal diffusion in H<sub>2</sub>-He mixtures

(a)  $\gamma_0 = 51.0\%$  He;  $T_1 = 291^\circ \text{K}$ ,  $T_2 = 90^\circ \text{K}$ ;  
 $T = 153^\circ \text{K}$ ;  $p = 32.2$  cm; frequency 605.00 kc/s

$t$ min	$\bar{W}$ m/s	$t$ min	$\Delta\gamma$ %	$-\ln\left(1 - \frac{\Delta\gamma}{\Delta\gamma_\infty}\right)$	$\tau \cdot 10^{-3}$ s (32.2 cm)	$\tau \cdot 10^{-3}$ s (1 atm)
0	1097.5	20	1.62	0.428	3.54	8.36
6	1098.7	30	1.85	0.509		
13	1099.5	40	2.32	0.691		
20	1101.0	50	2.75	0.875		
27	1101.2	60	3.07	1.087		
38	1102.4	70	3.40	1.21		
		$\infty$	4.64			
134	1107.7					
193	1108.3					
226	1108.4					

(b)  $\gamma_0 = 54.5\%$  He;  $T_1 = 290^\circ \text{K}$ ,  $T_2 = 77.3^\circ \text{K}$ ;  
 $T = 137^\circ \text{K}$ ;  $p = 43.7$  cm; frequency 605.00 kc/s

$t$ min	$\bar{W}$ m/s	$t$ min	$\Delta\gamma$ %	$-\ln\left(1 - \frac{\Delta\gamma}{\Delta\gamma_\infty}\right)$	$\tau \cdot 10^{-3}$ s (43.9 cm)	$\tau \cdot 10^{-3}$ s (1 atm)
0	1085.5	20	0.99	0.230	5.08	8.84
6	1086.6	40	1.72	0.456		
14	1086.9	60	2.30	0.672		
27	1088.5	80	2.85	0.932		
41	1090.0	100	3.28	1.197		
61	1092.2	$\infty$	4.7			
99	1093.5					
230	1096.4					
253	1096.6					
300	1096.8					

(c)  $\gamma_0 = 37.6\%$  He;  $T_1 = 291^\circ \text{K}$ ,  $T_2 = 77.3^\circ \text{K}$ ;  
 $T = 137^\circ \text{K}$ ;  $p = 52.0$  cm; frequency 604.72 kc/s

$t$ min	$\bar{W}$ m/s	$t$ min	$\Delta\gamma$ %	$-\ln\left(1 - \frac{\Delta\gamma}{\Delta\gamma_\infty}\right)$	$\tau \cdot 10^{-3}$ s (52.0 cm)	$\tau \cdot 10^{-3}$ s (1 atm)
6	1137.9	20	0.78	0.200	6.00	8.77
22	1139.2	40	1.42	0.401		
40	1141.4	60	1.92	0.614		
62	1143.0	80	2.36	0.796		
97	1144.6	100	2.71	0.995		
138	1147.1	150	3.42	1.586		
280	1149.5	$\infty$	4.3			
360	1150.0					
420	1149.0					

(d)  $\gamma_0 = 55\%$  He;  $T_1 = 289^\circ \text{K}$ ,  $T_2 = 20.3^\circ \text{K}$ ;  
 $T = 58^\circ \text{K}$ ;  $p = 42.7$  cm; frequency 604.80 kc/s

$t$ min	$\bar{W}$ m/s	$t$ min	$\Delta\gamma$ %	$-\ln\left(1 - \frac{\Delta\gamma}{\Delta\gamma_\infty}\right)$	$\tau \cdot 10^{-3}$ s (42.7 cm)	$\tau \cdot 10^{-3}$ s (1 atm)
0	1082.6	20	2.29	0.263	—	9.48
6	1084.9	40	3.80	0.484		
17	1086.4	60	4.97	0.697		
31	1090.2	80	5.94	0.916		
51	1093.8	100	6.72	1.136		
78	1097.7	150	8.07	1.688		
111	1100.7	$\infty$	9.9			
128	1101.9					
271	1107.8					
350	1108.1					
402	1108.6					

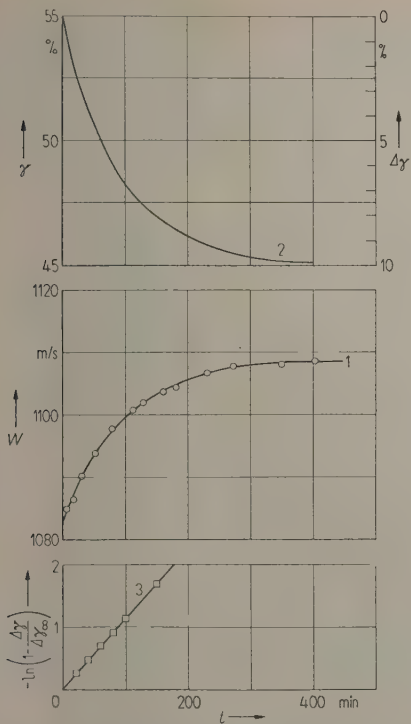


Fig. 2. Thermal diffusion in  $H_2$ -He mixtures ( $T_2=20^\circ K$ ,  $\gamma_0=55\%$  He).

Table II  
Thermal diffusion in  $H_2$ - $O_2$  and  $H_2$ - $N_2$  mixtures  
(a)  $H_2$ - $O_2$ ;  $\gamma_0=53.2\%$   $O_2$ ;  $T_1=291^\circ K$ ,  $T_2=90.1^\circ K$ ;  
 $T=153^\circ K$ ;  $p=19.2$  cm; frequency 604.80 kc/s

$t$ min	$W$ m/s	$t$ min	$\Delta\gamma$ %	$-\ln\left(1-\frac{\Delta\gamma}{\Delta\gamma_\infty}\right)$	$\tau \cdot 10^{-3}$ s (19.2 cm)	$\tau \cdot 10^{-3}$ s (1 atm)
5	434.5	20	2.03	0.341		
17	437.8	40	3.25	0.622		
29	440.4	60	4.13	0.887		
47	443.7	80	4.51	1.155		
65	445.7	100	5.34	1.448		
81	448.5	120	5.74	1.704		
157	451.5	$\infty$	5.9		4.14	16.38
190	453.0					

(b)  $H_2$ - $O_2$ ;  $\gamma_0=62.1\%$   $O_2$ ;  $T_1=290^\circ K$ ,  $T_2=80.1^\circ K$ ;  
 $T=142^\circ K$ ;  $p=15.5$  cm; frequency 604.77 kc/s

$t$ min	$W$ m/s	$t$ min	$\Delta\gamma$ %	$-\ln\left(1-\frac{\Delta\gamma}{\Delta\gamma_\infty}\right)$	$\tau \cdot 10^{-3}$ s (15.5 cm)	$\tau \cdot 10^{-3}$ s (1 atm)
7	407.6	40	2.48	0.665		
22	408.5	60	3.16	0.965		
34	411.0	80	3.72	1.306		
57	412.1	110	4.07	1.600		
78	413.7	$\infty$	5.1		3.72	18.20
110	416.4					
195	417.5					
210	418.4					

(c)  $H_2$ - $N_2$ ;  $\gamma_0=51.6\%$   $N_2$ ;  $T_1=291.5^\circ K$ ,  $T_2=90^\circ K$ ;  
 $T=153^\circ K$ ;  $p=24.4$  cm; frequency 608.55 kc/s

$t$ min	$W$ m/s	$t$ min	$\Delta\gamma$ %	$-\ln\left(1-\frac{\Delta\gamma}{\Delta\gamma_\infty}\right)$	$\tau \cdot 10^{-3}$ s (24.4 cm)	$\tau \cdot 10^{-3}$ s (1 atm)
9	472.2	20	1.42	0.311		
20	476.4	60	2.77	0.738		
34	478.2	100	3.60	1.139		
47	479.2	150	4.25	1.619		
64	481.8	200	4.70	2.180		
94	484.2	$\infty$	6.28		5.46	17.01
113	486.2					
303	492.7					
357	492.7					
400	492.9					

(d)  $H_2$ - $N_2$ ;  $\gamma_0=51.0\%$   $N_2$ ;  $T_1=288.2^\circ K$ ,  $T_2=90^\circ K$ ;  
 $T=153^\circ K$ ;  $p=53.3$  cm; frequency 608.59 kc/s

$t$ min	$W$ m/s	$t$ min	$\Delta\gamma$ %	$-\ln\left(1-\frac{\Delta\gamma}{\Delta\gamma_\infty}\right)$	$\tau \cdot 10^{-3}$ s (53.3 cm)	$\tau \cdot 10^{-3}$ s (1 atm)
8	469.3	100	2.62	0.511		
27	472.5	200	4.03	0.946		
62	475.8	300	5.21	1.570		
90	477.9	400	5.70	2.010		
116	478.9	$\infty$	6.58		11.82	16.85
570	492.2					
486	493.2					
600	493.2					

(e)  $H_2$ - $N_2$ ;  $\gamma_0=53.5\%$   $N_2$ ;  $T_1=292^\circ K$ ,  $T_2=90^\circ K$ ;  
 $T=153^\circ K$ ;  $p=28.0$  cm; frequency 604.80 kc/s

$t$ min	$W$ m/s	$t$ min	$\Delta\gamma$ %	$-\ln\left(1-\frac{\Delta\gamma}{\Delta\gamma_\infty}\right)$	$\tau \cdot 10^{-3}$ s (28 cm)	$\tau \cdot 10^{-3}$ s (1 atm)
6	467.7	20	1.15	0.196		
21	466.8	40	2.05	0.382		
39	469.4	60	2.80	0.569		
58	472.0	80	3.45	0.767		
90	476.2	100	4.00	0.967		
123	478.7	150	4.95	1.458		
158	480.6	$\infty$	6.45		6.24	16.94

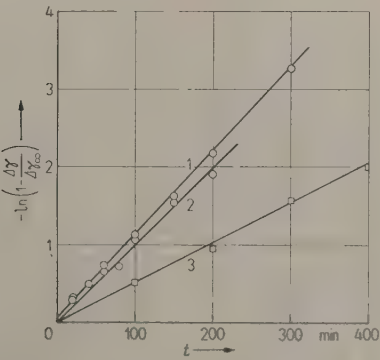


Fig. 3.  $H_2$ - $N_2$  mixtures;  $\gamma_0=\pm 50\%$ ;  
curve 1:  $p=24.4$  cm,  $T_2=90.1^\circ K$ ;  
curve 2:  $p=23.3$  cm,  $T_2=77.3^\circ K$ ;  
curve 3:  $p=53.3$  cm,  $T_2=90.1^\circ K$ .



Using values of the relaxation time  $\tau$  of Tables I and II and equation (2) we calculated the diffusion coefficient  $D_{12}$ . On the other hand we also calculated this coefficient by means of the equations and the empirical data given in HIRSCHFELDER's book [5].

As up to now no direct measurements on diffusion coefficients at low temperatures are known, we can conclude from Table III that this indirect method works fairly well. At the highest temperatures the agreement between the theoretical values

Table III

Mixtures	$T_1$ Room temp.	$\bar{T}$	$\tau \cdot 10^{-3}$	$D_{12}$ exp.	$D_{12}$ theor.
	$T_1$ ° K				
H <sub>2</sub> —He (50%)	90.1	153	8.36	0.421	0.518
	77.3	137	8.84	0.343	0.429
	20.3	58	9.48	0.093	0.098
	17.1	52	9.52	0.076	0.078
H <sub>2</sub> —He (35%)	77.3	137	8.77	0.346	0.429
H <sub>2</sub> —N <sub>2</sub> (50%)	90.1	153	17.0	0.207	0.237
	90.1	153	16.8	0.209	0.237
	90.1	153	16.9	0.208	0.237
	77.3	137	19.6	0.173	0.194
H <sub>2</sub> —O <sub>2</sub> (50%)	90.1	153	16.4	0.215	0.250
H <sub>2</sub> —O <sub>2</sub> (60%)	80.1	142	18.2	0.174	0.218

Thus we used the equation

$$D_{12} = 0.0026280 \frac{VT^3 (M_1 + M_2)/2 M_1 M_2}{p \cdot \sigma_{12}^3 \cdot \Omega_{12}^{(1,1)*} (T_{12}^*)};$$

$D_{12}$  diffusion coefficient in cm<sup>2</sup>/s,

$p$  pressure in atmospheres,

$T$  temperature in °K,

$T_{12} = kT/\varepsilon_{12}$ ,

$M_1, M_2$  molecular weights of species 1 and 2,

$\sigma_{12}, \varepsilon_{12}/k$  molecular potential energy parameters characteristic of the 1-2 interaction in Å and °K respectively,

$\Omega^{(1,1)}$  the well-known integrals for calculating the transport coefficients for the Sutherland potential.

The results obtained are given in Table III.

and the experimental values is not so good as at liquid hydrogen temperatures where the change of the concentration is about twice the change at liquid oxygen temperatures.

We take the opportunity of expressing our thanks to the Belgian Ministry of Education for financial aid during these experiments.

(Received May 3rd, 1956.)

#### References

- [1] VAN ITTERBEEK, A. and NIHOUL, J., *Acustica* 5 [1955], 142.
- [2] IBBS, T. L. and GREW, K. E.
- [3] NETTLEY, P. T., *Proc. Phys. Soc. (B)* 67 [1954], 753.
- [4] CLARK JONES, R. and FURRY, W. H., *Rev. mod. Phys.* 18 [1946], 1951.
- [5] HIRSCHFELDER, I. O.

# MUSIKINSTRUMENTENSTIMMUNGEN UND TONSYSTEME

Beispiele: Klavier, Flügel, Akkordeon, Harmonium, Streichinstrumente

VON H. MEINEL

Forschungsinstitut für Musikinstrumentenbau des Deutschen Amtes für Material- und Warenprüfung, Zwota über Klingenthal/Sachsen

## Zusammenfassung

Die Stimmung von Klavieren und Flügeln einerseits, Akkordeons und Harmoniums andererseits, entspricht verschiedenen temperierten Tonsystemen. Für die letzteren gilt das bisher als allein herrschend angesehene System der Einteilung der Oktave mit dem Frequenzverhältnis  $1:2$  in 12 Halbtöne der Größe  $\sqrt[12]{2}$ . Für gut gestimmte Klaviere und Flügel wird jedoch in der Praxis eine Temperierung mit um etwa 3 cent pro Oktave erweiterten Intervallen benützt, Halbtongröße  $\sqrt[12]{2,0017}$ . Gutgestimmte Klaviere und Flügel weisen deshalb nicht temperierte, sondern annähernd reine (natürlich-harmonische) Quinten auf. Da auch Streichinstrumente in reinen Quinten gestimmt werden, ergeben sich für Klaviere und Flügel einerseits, Streichinstrumente (Geigen, Bratschen, Celli) andererseits gleichlaufende Stimmungskurven. Ursachen und Bedeutung dieser Übereinstimmung und technische Anwendungsmöglichkeiten der Stimmungskurven werden besprochen.

## Summary

The use of differently tempered scales for pianos and accordions or harmoniums must be accepted. In the latter the octave is divided into 12 semitones of value  $2^{1/12}$  but in the former the practice uses octaves 3 cents wider, making the semitone  $2.0017^{1/12}$  so that the fifths are almost pure untempered. As bowed-string instruments also have pure fifths they and the piano have similar tuning curves. The causes and results of this agreement are discussed as well as its technical possibilities.

## Sommaire

L'emploi de différents modes tempérés pour les pianos droits et à queue d'une part, les accordéons et les harmoniums d'autre part, doit être considéré comme bien établi. Dans le cas de ces derniers instruments, on utilise le système considéré jusqu'à présent comme unique, dans lequel l'octave est partagée dans le rapport de fréquences  $1:2$  en 12 demitons de valeur  $\sqrt[12]{2}$ . Dans le cas des pianos droits et à queue bien accordés, cependant, on utilise en pratique un tempérament avec intervalles élargis d'environ 3 cents par octave: valeur du demi-ton  $\sqrt[12]{2,0017}$ . Les pianos droits et à queue bien accordés présentent donc des quintes non tempérées mais à peu près pures (harmoniquement naturelles). Comme les instruments à cordes sont aussi accordés par quintes pures, les pianos droits et à queue d'une part, les instruments à cordes d'autre part (violons, altos, violoncelles) ont des courbes d'accord analogues. On indique les causes et signification de cette concordance, ainsi que les possibilités techniques d'utilisation de ces courbes d'accord.

## 1. Klavierstimmung und Tonsysteme

Seitdem es möglich ist, Frequenzen relativ schnell und genau zu messen, wurde aus verschiedenen wichtigen Gründen versucht, über Klavierstimmungen, insbesondere über die beste Klavierstimmung, Klarheit zu gewinnen. Gearbeitet haben darüber GRÜTZMACHER und LOTTERMOSER [1], O. L. RAILSBACK [2], R. W. YOUNG [3], D. W. STAUFFER [4], H. MEINEL [5]. Um gute Vergleichsmöglichkeiten auch mit unseren Ergebnissen zu haben, wurden Kurven aus den Arbeiten der obengenannten Autoren in einheitlichem Maßstab in Abb. 1 wiedergegeben und unserer Darstellungsweise angeglichen. Aus der Arbeit von GRÜTZMACHER und LOTTERMOSER wurde dabei, unserer Zielsetzung entsprechend, nur

die beste der dort gezeigten drei Stimmungen ausgewählt, die jedoch noch nicht wirklich gut ist. YOUNG weist selbst darauf hin, daß die von ihm veröffentlichte Kurve nur die Steigung der eigentlichen Stimmungskurve darstellt, nicht die Stimmung selbst. STAUFFER bringt eine Kurve, die von zwei Klavieren stammt, ohne daß nähere Angaben über die Gewinnung gemacht werden. Sie weisen je Taste nur einen Meßwert auf und lassen die Güte der Stimmung nicht genügend beurteilen. Sie muß erkennbar sein, will man sich ein Bild über die besten Klavierstimmungen machen. So sind wir zu Vergleichszwecken im wesentlichen auf die Kurve von RAILSBACK angewiesen, werden aber die anderen nicht vernachlässigen. Wir selbst haben aus dem Prüfbetrieb der letzten Jahre umfangreiches Mate-





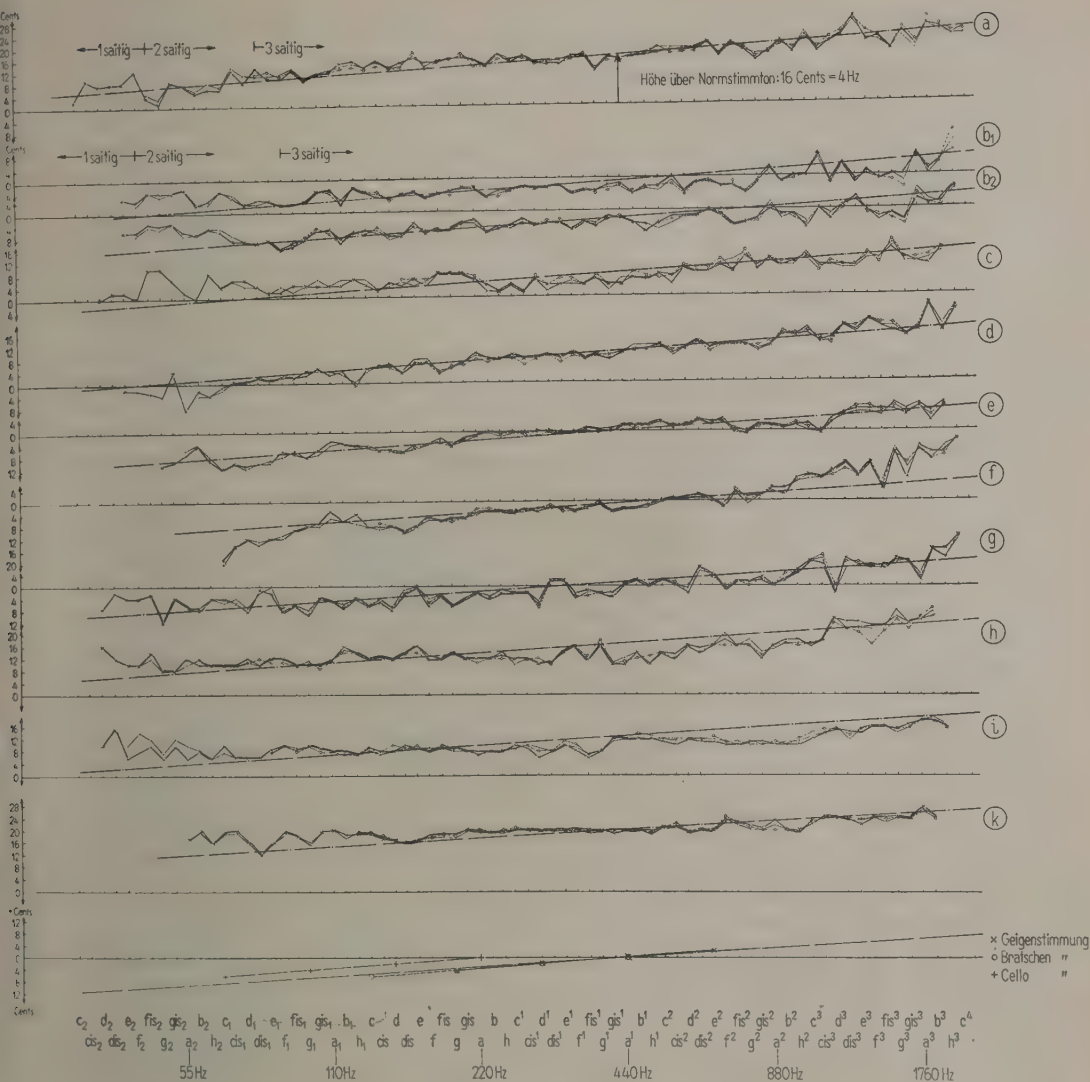


Abb. 2. Gute Klavier- und Flügelstimmungen eigener Messung. Instrumente der Firmen C. Bechstein, Berlin; Julius Blüthner, Leipzig; VEB Pianofortefabrik Eisenberg/Thür.; August Förster, Löbau; Grotian-Steinweg, Braunschweig; Sächs. Pianofortefabrik VEB Seifhennersdorf L.; Steinway & sons, Hamburg. Die Reihenfolge der Kurven stimmt nicht mit der Reihenfolge der Firmen überein. Weitere Stimmungskurven, auch von schlecht gestimmten Instrumenten, unter [5].

der Stimmungsmittellinie — bei  $a^1$  von 440 Hz als Abweichung vom Normstimmton (vgl. Abb. 2 a). So entsprechen z. B. die Stimmungen in Abb. 2 b, 2 e, 2 f, 2 g der Normung  $a^1 = 440$  Hz.

Die Beurteilung der Güte der von uns gemessenen Stimmungen fußte ursprünglich auf der musikalisch-künstlerischen Beurteilung seitens unserer Gutachterausschüsse. Später konnte sie sich auf die physikalischen Meßergebnisse allein stützen. Es hatte sich z. B. oft gezeigt: Gehören zu einer Taste mehrere

Saiten und fallen die davon herrührenden Frequenzmeßwerte nicht zusammen (Toleranz größer als etwa 2 cent), so wird der Klang dieser Taste, durch Schwebungen bedingt, nicht als ruhig empfunden, er „quirlt“, „flackert“, „wimmert“ oder wie man es sonst nennen mag, genügte jedenfalls nicht den künstlerischen Ansprüchen unserer Gutachterausschüsse. Die musikalische Bedeutung der physikalischen Meßergebnisse der Frequenzunterschiede zwischen den verschiedenen Saiten einer Taste, die



Güte der Stimmung in dieser Richtung, entspricht etwa der Größe dieser Unterschiede. Am besten ist nach den uns vorliegenden Urteilen eine völlige Übereinstimmung der Saitenfrequenzen. Für die musikalische Bedeutung der Unterschiede liegt jedoch eine Art Schwellwert von etwa 1 cent vor. Noch geringere Unterschiede zwischen den Frequenzen der Saiten einer Taste bringen keinen bemerkenswerten musikalischen Gewinn mehr. Werden die Unterschiede größer als etwa 2 cent, beginnen sie unangenehm zu wirken.

Anfangs waren wir wegen verschiedener Hinweise in der Literatur und auf Grund von Behauptungen mancher Stimmer unsicher in der Beantwortung der Frage, ob die beste Klavierstimmung tatsächlich möglichst genau temperiert sein soll, oder ob nicht doch gewisse Abweichungen von der temperierten Stimmung zweckmäßig sind, etwa in Richtung einer mitteltönigen Stimmung, d. h. der Bevorzugung gewisser öfters benützter Tonarten, vgl. [1]. Wir verwendeten eine beachtliche Zeit darauf, in unseren Klavier- und Flügel-Stimmungskurven, die manchmal erhebliche Abweichungen von einer temperierten Stimmung zeigen, vernünftige Gesetzmäßigkeiten und schließlich solche irgendwelcher Art außerhalb einer Temperierung zu entdecken (vgl. auch [1]. Die Prüfung unseres gesamten Materials, insbesondere auch der jeweils von einem Stimmer vorliegenden verschiedenen Stimmungen und unsere mit zahlreichen guten Stimmern durchgeführten Versuche, zeigte jedoch in keinem Fall gewollte und daher wenigstens bei demselben Stimmer immer wieder vorkommende Abweichungen gegenüber einer temperierten in Richtung einer mitteltönigen Stimmung. Fast zwangsläufig weisen übrigens die gut temperierten Stimmungen auch geringste Unterschiede innerhalb eines Chores auf.

Betrachten wir die Stimmungskurven in ihrem Verlauf von Klang zu Klang, so sehen wir vor allem einen Anstieg von links nach rechts, vgl. Abb. 1 und Abb. 2, wobei die Kurven für die künstlerisch am besten beurteilten Stimmungen weitgehend eine Gerade darstellen. Die Halbtöne sind also etwas größer, als einem Faktor  $\sqrt[12]{2}$  entspricht und die Gerade selbst zeigt, daß eine Temperierung vorliegt. Die bei der Temperierung von unseren besten Stimmern gezeigte Leistung (Abweichungen im allgemeinen  $\leq \pm \frac{1}{2}$  cent) ist überraschend hoch [5]. Manchmal nähert sich die Stimmung in den mittleren Oktaven einer waagerechten Geraden (Abb. 1 a bis d, Abb. 2 h bis k), manchmal finden wir, daß bei den tiefen Klängen die Stimmung weniger absinkt, bei hohen weniger steigt als der schrägen Geraden entspricht (Abb. 2 b, c), manchmal ist es umgekehrt (Abb. 1 c, d, Abb. 2 f). Aber das sind

Effekte (zweiter Ordnung), die bei unseren Betrachtungen keine Rolle spielen, noch dazu, da wir sie bei unseren zahlreichen Messungen nicht als typisch feststellen konnten. Vom Stimmer werden sie beim Spielen von besonders für die Temperierung geeigneten Akkorden gehört, kaum beim Spiel von Klaviermusik. Typisch ist dagegen das allgemein festzustellende Steigen der Stimmungskurve<sup>1</sup>.

Es bedeutet, daß neben der bisher allgemein als allein herrschend angesehenen Werkmeister-Temperierung bei einem unserer bedeutsamsten Instrumente, dem Klavier oder Flügel, eine andere Temperierung besteht. Diese offenbar auf praktische Bedürfnisse zurückgehende neue Temperierung vergrößert sogar das Frequenzverhältnis der Oktave, des konservativsten Intervalls, das sowohl im pythagoreischen und natürlich-harmonischen als auch im bisherigen temperierten Tonsystem 1:2 beträgt. Zwangsläufig erhebt sich hier die Frage, ob auch andere Instrumente diese besondere Art der Temperierung aufweisen.

## 2. Akkordeon- und Harmoniumstimmung und Tonsystem

Wir haben in den letzten Jahren an hunderten, zum wesentlichen Teil ganz hervorragend gestimmten Akkordeons, mehreren Harmoniums und einigen Orgeln, darunter berühmten und von Organisten mit Weltruf benützten, die Stimmung gemessen. In keinem einzigen Falle haben wir bei diesen Instrumenten eine ansteigende (oder fallende) Stimmungsgerade gefunden, sondern immer nur die mehr oder minder geglückte Angleichung an die waagerechte Gerade unserer Darstellung, an die Werkmeister-Temperierung. Die Abb. 3 zeigt ein Beispiel einer guten Akkordeon- und Harmoniumstimmung (Akkordeonstimmungen verschiedener Güte unter [5]). An unseren Stimmungskurven von Klavieren finden wir dagegen nur ausnahmsweise d. h. in etwa 5 bis 10% aller gemessenen Stimmungen, eine waagerecht liegende Kurve. Bei derart umfassendem Material und solchen Ergebnissen darf man die Benützung verschiedener temperierter Tonsysteme bei Klavieren und Flügeln einerseits, Akkordeons und Harmoniums andererseits als feststehend ansehen.

<sup>1</sup> Die dieser Arbeit zugrunde liegenden Klavierstimmungen gehen auf verschiedene Methoden des Klavierstimmens zurück, und darauf sind im wesentlichen die oben erwähnten Unterschiede in der Stimmung, als Effekte zweiter Ordnung bezeichnet, zurückzuführen. Über die Richtigkeit dieser oder jener Stimmethode gibt es Meinungsverschiedenheiten. Auf Grund der vorliegenden Ergebnisse dürften sie sich, von der Praxis aus gesehen, als unbegründet erweisen.



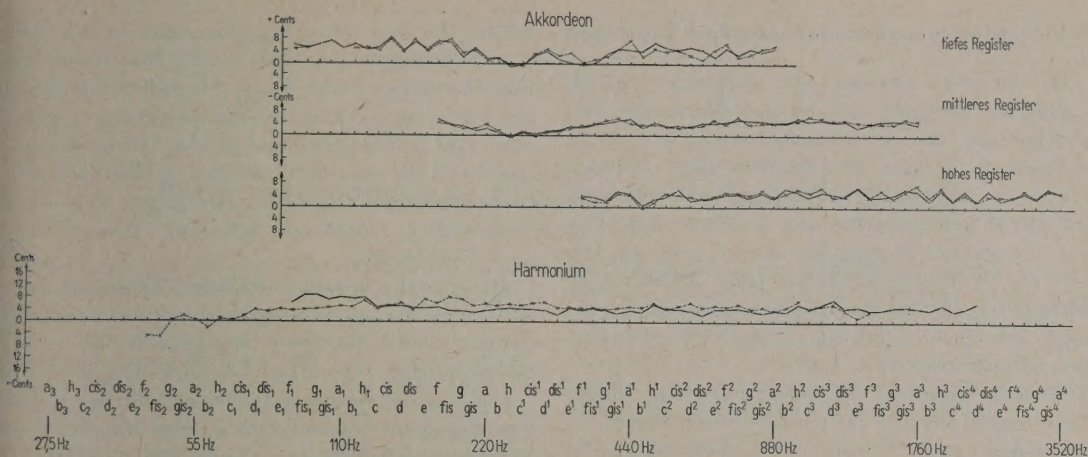


Abb. 3. Beispiel guter Akkordeon- und Harmoniumstimmung.

### 3. Ursachen der Benützung verschiedener temperierter Tonsysteme

Unter den geschilderten Umständen muß eine bestimmte Ursache für die verschiedenen Stimmungsarten der erwähnten Musikinstrumente vorliegen.

Wir prüften die Meinung vieler Klavierstimmer und mancher Pianisten, nach der die erweiterten Intervalle dem Klang eine größere Brillanz verleihen, selbst nach, und kamen zu gleicher Auffassung. Eine solche Wirkung liegt außerdem im Zuge der Entwicklung des Klavierklanges in den letzten 200 Jahren. Etwa seit der Zeit Mozarts wurde die Erhöhung der Kraft und Brillanz des Klavierklanges u. a. durch Erhöhung der Saitenspannung technisch in starkem Maße verwirklicht und ist durch einen Vergleich von originalgetreu besaiteten Klavieren aus der Zeit Mozarts mit heutigen deutlich zu hören, z. B. im Deutschen Museum in München. Der Wunsch nach größerer Brillanz dürfte aber nicht als alleinige Ursache für die erweiterten Intervalle anzusehen sein, wahrscheinlich nicht einmal als die wichtigste; denn die mit der angegebenen Erweiterung der Intervalle verbundene Erhöhung der Brillanz ist subjektiv nicht sehr bedeutsam. Dem heutigen Klavierbau stünden wirksamere Mittel zur Verfügung.

Um weitere Ursachen zu finden, ließen wir unter gleichklingenden Akkordeons einige mit erweiterten Intervallen stimmen und die musikalische Wirkung durch Sachverständigengremien beurteilen. Die Erhöhung der Brillanz wurde auch beim Akkordeon festgestellt und zwar auch hier als nicht sehr beachtlich, wenn auch hörbar. Die Sachverständigen kamen jedoch nicht zu einer allgemein positiven Einstellung gegenüber der Anwendung der besten Klavierstimmung für das Akkordeon, sondern mehrere gaben der Werckmeister-Temperierung den Vorzug.

Das mag darin begründet liegen — was für Harmonium und Orgel wenigstens teilweise ebenfalls gelten könnte —, daß diese Instrumente Zungenstimmen mit ihrem starken Gehalt an hohen Teiltönen besitzen und eine Erhöhung der Brillanz daher gar nicht brauchen. Außerdem scheint es bei länger andauernden Klängen und Akkorden — die auf Akkordeon, Harmonium und Orgel im Gegensatz zum Klavier möglich sind — so zu sein, daß sich bei ansteigender Stimmungsgeraden Schwebungen und Rauigkeiten des Klanges unangenehm bemerkbar machen. Sie lassen sich durch das Auftreten zusätzlicher Interferenzen zwischen Teiltönen, besonders Oktaven, als Folge der steigenden Stimmungsgeraden erklären. Damit sind die auffälligen Unterschiede in der Lage der Stimmungsgeraden zwischen Klavieren einerseits, Akkordeons, Harmoniums und Orgeln andererseits in ihren Ursachen einigermaßen verständlich. Eine quantitative Betrachtung der Steigung der Stimmungsgeraden führt weiter.

Die Steigung der Stimmung der besten Klaviere beträgt ungefähr 3 cents pro Oktave (siehe dazu die vergleichsweise in den Abb. 1 und 2 eingezeichneten schrägen Geraden, die alle eine Steigung von 3 cents pro Oktave aufweisen). Diese Steigung bedeutet, daß die Oktaven um 3 cents größer sind als 1 : 2, also  $= 1 : 2.001735$ , daß die Halbtonerweiterung  $\frac{3}{12}$  cent beträgt und die Erweiterung einer Quinte (7 Halbtöne)  $\frac{21}{12}$  cents, also fast 2 cents ausmacht. Da die reine (natürlich-harmonische) Quinte mit dem Frequenzverhältnis 2 : 3 auch um 2 cents größer ist als die nach Werckmeister temperierte, bedeutet das, daß bei der hervorragenden Klavierstimmung die temperierten Intervalle so erweitert werden, daß aus den temperierten Quinten praktisch reine Quinten werden.



#### 4. Streichinstrumentenstimmung und Tonsystem

Die Streicher bemühen sich nach ihrer vielfach geäußerten Meinung und unseren Messungen fast ausnahmslos, ihre Instrumente möglichst rein zu stimmen, d. h. ihren Instrumenten reine Quinten, Frequenzverhältnis 2 : 3, zu geben<sup>2</sup>. Damit besitzen die Stimmungskurven von Klavieren bzw. Flügeln die gleiche Steigung von etwa 3 cents pro Oktave wie die von Streichinstrumenten<sup>3</sup>. Das ist beachtenswert, da Streichinstrumente praktisch die einzigen Instrumente sind, mit denen Klaviere zusammen gespielt werden.

Weitere Ursachen der Übereinstimmung liegen darin begründet, daß das pythagoreische System — eine Folge reiner Quinten — melodisch bedingt ist und nach bisherigen Erfahrungen [6] Musiker (Streicher) bei Melodien eine der pythagoreischen angenäherte Stimmung bevorzugen. Auch bei ersten Versuchen mit geblasener Melodie waren die Intervalle gegenüber der üblichen temperierten Stimmung erweitert, so daß sich auch hier Beziehungen zur Klavierstimmung andeuten. Von Sängern hörten wir ähnliches. Ein strenger Nachweis in dieser Richtung nach bereits durchgeführten Messungen mit unserem Stimmgerät erfolgt demnächst von anderer Seite aus. So dürfte die Übereinstimmung zwischen den Stimmungskurven für Klaviere und Streichinstrumente zwar auch auf Stimmungserfahrungen beim Zusammenspiel beruhen, könnte aber sehr wohl allgemeinere Bedeutung haben, hauptsächlich in einem gemeinsamen künstlerischen Emp-

finden, das auch ohne Zusammenspiel zu den gleichen Stimmungsergebnissen für die Instrumente geführt hätte, begründet liegen. Möglicherweise besitzen wir in der auf künstlerische Bedürfnisse gegründeten guten Klavierstimmung eine Temperierung, den Ausdruck eines musikalischen Gefühls, von größerer praktisch-musikalischer Bedeutung, als der an theoretischer Grundlage fußenden Temperierung nach Werckmeister.

Die instrumentenbautechnische Bedeutung der Aufnahme solcher Schwingungskurven sei kurz zusammengefaßt: Sie geben ein genaues, allein auf meßtechnischer Grundlage fußendes Bild über die Einhaltung des Normstimmtones und die dazu wichtige allgemeine Stimmungshöhe, über die Güte der Stimmung innerhalb eines Chores und von Taste zu Taste, über die Haltbarkeit der Stimmung gegenüber Transport, Temperatur und Spieleinflüssen. Sie zeigen auch Mängel am Instrument selbst; bei Klavieren und Flügeln: zu schwache Rast, ungenügend stabiler Eisenrahmen, zu locker sitzende Wirbel und anderes. Bei Akkordeons und Harmoniums geben sie u. a. Aufschluß über die Güte der Nietung der Stimmzungen, über Alterungserscheinungen und andere Einflüsse auf die Stimmung. Nicht ganz unerwähnt mag bleiben, daß manche Stimmer über ihre Leistungen eigene, nicht immer zutreffende Meinungen haben. Auch solche Fälle lassen sich klar und zugunsten der wirklich tüchtigen Stimmer entscheiden. Für Klavierstimmungszwecke allein wird am besten ein Stimmgerät benutzt, das die Erweiterung der temperierten Intervalle um 3 cents pro Oktave bereits berücksichtigt. Ein solches Gerät wurde von uns nach Art des bereits beschriebenen [5] entwickelt.

Für die subjektive Beurteilung der Stimmungen danke ich Frau Prof. ELLY NEX, den Herren GÜNTER KOOTZ, WOLFGANG SCHETELICH, Prof. FRITZ WEITZMANN, den Mitgliedern unseres Prüfungsausschusses Tasteninstrumente: den Herren GERHARD FÖRSTER, FRITZ GEISSLER, MAX KNOPPE, WILLI KRONBERG, PAUL NEUTSCHMANN, WALTER STILLER; für die sorgfältige Durchführung der Messungen meinen Mitarbeitern Fr. ERNA BACHMANN, Herrn KURT HEROLD, Herrn FRITZ KAISER.

(Eingegangen am 1. Juni 1956.)

#### Schrifttum

- [1] GRÜTZMACHER, M. und LOTTERMOSER, W., Phys. Z. 24 [1935], 903—911.
- [2] RAILSBACK, O. L., J. acoust. Soc. Amer. 9 [1937], 37—42.
- [3] YOUNG, R. W., The tuning of musical instruments, Lecture 1953.
- [4] STAUFFER, D. W., Information deficiencies of wind instruments in ensemble. Dissertation Washington 1954.
- [5] MEINEL, H., Acustica 4 [1954], 233—236.
- [6] MEINEL, H., Wiss. Ann. 5 [1956], Heft 7, 568 bis 581; Akademie-Verlag Berlin.

<sup>2</sup> Nur wenn man so stimmt, hat man den Eindruck, daß die Geige wirklich stimmt, jede klangliche Unruhe innerhalb der Quinten deutlich wegfällt. Die Stimmung der Saiten in reinen Quinten bedeutet übrigens, daß nicht etwa die Geige „rein“ gestimmt ist, das würde nur für d-dur gelten, sondern daß sie wegen ihrer aufeinanderfolgenden Quinten pythagoreisch gestimmt ist.

<sup>3</sup> Wenn das Cello-a, wie üblich, mittels einer reinen Oktave auf das Normstimmton-a<sup>1</sup> eingestimmt wird, liegt seine Stimmung gerade um 3 cents gegenüber Violine und Viola höher (vgl. Abb. 21), um 50% mehr, als der Unterschied zwischen reiner und temperierter Quinte beträgt. Das (und ähnliches bei anderen Musikinstrumenten) sollte bei Normvorschriften zum Einstimmen der Musikinstrumente beachtet werden. Auch für die Stimmung im Streichquartett ergeben sich Diskrepanzen, lösbar durch Annahme pythagoreischen Spiels. Doch kann auf dies alles hier nicht eingegangen werden. Hingewiesen sei lediglich noch darauf, daß die „leeren“, d. h. unverkürzt schwingenden Saiten der Streichinstrumente festliegende Orientierungstonhöhen sind, die der Streicher nie wesentlich verläßt (und die auch die Frequenzen der anderen Klänge mit festigen). Spielt er temperiert, spielt er daher zwangsläufig Intervalle, die um etwa 3 cents pro Oktave erweitert sind, spielt also entsprechend der guten Klavierstimmung. Selbst wenn der Streicher nicht temperiert spielt, muß die Berücksichtigung der Stimmung der leeren Saiten seiner Intonation eine ähnliche Tendenz aufdrücken.



## Die Spiralaustastmethode zur Messung stationärer Schalldruckfelder

von G. HÜBNER, Berlin

Abgesehen von wenigen Standardbeispielen ist die Verteilung des Schalldruckes in einem akustischen Feld mit tragbarem Aufwand oft nicht zu berechnen. Aber auch die Möglichkeit, ein solches Schallfeld meßtechnisch zu erfassen, ist heute noch recht unbefriedigend. Man erhält auch hier nur durch eine große Zahl von Messungen und über langwierige Auswertungen den gewünschten Überblick. Das im folgenden angegebene Meßverfahren erlaubt eine schnelle, lückenlose Ausmessung größerer Schallfelder mit gleichzeitiger Registrierung der Meßwerte.

### 1. Verfahren

Ein Mikrofon wird im Schallfeld auf einer Spiralbahn so bewegt, daß der radiale Vorschub pro Umdrehung konstant und gleich der effektiven Mikrofonbreite ist. Dadurch wird eine Kreisfläche lückenlos in einem Zuge ausgetastet, das Schallfeld in einer Schnittebene untersucht. Die dem Schalldruck am Ort des Mikrophons proportionale Mikrofonklemmenspannung wird nach Spannung und Leistung verstärkt und steuert während der Austastung die Helligkeit einer Glühlampe. Die Glühlampe als Registrierorgan wird schließlich synchron zum Mikrofon und im gleichen Sinne wie dieses auf einer verkleinerten Spiralbahn über die photographische Schicht geführt und belichtet diese dabei. Durch die Anordnung erhält man ein Bild

des Schallfeldes, wenn sich die belichteten Spiralen einander anschließen. Durch Einhaltung eines festen Abstandes zwischen Film und Registrierlampe und bei definierten Entwicklungsbedingungen ist das Verfahren quantitativ, man kann durch Photometrieren des Filmes nach einer Eichung den Schalldruck für jeden Meßort des Austastkreises in  $\mu\text{bar}$  angeben.

### 2. Konstruktion, Daten, Schaltelemente

Die Registriereinrichtung und der Endverstärker wurden von dem im Feld befindlichen Austastgerät getrennt. Die Austastung geschieht mit konstanter Winkelgeschwindigkeit. Die hierdurch bedingte, unerwünschte  $1/r$  proportionale, zur Bildmitte hin zunehmende Schwärzung des Bildes kann elektrisch oder optisch bei der Aufnahme korrigiert werden.

Winkelgeschwindigkeit  $\omega$  des Austastflügels:

Wahlweise  $2,62 \text{ s}^{-1}$  entsprechend  $25 \text{ U/min}$   
oder  $0,873 \text{ s}^{-1}$  entsprechend  $8,33 \text{ U/min}$ ;  
Durchmesser des ausgetasteten Kreises  $2,61 \text{ m}$  entsprechend  $5,4 \text{ m}^2$ .

Vorschub des Mikrophons pro Umdrehung:  $2,6 \text{ cm}$ ,  
Dauer für die lückenlose Austastung einer Fläche von  $1 \text{ m}^2$ :  $22 \text{ s}$  bzw.  $67 \text{ s}$ ,

Verkleinerung von Feld zu Originalbild:  $1:13$ ,  
Dynamik bezogen auf die registrierte Schwärzung (bei  $\omega = 0,873 \text{ s}^{-1}$ ):  $65 \text{ dB}$ .

#### Kleinster meßbarer Schalldruck

Der von der Apparatur noch meßbare kleinste Schalldruck ist von der Winkelgeschwindigkeit des Austastflügels abhängig und wurde hier einzig durch die bei der jeweiligen Winkelgeschwindigkeit auftretenden Störerschütterungen des Mikrophons festgelegt. Bei der Ausmessung von Feldern mit Stellen kleineren Schalldrucks muß die Apparatur mit der geringeren Geschwindigkeit betrieben werden. Die weitere Bedingung, daß die Winkelgeschwindigkeit nur so groß sein darf, daß der vom kleinsten Schalldruck bewirkte kleinste Lichtstrom des Registrierorgans noch eine ausreichende Schwärzung ( $0,1$  über dem Schleier) hervorruft, ist allgemein erfüllt. Bei einer Messung von Feldern mit leisesten Stellen von  $50 \text{ dB}$  wird die Apparatur der Störerschütterungen wegen mit der Winkelgeschwindigkeit  $\omega = 0,873 \text{ s}^{-1}$  betrieben, könnte der Schwärzung wegen \* aber 10- bis 15mal so schnell gedreht werden.

\* Die auf Grund der Schwärzungsbedingungen höchstzulässige Winkelgeschwindigkeit bzw. höchstzulässige Drehzahl ( $\nu_{\text{max}}$ ) berechnet sich zu

$$\nu_{\text{max}} = 43,3 E_{\text{min}} \cdot 10^{(n-1)/10} d/R \text{ U/min};$$
  
 $E_{\text{min}}$  kleinste Beleuchtungsstärke der Glühlampe in lux (bei der Zündung),  
 $n/10$  DIN-Empfindlichkeit des Films,  
 $d$  Durchmesser des Lichtflecks,  
 $R$  Radius der größten Registrierspirale.

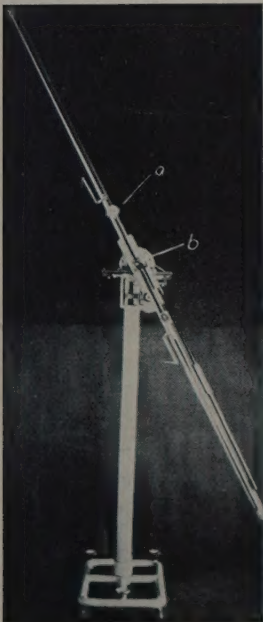


Abb. 1. Das Austastgerät; a Mikrofon, b Verstärker.



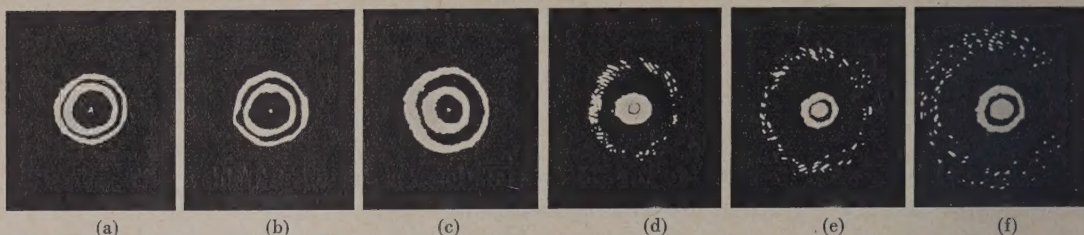


Abb. 2. Parallelschnitte durch das Feld einer Zonenplatte. Abstand der Meßebene von der Zonenplatte bei der Aufnahme: (a) 35 cm, (b) 46 cm, (c) 80 cm, (d) 155 cm, (e) 250 cm, (f) 350 cm. Wellenlänge  $\lambda = 5,3$  cm, Radius der ersten Fresnelzone 25 cm, entsprechend einer Hauptbrennweite von 255 cm.

### Wandlungskanal

Austastgerät: Kristallmikrophon mit der Röhre AC 701 (in der ersten Verstärkerstufe); Vorverstärker mit den Röhren ECC 83 und EF 40; Schleifringe. Registriergerät: Endstufe; Schleifringe; Signalglimmlampe der Firma OSRAM; Röntgen SS-Film.

### 3. Niveaulinienmethode

Die Nachteile der Registrierung bei dem angegebenen Verfahren im Hinblick auf eine quantitative Auswertung sind die genau einzuhaltenden Entwicklungsbedingungen des Films und die Zeitdauer der noch nötigen photometrischen Auswertung. Die Ermittlung der Linien konstanten Schalldrucks, also einer Karte des Feldes, erscheint eine anzustrebende Lösung des Problems, ein stationäres Schalldruckfeld quantitativ zu erfassen. Die gesamte Feldkarte läßt sich in einer Aufnahme ermitteln, wenn man die Spiralaustastung mit einer solchen Spiralregistrierung kombiniert, die auf der photographischen Schicht nur dann Schwärzungspunkte erzeugt, wenn bestimmte Schalldruckwerte — z. B. von 5 zu 5 dB — vom Mikrophon aufgenommen werden. Dadurch werden die Linien konstanten Schalldrucks nach einer vollständigen Austastung punktweise zusammengesetzt.

### 4. Schallfeldmessungen

Ein Beispiel für die Spiralaustastung mit Intensitätsregistrierung ist die Abb. 2 und ein Beispiel für die Spiralaustastung mit Niveaulinienschreibung die Abb. 3. In Abb. 2 wurde das Schallfeld hinter einer akustischen

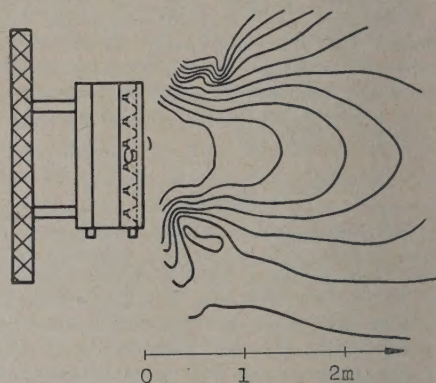


Abb. 3. Schnitt durch das Feld einer im Freien stehenden Tonsäule. Länge der Lautsprecherzeile 140 cm, Frequenz 400 Hz, entsprechend  $\lambda = 85,5$  cm. Zwei benachbarte Linien gleichen Schalldrucks unterscheiden sich um 2,5 dB.

Zonenplatte in Parallelebenen mit verschiedenen Abständen ausgemessen und gleichzeitig registriert. Die Abb. 3 ist ein Versuch für eine Spiralaustastung mit Niveaulinienregistrierung, die noch nicht voll automatisch geschrieben wurde.

(Eingegangen am 21. Januar 1957.)

### Schrifttum

Bekannte Schallfeld-Austastverfahren:

- a) Linienaustastung: SPANDÖCK, F., Ann. Phys., Lpz. (5) 20 [1934], 345.
- b) Kreisbogen-austastung: HARVEY, F. K. und KOCK, W. E., Bell Lab. Res. 28 [1950], 304.
- c) Zeilen-austastung: CANAC, F. und GAYREAU, V., Acustica 1 [1951], 2.